COMMISSIONING OF THE LARGE ANGLE BEAMSTRAHLUNG MONITOR AT SUPERKEKB

by

SALVATORE DI CARLO

DISSERTATION

Submitted to the Graduate School

of Wayne State University,

Detroit, Michigan

in partial fulfillment of the requirements

for the degree of

DOCTOR OF PHILOSOPHY

2017

MAJOR: Physics

Approved By:

_____

Advisor

_____

_____

_____

DEDICATION

I dedicate my dissertation work to my parents, Giacomo and Salvina.

ACKNOWLEDGEMENTS

Starting a PhD far from home was an incredible experience: new links with people and places, new knowledge, new paces. The sensation was sometimes pleasant, sometimes confusing, and I have found many friends along the path.

A special thanks goes to Prof. Giovanni Bonvicini who, with patience and care, I would say almost like a father, has contributed to my personal and professional growth. Besides inspiring me and shaping my view of physics, he has always reaffirmed and made clear to me the importance of moral integrity in our profession and in life.

I am grateful to my uncle Giuseppe for hosting me in his house for the entire period I was in Detroit. During the time we have lived together, I had the possibility of getting to know him better and appreciate his generosity and his love for life. He represented my family in Detroit, and with his presence it was much easier to live far from home.

I want to thank my whole family for being supportive toward my adventure overseas. In particular, I want to thank my parents, Giacomo and Salvina, who also came to visit me in USA during summer 2016. During my lifetime they have always left me free to choose whatever activity I was willing to undertake, and my achievements would have not been possible without them.

Finally, I am thankful to all professors, postdocs, students, and staff of the physics department who, in different ways, helped me during the time I was pursuing the degree. A special thanks goes to Joern Putschke and Kolja Kauder, who helped me every time I was in trouble with my computer codes.

TABLE OF CONTENTS

Dedication ii

Acknowledgments iii

List of Figures vi

Chapter 1 INTRODUCTION 1

The Standard Model 1

The particles of the Standard Model 1

Symmetries 3

Beyond the Standard Model 3

Two complementary approaches 5

SuperKEKB and the LABM 5

Chapter 2 SUPERKEKB AND THE BELLE II EXPERIMENT 8

KEKB and the Belle experiment 8

SuperKEKB 8

The Belle 2 detector 17

Luminosity 22

Beam instrumentation 24

Chapter 3 THE LARGE ANGLE BEAMSTRAHLUNG MONITOR . . . 28

The Beamstrahlung 28

The Large Angle Beamstrahlung Monitor 28

Optical channels 30

Optical boxes 39

Data acquisition (DAQ) 48

Mirrors and conveyor belt remote control 49

IP resolution 51

LABM observables 52

Chapter 4 DATA TAKING AND ANALYSIS 56

Conventions used 57

Pedestals and calibration 58

Data taking 59

Angular scans 63

Large angle synchrotron radiation 64

Bending magnets 66

Beam pipes and reflections 68

Streaks and IP angle 73

Analysis of the angular scans 75

Up-down asymmetry 83

Results of the angular scans 83

Chapter 5 SUMMARY AND CONCLUSIONS 85

Bibliography 86

Abstract 87

Autobiographical Statement 89

LIST OF FIGURES

Figure 1.1 The fundamental particles of the standard model. 2

Figure 1.2 Peak luminosity trends as a function of the years. The luminosity has increased by a factor 10 every 10 years in the last 50 years. Source: http://www.ung.si/en/research/laboratory-for-astroparticle-physics/projects/belle/ 6

Figure 2.1 Illustration of the SuperKEKB collider. SuperKEKB is an asymmetric collider, meaning that the elctron and positron beams have different energies and currents. The beams circulate in opposite directions and collide at the interaction point, where the Belle II detector records the events produced in the collisions. Source: http://www-superkekb.kek.jp/documents/LoI_accelerator.pdf 9

Figure 2.2 Betatron motion of a particle in the beam. When a particle of the beam is displaced from the ideal trajectory, it is subjected to oscillation in the transverse plane periodic respect to the s coordinate. Source: https://cds.cern.ch/record/1213281/files/p317.pdf . 12

Figure 2.3 Illustration of the beams at KEKB and SuperKEKB, the latter one using the nano-beam scheme. We notice how the SuperKEKB beams are squeezed respect to the KEKB ones. Source: http://www.phys.vt.edu/\protect\unhbox\voidb@x\penalty\@M\{}piilonen/BelleII-Piilonen3.pdf 13

Figure 2.4 The interaction point set up for the commissioning phase. The Belle 2 detector in the background. 15

Figure 2.5 The electron and positron beams collide at a crossing angle, making the effective length of the beams equal to d. Source: http://www-superkekb.kek.jp/documents/B2TDR.pdf 16

Figure 2.6 "The hourglass effect". The positron beam in red, the electron beam in green. Near the interaction point the beams become more focused and therefore, if the are two long, they can assume the shape of a hourglass. Source: https://accelconf.web.cern.ch/accelconf/e02/PAPERS/MOPLE039.pdf 17

Figure 2.7 The detector has cylindrical shape, with beams colliding near the axis of the cylinder. The Belle 2 detector consists of a series of sub-detectors, starting from the most internal one and going in order of increasing radius. Source: https://www.belle2.org/research/detector/ 18

Figure 2.8 Schematic of one of the modules of the TOP detectors. The TOP detector allows, through a algorithm, to identify the species of the incident charged particle. Source: http://www-superkekb.kek.jp/documents/B2TDR.pdf 20

Figure 2.9 Beam position monitor configuration. Four electrodes are placed at four position on a plane transverse respect to the beam pipe to measure the current on the inner wall of the beam pipe. Measuring this current, it is possible to establish the position of the beam inside the beam pipe. Sources: http://linac96.web.cern.ch/linac96/proceedings/tuesday/tup67/paper.html; https://www.bnl.gov/edm/review/files/references/RShafer_AIP_249_601_1992.pdf . 25

Figure 3.1 The interaction region in the Tsukuba area on the left, the four KEK areas specified on the right. The position of the LABM is indicated on each side of the IP. Source: http://www.wikiwand.com/de/KEK_(Forschungszentrum) 29

Figure 3.2 A schematic of the whole LABM apparatus. The optical channel is described in section 3.3. The optical box is described in section 3.4. The DAQ system is described in section 3.5. 30

Figure 3.3 Some details of the optical channel. 1)Beam pipe; 2)Heat sink; 3)Cooling fan; 4)Primary pipe; 5)Primary elbow; 6)Small pipe; 7)Secondary elbow; 8)Big pipe; 9)Steel rods 31

Figure 3.4 Vacuum mirrors configuration inside the beam pipe. The vacuum mirrors are located about 5 meters far from the interaction point (IP). The beamstrahlung is collected by two mirrors per side, one on the top, and the other of the bottom of the beam-pipe. The beams travel in the z direction. 32

Figure 3.5 Beam-beam deflection of beams with a given offset Δ: the two beams will be attracted toward each other during the collision, with the result of being deflected. Source: http://accelconf.web.cern.ch/AccelConf/l86/papers/th3-16.pdf 33

Figure 3.6 Vacuum mirror design on the left; top and side view of the heat sink and beam pipe window on the right. 34

Figure 3.7 Normal reflectivity for the Berillium vacuum mirrors. The solid line is the s-polarization. The dashed line is the p-polarization. 35

Figure 3.8 The remotely controlled secondary elbow. Mirror frame with the two screws on the left. Stepper motors installed to rotate the screws on the right. 36

Figure 3.9 Elbow: front view on the left; back view with panel removed and view of the mirror mount at the center; back view with panel and mirror removed on the right. 37

Figure 3.10 Normal efficiency of the aluminum mirrors for perpendicular and parallel polarizations. Source: `http://motor1.physics.wayne.edu/\protect\unhbox\voidb@x\penalty\@M\{}giovanni/hussein.pdf` 38

Figure 3.11 LED board inserted on the primary pipe on the left. LEDs seen from inside the optical channel on the right. The LEDs allow to visually align the position of the mirrors in the optical channel. . . . 40

Figure 3.12 View of the inside of the optical box. The box contains many optical elements, the photomultiplier tubes (PMTs) used to measure the beamstrahlung, and the electronics needed to read the signal from the PMTs and send it to the DAQ. 1)Wollaston prism, 2)Gratings, 3)Mirrors, 4)Focusing prism-lens, 5)Conveyor belt, 6)Photo-multipliers, 7)Electronics. 41

Figure 3.13 Schematic of the Wollaston prism (WP). The WP is used to decompose the unpolarized incident wave into two waves with perpendicular polarizations. Source: Hecht E. "Optics", 5th edition. 42

Figure 3.14 Blazed diffraction grating: the maximum power is reflected toward the first order peak ($m = 1$). Source: `https://www.thorlabs.com/newgrouppage9.cfm?objectgroup_ID=26` 43

Figure 3.15 The Prism-Lens system is used to focus the light incoming from the gratings into a smaller spot on the surface of the PMTs, in order to optimize the detection. 44

Figure 3.16 The conveyor belt during a calibration run. The rotation of the conveyor belt allows placing each PMT in the original position of every other PMT and therefore measuring the relative efficiencies. 45

Figure 3.17 Photo-multiplier tube (PMT) schematic. A PMT is a vacuum tube used to detect photons, basically multiplying the initial current produced by an incident photon. Source: `https://en.wikipedia.org/wiki/Photomultiplier` 46

Figure 3.18 The electronic board was designed to power the PMTs and allow discrimination of the output signal. The relevant elements of the board are: 1)SuperLemo connectors; 2)Low Voltage (LV) power +/- 5V; 3)Photo-multiplier tube connection; 4)Discriminator 10 mV. 47

Figure 3.19 Back panel of the electronic board: 1)Conveyor belt control; 2)110 V power; 3)SuperLemo connectors, the output is sent as low-voltage differential signaling (LVDS); 4)High Voltage (HV); 5)Not used in commissioning phase; 6)HV. 48

Figure 3.20 The optical box, shown without covering on the left, and with covering on the right. 49

Figure 3.21 Crate for Data acquisition: 1)High Voltage (HV) CAEN V6533; 2)V830 CAEN Scaler 32 channels; 3)CAEN V2718 controller, optic fiber. A3818 pci adapter. 50

Figure 3.22 Remotely controlled mirrors: 1)Input cable from the computer to the motor drivers; 2)Motor drivers; 3)Output cable from the motor drivers to the stepper motors; 4)Stepper motor inside the primary elbow; 5)Primary elbow. 51

Figure 3.23 Rounded collimator inserted in the elbow on the left. Final design of squared collimator on the right. The collimator is used to improve the spacial resolution of the LABM and to reduce the rate of photons arriving at the box. 52

Figure 3.24 Estimation of the IP resolution for the LABM. y_1 is half of the side of the collimator. y_2 is half of the side of the vacuum mirror. y_3 is half of the side of the spot at the IP. 53

Figure 3.25 Pathologies presented by colliding collinear beams. When the collision is not perfect, the energy in the x and y polarizations show a well determined pattern: 1)Beams offset on the left; 2)Beams tilted on the center; 3)One beam embedded inside the other on the right. . 54

Figure 4.1 Coordinate frame at the IP: this frame will be used, in the following, to present the results. On the sides, we see the bending magnets responsible for the emission of synchrotron radiation. 56

Figure 4.2 First rates measured by four of the PMTs of the LABM in February 2016. Time (hour) on the horizontal axis. Rate (Hz) on the vertical axis. 60

Figure 4.3 Rate-current correlation for PMTs 16 and 17. Rate (blue) and current (red) superimposed on the left. Time (hour) on the horizontal axis. Rate (Hz) on the vertical axis. Rate versus current on the right. Current (A) on the horizontal axis. Rate (Hz) on the vertical axis. We notice that the signal from the PMTs is linearly correlated to the current of the radiating beam. 61

Figure 4.4 The rates measured in passing from a $12\,mm$ to a $8\,mm$ collimator. We notice that the rate, for the same current of the radiating beam, drop to about 1/3 of the initial value. Time (hour) on the horizontal axis. Rate (Hz) on the vertical axis. 62

Figure 4.5 The beam emits SR while progressing through the magnet. The SR collected by the LABM is collected at different angles along the path. At the entrance of the bending magnet (BM) the angles are denoted by 1, in the center of the BM by 2, and the exit of the BM by 3. We are interested in the angles respect to the vacuum mirror. We have that the polar angle θ decreases during the progression, while the azimuthal angle at the exit of the magnet (3) is $\phi = \pi/2$. The result of radiation emitted by the beam while progressing inside the beam is a streak. 69

Figure 4.6 TiN reflectivity: (A) $\lambda = 650nm$; (B) $\lambda = 350nm$. The solid line is the s-polarization. The dashed line is the p-polarization. 70

Figure 4.7 Aluminum reflectivity: (A) $\lambda = 650nm$; (B) $\lambda = 350nm$. The solid line is the s-polarization. The dashed line is the p-polarization . 71

Figure 4.8 Figure for the calculation of the reflection angles inside a beam pipe of radius R. The thick line represents the streak produced by the radiating beam while progressing through the magnet. The reflection emitted by the X point of the streak is seen, from the vacuum mirror, at an angle φ. 73

Figure 4.9 Schematic to find the length of the direct streak from the geometry of the interaction region. L is the length and ρ is the radius of curvature of the bending magnet. 74

Figure 4.10 Schematic to find the angle α. The IP will be located at an angle α below the position of the bending magnet. The position of the bending magnet is identified with the position of the direct streak produced by the radiating beam while progressing through the magnet. 76

Figure 4.11 Nikko down scan. PMT 16 (red light X-polarized) on the left. PMT 23 (red light Y-polarized) on the right. The area of each cell is proportional to the intensity of the signal in arbitrary units. The red ellipse corresponds to the Beam Pipe Inner diameter at the IP. The direct image of the beam is the streak identified as I, while the structures labelled as II, III, IV, V are reflections. The position of the interaction point (IP) is found below the direct streak. 78

Figure 4.12 Nikko up scan. PMT 24 (red light X-polarized) on the left. PMT 31 (red light Y-polarized) on the right. The area of each cell is proportional to the intensity of the signal in arbitrary units. Instead of streaks, we obtained extended structures that make difficult to find the position of the direct image coming from the magnet. 80

Figure 4.13 Upgrades for the primary pipes and the primary mirrors. We have realized new primary pipes made of a single piece, and a new transmission system for the motors with forks used to rotate the screws that move the remotely controlled mirrors. 81

Figure 4.14 Oho down scan. PMT 11 (UV light X-polarized) on the left; PMT 12 (UV light Y-polarized). The area of each cell is proportional to the intensity of the signal in arbitrary units. We have a softer bending that results in short streaks, of size comparable to our resolution. Therefore, we are able to see only dots. The position of the interaction point (IP) is found below the direct streak. 82

Figure 4.15 Oho up scan. PMT 3 (UV light Y-polarized) on the left; PMT 4 (UV light X-polarized). The area of each cell is proportional to the intensity of the signal in arbitrary units. As for Oho Down, we have a softer bending that results in short streaks, of size comparable to our resolution. Therefore, we are able to see only dots. The position of the interaction point (IP) is found above the direct streak. 83

CHAPTER 1 INTRODUCTION

1.1 The Standard Model

The Standard Model (SM) is the currently accepted theory which explains the weak, electromagnetic, and strong interactions in particle physics. The SM includes 12 fundamental fermions, 4 gauge bosons which mediate the three above interactions, and the Higgs boson, which is necessary to explain the mass of the other fundamental particles. The SM is a quantum field theory based on local gauge invariance, and therefore the interactions involved are usually classified according to their symmetry under local gauge transformations. The mathematical theory of symmetry is the group theory, from where the SM directly borrows its terminology. Therefore, the weak and electromagnetic theory are grouped together to form a $SU(2) \times U(1)$ gauge theory (Electroweak interaction), while the strong interaction constitutes a SU(3) gauge theory.

1.2 The particles of the Standard Model

The fundamental particles of the SM are quarks and leptons (fermions), gauge bosons, and the Higgs boson. These particles are shown in Figure 1.1.

1.2.1 Fermions

Fermions are particles of semi-integer spin. The fundamental fermions of the SM are quarks and leptons, which are divided in three generations of increasing masses. The up and down quarks, the electron and its neutrino belong to the first generation; the charm and strange quarks, the muon and its neutrino belong to the second generation; the top and bottom quarks, the tau and its neutrino belong to the third generation. The up, charm, and top quarks have charge +2/3, while the down, strange, and bottom

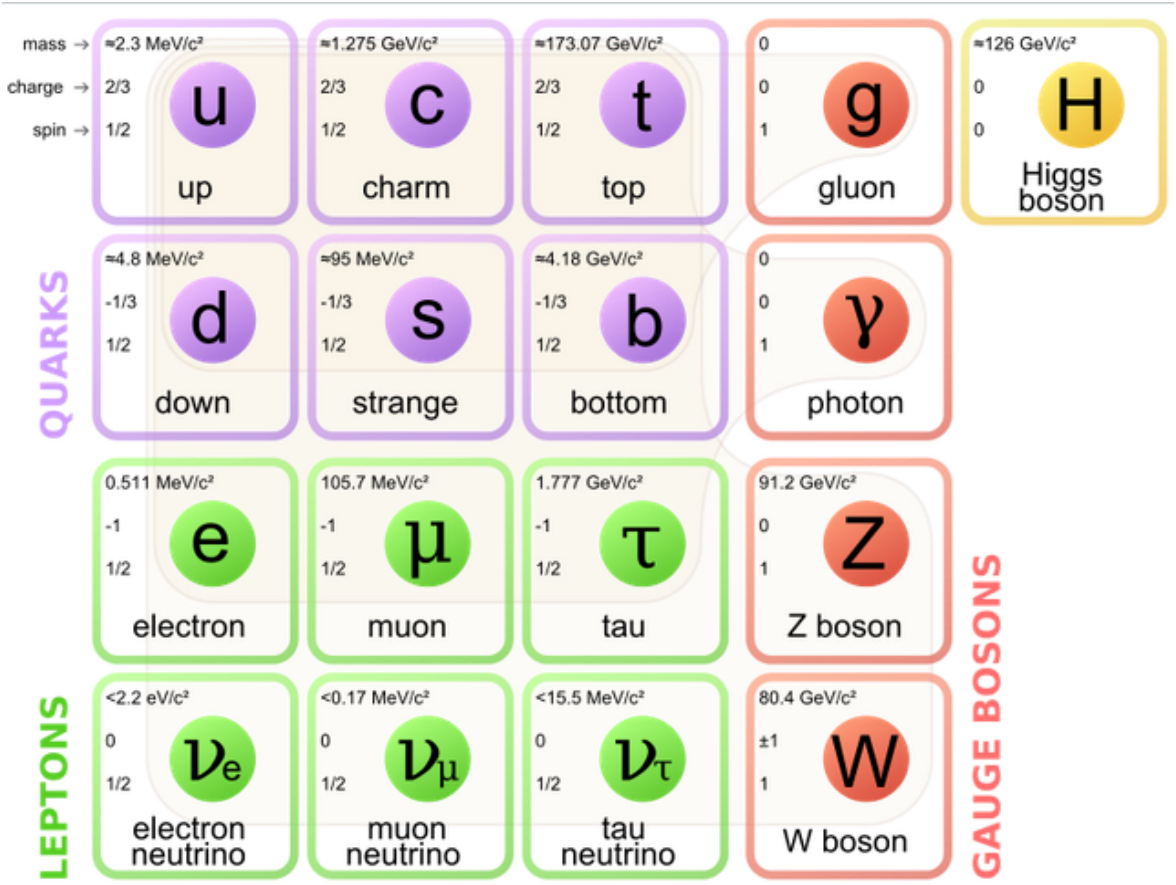

Figure 1.1: The fundamental particles of the standard model.

quarks have charge -1/3. The electron, muon, and tau all have charge -1, while their neutrinos are, as suggested by the name, neutral particles. Quarks also have color, a quantum number that by convention can be red, green, or blue. For each fermion there exists a corresponding anti-fermion with opposite charge and color. Quarks only exist confined within mesons or baryons, which are colorless combinations of quarks. In particular, baryons are made of three quarks and mesons are made of a quark and an anti-quark. Baryons and mesons are collectively called hadrons.

1.2.2 Bosons

Bosons are particles of integer spin. In the SM we have four gauge bosons which mediate the interactions. In particular, the photon mediates the electromagnetic in-

teraction, the gluon mediates the strong interaction, the W^{+-} and the Z mediate the weak interaction. Besides the gauge bosons, we have the Higgs boson, which is responsible for the masses of all the fundamental particles. Each of the gauge bosons has spin 1, the Higgs has spin 0. The photon and the gluon are massless, while the other bosons are massive. The W^{+-} is the only charged fundamental boson with charge +1 or -1 respectively.

1.3 Symmetries

In physics, a symmetry is an operation that, when applied, leaves the measurable quantities of a system unchanged. The most important symmetries in particle physics are the charge symmetry (C), the parity symmetry (P), and the time symmetry (T). The C symmetry changes every particle in its own anti-particle. The P symmetry changes a physical system in its mirror image. The T symmetry reverses the direction of the time. The strong and electromagnetic interactions are invariant with respect to C, P, and T symmetries. On the contrary, the weak interaction violates the C and P symmetries, and also the combined symmetry operation CP. One of the most important results of quantum field theory is the TCP theorem, which states that any interaction is invariant with respect to the combined symmetry operation of T, C, and P [1]. Because of the TCP theorem, the weak interaction is expected to violate also the T symmetry.

1.4 Beyond the Standard Model

The SM is probably one of the most successfully tested theories in the history of physics, but nevertheless it does not answer many fundamental questions. For example, one important issue is why matter dominates over antimatter in the universe. CP vio-

lation is a necessary ingredient for the matter to win over the antimatter[2]. In the SM, the CP violation is incorporated including a complex phase in the Cabibbo-Kobayashi-Maskawa (CKM) matrix. The CKM matrix contains the probability amplitudes of up quarks (u, c, t) decaying into down quarks (d, s, b) through the weak interaction. The CKM matrix in the Wolfenstein parametrization, with parameters A, λ, ρ, η is given in Eq. 1.1:

$$\begin{bmatrix} V_{ud} & V_{us} & V_{ub} \\ V_{cd} & V_{cs} & V_{cb} \\ V_{td} & V_{ts} & V_{tb} \end{bmatrix} = \begin{bmatrix} 1-\lambda^2/2 & \lambda & A\lambda^3(\rho - i\eta) \\ -\lambda & 1-\lambda^2/2 & A\lambda^2 \\ A\lambda^3(1-\rho-i\eta) & -A\lambda^2 & 1 \end{bmatrix} \tag{1.1}$$

The Cabibbo-Kobayashi-Maskawa theory was succefully verified in the Belle experiment at KEKB and BaBar experiment at SLAC. In these two experiments, indisputable evidence of CP violation was gathered studying the decays of B mesons. However, the latter effect is too small to explain the evolution of a universe where matter dominates over anti-matter. Moreover, the magnitudes of the CKM matrix elements can only be measured from experiments. Another unanswered issue is why we have three generations of quarks and if there are more, indeed the number of generations cannot be derived from the SM. From the above considerations, we see why the SM is considered too phenomenological, in the sense that many parameters are measured in experiments and cannot be derived from the theory itself. From what we said above, there are many clues that the SM is not the ultimate theory in particle physics. Many experiments are currently running (e.g. Atlas and CMS at LHC) and others are underway (e.g. Belle II at SuperKEKB) in order to find departures from the SM and give new clues about

how to develop new theories beyond the SM.

1.5 Two complementary approaches

Nowadays, the particle physics organizations are following two different but complementary approaches. The energy frontier approach consists in designing a particle accelerator that is able to provide the highest possible available energy to produce new particles or discover unknown processes at very high energies. This is the Atlas and CMS approach at LHC. Another approach consists in working at lower energy, thereby designing the accelerator in order to optimize the production of certain well known resonances and, studying their rare decays, underline some new processes that are not contemplated within the standard model. The latter is the path followed by Belle II in the framework of the SuperKEKB accelerator [3]. In the latter case, one must deal with rare events (i.e., events with a small cross section) which show departures from the SM. The rate of events production is given by the luminosity times the cross section:

$$\frac{dN}{dt} = \mathcal{L}\sigma \tag{1.2}$$

It is clear that the success and physics reach of this project depends critically on luminosity, one of the two figure of merit of the accelerator together with the energy. The purpose of our project is to help optimize the luminosity by monitoring the size and overlap of the colliding beams. This is discussed in detail in Chapter 2.

1.6 SuperKEKB and the LABM

SuperKEKB is a particle accelerator which is located in Tsukuba (Japan) and collides electrons with positrons. SuperKEKB is tuned at the $\Upsilon(4S)$ resonance, which corresponds to $\sqrt{s} = 10.58\, GeV$[3]. SuperKEKB is an asymmetric accelerator, meaning

that the energy and the current of the electron beam are different from those of the positron beam. In the search for new physics, SuperKEKB aims to achieve the very high luminosity of $8 \times 10^{35} \frac{1}{cm^2 s}$, becoming the particle accelerator with the highest luminosity ever reached (See Figure 1.2).

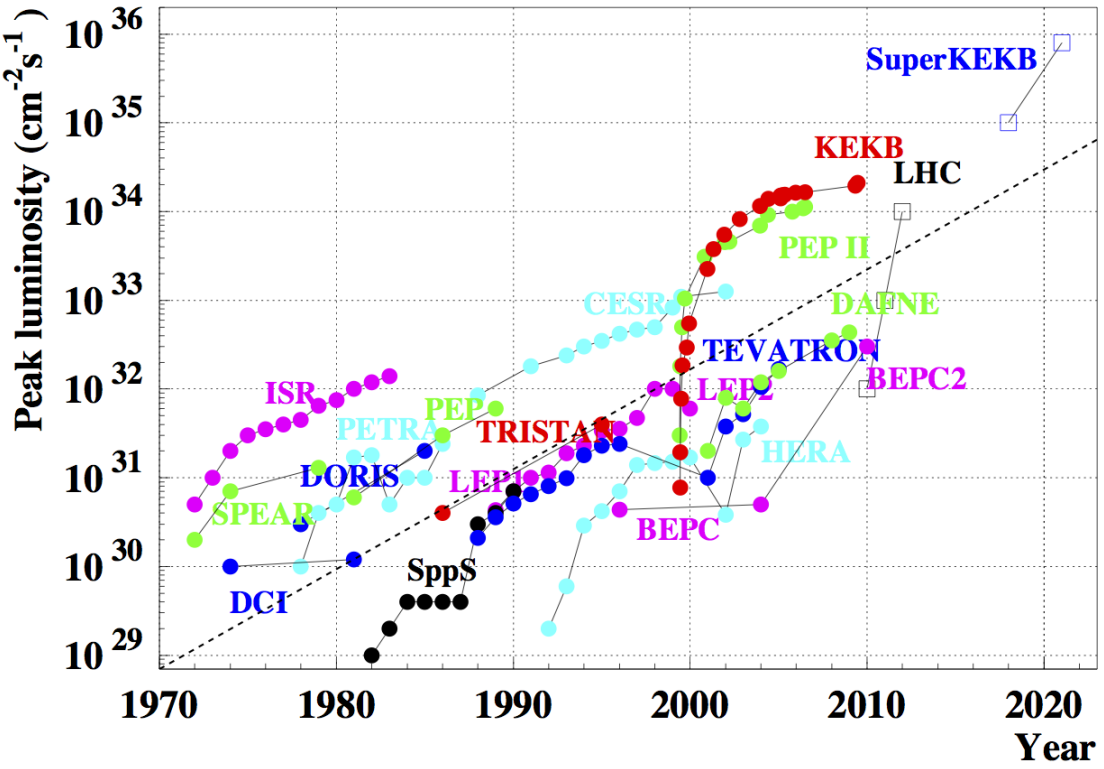

Figure 1.2: Peak luminosity trends as a function of the years. The luminosity has increased by a factor 10 every 10 years in the last 50 years. Source: `http://www.ung.si/en/research/laboratory-for-astroparticle-physics/projects/belle/`

SuperKEKB is a super-B factory (i.e., a collider designed to make B mesons) designed to use the nano-beam scheme, which contemplates very small beams and collisions at a crossing angle [3]. If, from one hand, the nano-beam scheme brings a significant advantage in terms of increasing the luminosity, on the other hand the beams are so small that it becomes difficult to ensure an optimal collision. SuperKEKB is equipped with many instruments which are supposed to help in monitoring the beams

at running time, such as a beam position monitor system (BPM), an X-ray beam profile monitor, a large angle beamstrahlung monitor (LABM), and many others [4].

The "Large Angle Beamstrahlung Monitor" (LABM) is a telescope designed to collect and analyze the radiation emitted during a collision between two charged beams. The radiation emitted in these events is called beamstrahlung. The emission of radiation is a classical phenomenon: one charged beam is subjected to the electromagnetic fields of the other charged beam, and therefore accelerates emitting light [5]. For given beams, it is apparent that the properties of the radiated light can only depend on the geometry of the collision. Indeed, it turns out that the main properties of the light, namely spectrum and polarization, can be used to monitor the relative position of the beams at the instant of the collision [6]. In the nano-beam framework of SuperKEKB, a powerful and versatile instrument such as the LABM becomes fundamental to monitor the geometry of the collision, making possible to adjust the beams position in case of eventual misalignment.

The total energy radiated for each collision is proportional to $1/m^2$, where m is the mass of the particles which constitute the beams. It is possible to show that there will be sizable emission of beamstrahlung light only in an e^+e^- colliders. A first prototype of LABM was designed to monitor the collisions at CESR, an e^+e^- collider located at Cornell University [7]. The definitive version of LABM, which is the object of this thesis, has been built for SuperKEKB.

CHAPTER 2 SUPERKEKB AND THE BELLE II EXPERIMENT

In this chapter I will introduce the SuperKEKB accelerator and the Belle 2 experiment. I will describe the most important features of the accelerator, the design of the Belle 2 detector, the main goals of the experiment, and the technical challenges involved in the project.

2.1 KEKB and the Belle experiment

KEKB was an electron-positron collider located in Tsukuba, Japan, and established in 1997. At KEKB, electron and positron beams of energies 8 GeV and 3.5 GeV, respectively, were collided. The center of mass energy was equal to 10.58 GeV, corresponding to the $\Upsilon(4S)$ resonance. The $\Upsilon(4S)$ then decays in two B mesons, whose decays are studied in order to find CP violation. This explains why KEKB is often referred as a B factory. The data produced was gathered from 1999 to 2010 through the Belle detector. The Belle experiment, named after the detector, was a history of success. To date, almost five hundred papers have been produced from the Belle collaboration. Moreover, the Belle experiment measurements of CP violation in the B system decays lead to Nobel prizes. Makoto Kobayashi and Toshihide Maskawa were awarded with the Nobel Prize in 2008. KEKB was shut down in 2010, in order to allow a major upgrade of both the accelerator and the detector. The upgrade and successor of KEKB was named SuperKEKB, while the upgraded detector was named Belle 2.

2.2 SuperKEKB

SuperKEKB factory is a Super B factory and represents an upgrade of the previous KEKB. SuperKEKB started the phase of beam commissioning on 1 February 2016. By the end of the month, the collider succeeded in storing and circulating both the

electron and the positron beams [8]. During this phase no collisions took place, and the BEAST II commissioning detector was used to measure the beams background [8]. As its predecessor KEKB, SuperKEKB is an asymmetric accelerator, with electrons of energy 7 GeV and positron of energy 4 GeV. Electrons and positron are accelerated in a linear accelerator and then injected in two storage rings, called High Energy Ring (HER) for the electrons and Low Energy Ring (LER) for the positrons. An illustration of SuperKEKB is given in Figure 2.1.

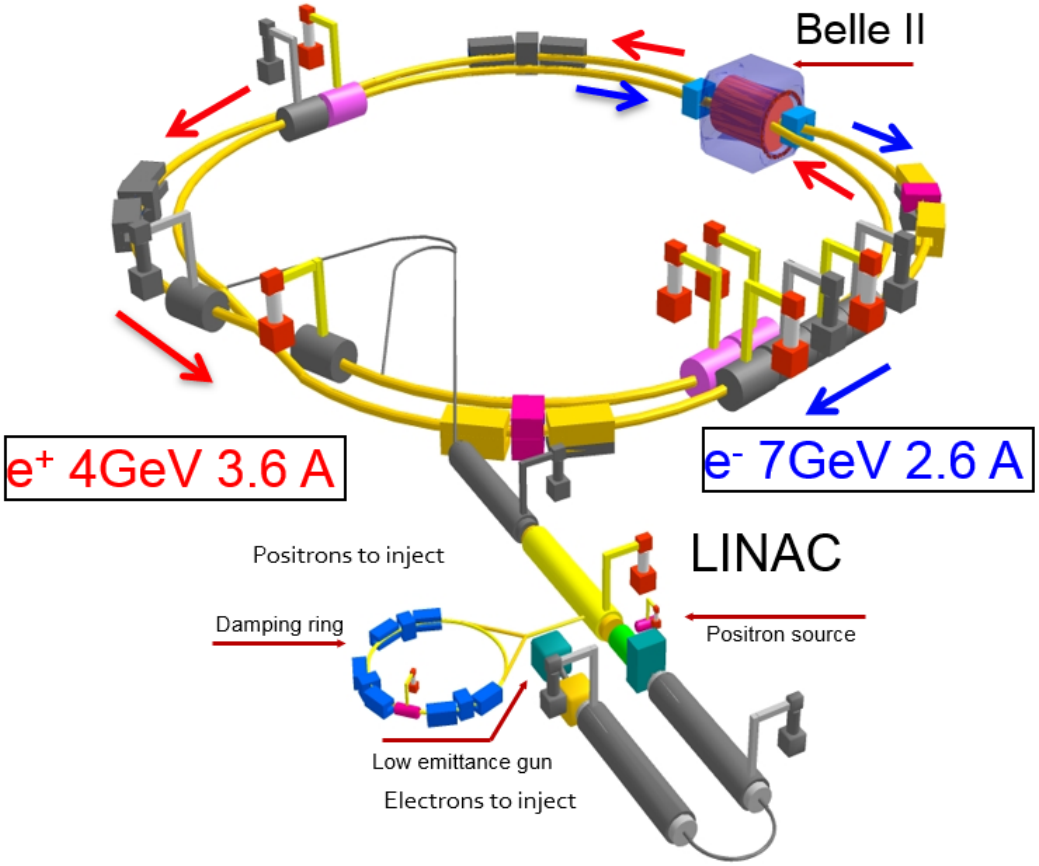

Figure 2.1: Illustration of the SuperKEKB collider. SuperKEKB is an asymmetric collider, meaning that the elctron and positron beams have different energies and currents. The beams circulate in opposite directions and collide at the interaction point, where the Belle II detector records the events produced in the collisions. Source: `http://www-superkekb.kek.jp/documents/LoI_accelerator.pdf`

In the following Sections we describe the various components of SuperKEKB.

2.2.1 Machine parameters

Before giving the machine parameters of SuperKEKB, it is essential to define some of the characteristic quantities used in accelerator physics. The beams are organized in bunches, much like beads on a string. Each bunch has a longitudinal spread of about 6mm and is separated by about 120 cm (4 nanoseconds) from the next bunch. They tend to have Gaussian particle distributions in all three dimensions.

Let us focus on a single bunch. The bunch is traveling around the ring, and it is customary to use s as the independent variable instead of the time. s is the coordinate that describes the position of the bunch in the ring. Moving together with the bunch we have our usual cartesian reference system, with coordinates (x, y) in the plane transverse to the motion of the bunch and the z coordinate pointing in the direction of motion. Let us consider the x coordinate (the treatment for y is identical). We need to consider the derivative of x respect to the independent variable s, which we define as $x' = \frac{dx}{ds}$. Given the normalized particle distribution in the (x, x') phase space $\rho(x, x')$ with $\int \rho(x, x')dxdx' = 1$, we define the moments of the distribution [9]:

$$< x >= \int x\rho(x, x')dxdx' \tag{2.1}$$

$$< x' >= \int x'\rho(x, x')dxdx' \tag{2.2}$$

$$\sigma_x^2 = \int (x - < x >)^2\rho(x, x')dxdx' \tag{2.3}$$

$$\sigma_{x'}^2 = \int (x' - < x' >)^2 \rho(x, x') dx dx' \tag{2.4}$$

The physical meaning of these quantities is apparent, with σ_x and $\sigma_{x'}$ describing the spread in the transverse position and momentum of the particles in the bunch. Another important machine parameter is the so called emittance of the beam, defined as [9]:

$$\epsilon_x = \sigma_x \sigma_{x'} \tag{2.5}$$

The emittance of the beam is a measure of the phase space volume accessible to the particles in the beam, i.e. the overall spread in position and momentum. It is important because it is invariant, meaning that a small σ_x can be obtained only by increasing $\sigma_{x'}$. We strive to produce low emittance beams so they can be easily focussed into small spots at the IP.

Finally, the last quantity I want to define is the so called beta function [9]:

$$\beta_x = \frac{\sigma_x^2}{\epsilon_x} \tag{2.6}$$

When a particle of the beam is displaced from the ideal trajectory, it is subjected to oscillation in the transverse plane periodic respect to the s coordinate. It is possible to show that the beta function is essentially the amplitude of this oscillation. This motion is usually referred as betatron motion and an illustration is given in Figure 2.2.

The frequency of oscillation in the transverse plane is called "tune", and the de-

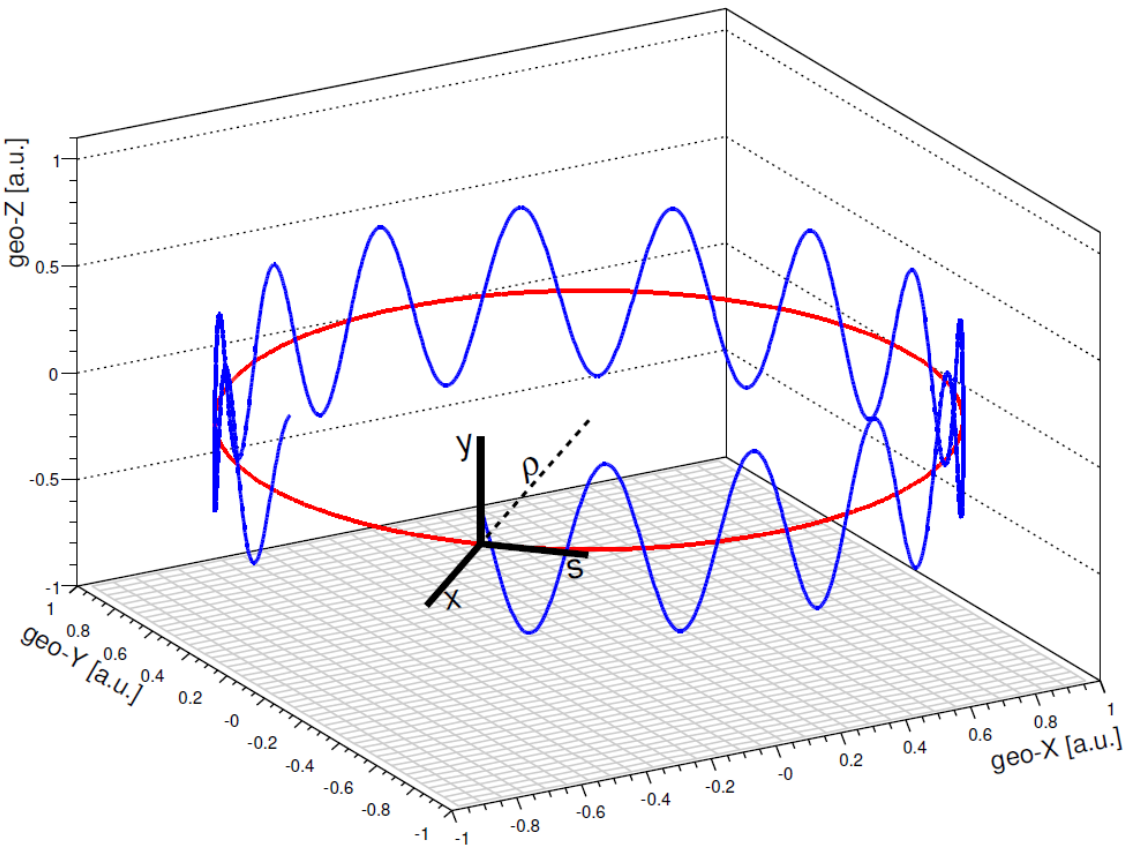

Figure 2.2: Betatron motion of a particle in the beam. When a particle of the beam is displaced from the ideal trajectory, it is subjected to oscillation in the transverse plane periodic respect to the s coordinate. Source: `https://cds.cern.ch/record/1213281/files/p317.pdf`

pendence of the tune from the momentum of the oscillating particle is called "chromaticity". The word chromaticity derives from the fact that, as electromagnetic waves of different energy experience a different index of refraction when they pass through a material, so particles of different energy inside a beam experience a different frequency of oscillation.

Equivalent relations hold for the y coordinate. Near to the interaction point the beams are usually more focused than in the rest of the storage ring, and therefore the machine parameters are denoted by a star. For example, the beam size and beta

functions in the neighborhood of the interaction point are usually denoted σ_x^* and β_x^*. Table 2.1 shows the machine parameters for KEKB and SuperKEKB[10].

	KEKB (e^-/e^+)	SuperKEKB (e^-/e^+)
$\sigma_x(\mu m)$	124/117	11/10
$\sigma_y(\mu m)$	1.9/1.9	0.062/0.048
$\sigma_z(cm)$	0.65/0.65	0.5/0.6
$\epsilon_x(nm)$	24/18	4.6/3.2
$\epsilon_y(nm)$	0.61/0.56	0.013/0.0086
$\beta_x^*(m)$	1.2/1.2	0.025/0.032
$\beta_y^*(m)$	0.0059/0.0059	0.0003/0.00027

Table 2.1: Machine parameters for KEKB and SuperKEKB [10].

From the Table, we can appreciate how the upgrade from KEKB to SuperKEKB will produce smaller beams with lower emittance and beta function at the IP. Figure 2.3 shows the impressive evolution of the beams size from KEKB to SuperKEKB. This upgrade strategy is referred to as the nano-beam scheme [3]. We will discuss further the implication of having such small beams later in this chapter.

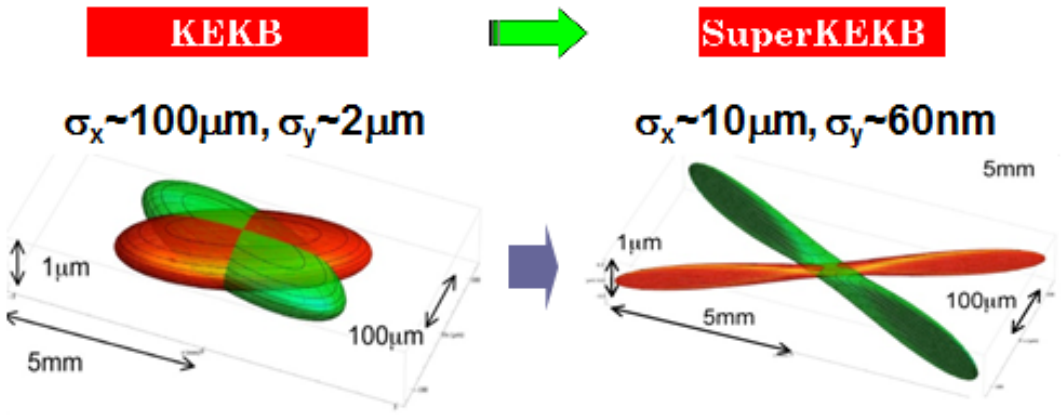

Figure 2.3: Illustration of the beams at KEKB and SuperKEKB, the latter one using the nano-beam scheme. We notice how the SuperKEKB beams are squeezed respect to the KEKB ones. Source: `http://www.phys.vt.edu/~piilonen/BelleII-Piilonen3.pdf`

2.2.2 The Linac

The linear accelerator (Linac) at SuperKEKB is 483 meters long. Beams of electrons and positrons are generated using two electron guns. The electrons coming from one of the two electron guns are accelerated along the Linac and then injected in the appropriate ring. The electrons produced in the other electron gun hit a tungsten target located in the middle of the Linac, producing positrons [3]. The positrons produced present a significant spread in angle and momentum and therefore need to be collimated before they can be injected in their storage ring. The positron are collimated in the damping ring (DP) located on one side of the Linac, as we can appreciate in Figure 2.1. Exiting form the DP, the positrons are accelerated in the remaining length of the Linac and then injected in their storage ring. The beams are accelerated in the Linac using Radio Frequency (RF) cavities. RF cavities are designed to contain electromagnetic fields oscillating at a certain frequency. The RF cavities allow to accelerate particles of low energy and decelerate particles of high energy, in such a way that the beams maintain an energy as close as possible to the ideal one. This also allows organizing the beams in bunches separated by a certain distance. In this way low energy particles in the Linac always feel a force in the forward direction, and therefore get accelerated.

2.2.3 The storage rings

The storage rings at SuperKEKB have a circumference equal to 3016 meters. Electrons and positron beams circulate in opposite directions and are stored for minutes or hours, which is a relative long time in particle physics. RF cavities are also present along the rings, in such a way to supply the necessary energy when the beams radiate and therefore lose energy. The rings are separated and join together only at the inter-

action point, in order to allow the collision between the beams. The interaction point set up for the commissioning phase is shown in Figure 2.4.

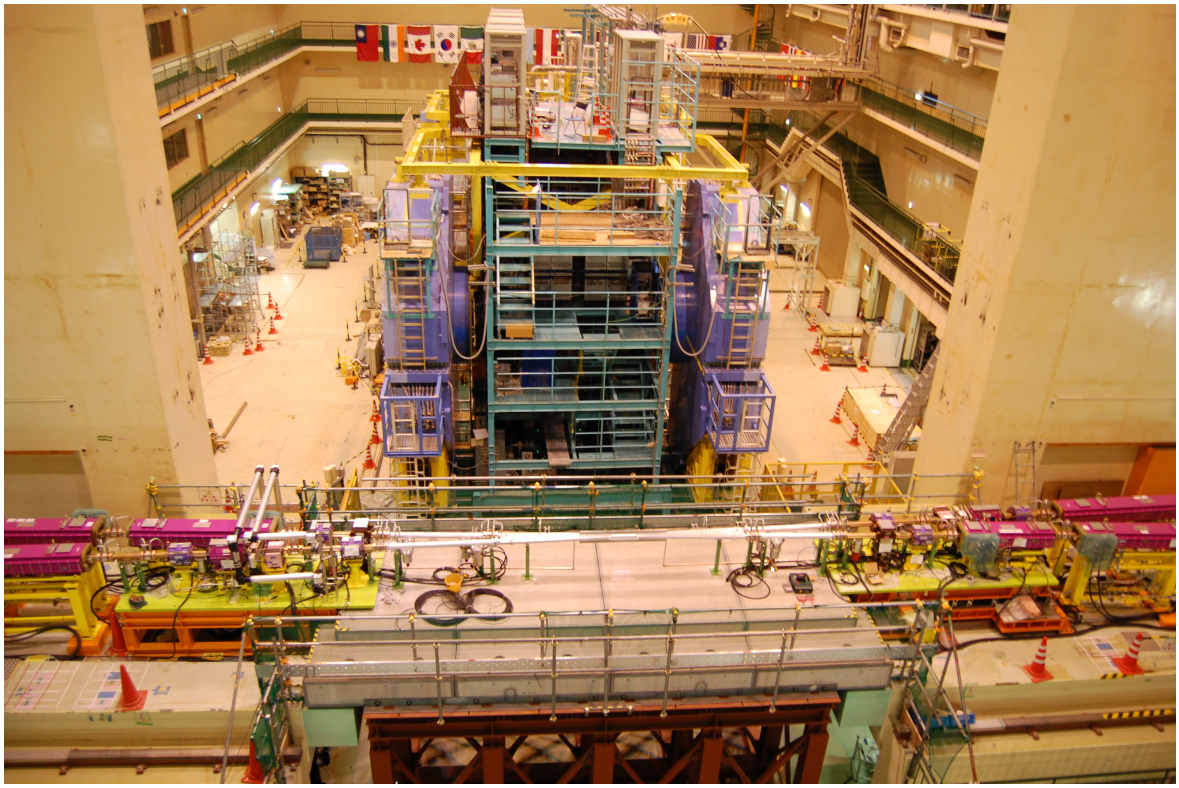

Figure 2.4: The interaction point set up for the commissioning phase. The Belle 2 detector in the background.

The rings are not really circular, but instead they are designed as octagons with arcs separated by straight pieces. The arcs are equipped with dipole magnets which make the beams turning from one straight piece to the next. The beams emit synchrotron radiation during the turns, because they are accelerated toward the center of the rings. The straight sections are equipped with RF cavities which accelerate the beams, in order to replenish the energy previously lost. The storage rings are also equipped with quadrupole and sextupole magnets which are used for different purposes in order to correct optical defects of the beam. The quadrupole magnets are used to focus

the beams whenever needed, in order to maintain them inside the beam pipes. The sextupole magnets are used to control the chromaticity of the beams.

2.2.4 The interaction point

The interaction point (IP) is where electron and positron beams collide at a crossing angle $\theta_c = 83\,mrad$, as in Figure 2.5. The radius of beam pipe at the IP, in its final design, is expected to be $10\,mm$ [3].

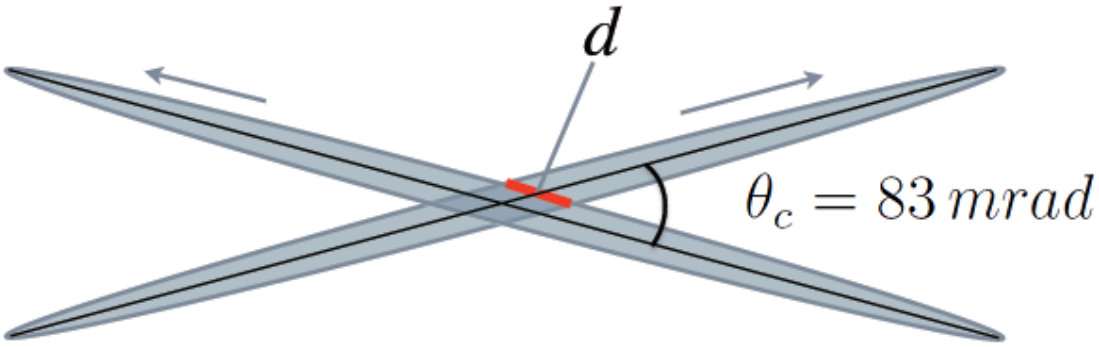

Figure 2.5: The electron and positron beams collide at a crossing angle, making the effective length of the beams equal to d. Source: `http://www-superkekb.kek.jp/documents/B2TDR.pdf`

Besides colliding beams at a crossing angle, SuperKEKB will use nano-beams. These two strategies, combined, make the effective length of the beam equal to d. From 2.5 it is clear that d is smaller than the total length, which would correspond to the effective length in case of head on collisions (i.e. $\theta_c = 0\,mrad$). This strategy allows to avoid the so called "hourglass effect", which affects collisions where the effective length of the beams is too large (or equivalently, β^* varies too quickly). Indeed, near the interaction point the beams become more focused and therefore, if the are two long, they can assume the shape of a hourglass. In other words, the transverse size of the beams near the interaction point is not constant along the beam, and this

lower the overall efficiency of the collision. The hourglass effect is illustrated in Figure 2.6, where we have a head on collision between a positron beam (red) suffering the hourglass effect and a much shorter electron beam (green).

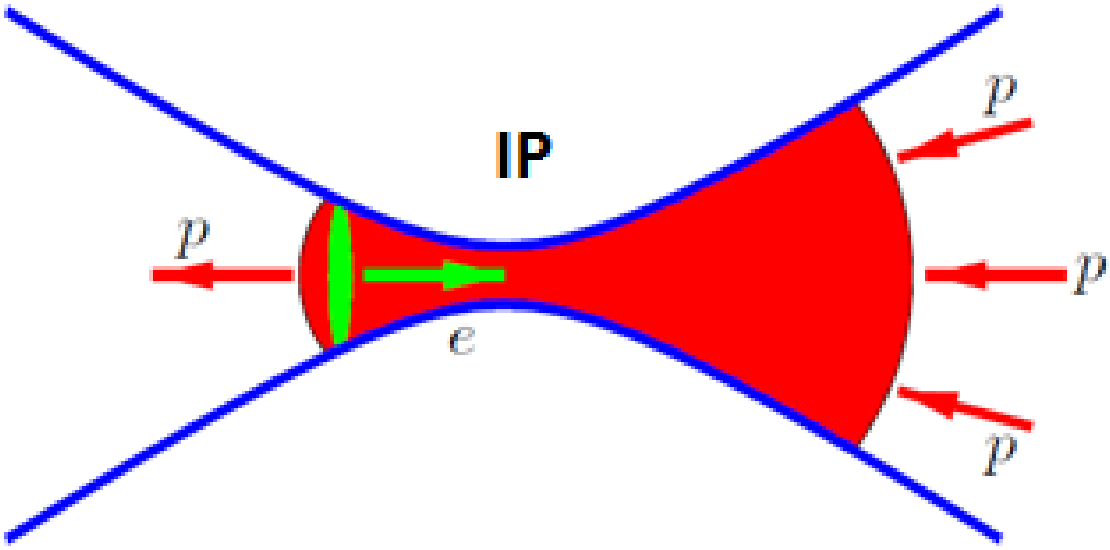

Figure 2.6: "The hourglass effect". The positron beam in red, the electron beam in green. Near the interaction point the beams become more focused and therefore, if the are two long, they can assume the shape of a hourglass. Source: `https://accelconf.web.cern.ch/accelconf/e02/PAPERS/MOPLE039.pdf`

2.3 The Belle 2 detector

The Belle 2 detector is a general purpose detector and it is an upgrade of the previous Belle detector. The detector is designed to record the events produced in the collisions of electrons and positrons at the SuperKEKB collider. The detector has cylindrical shape, with beams colliding near the axis of the cylinder. A solenoidal magnetic field of 1.5 Tesla is applied to identify the charge of the particles produced. The Belle 2 detector consists of a series of sub-detectors, as shown in Figure 2.7 that will be briefly described in the following, starting from the most internal one and going in order of increasing radius.

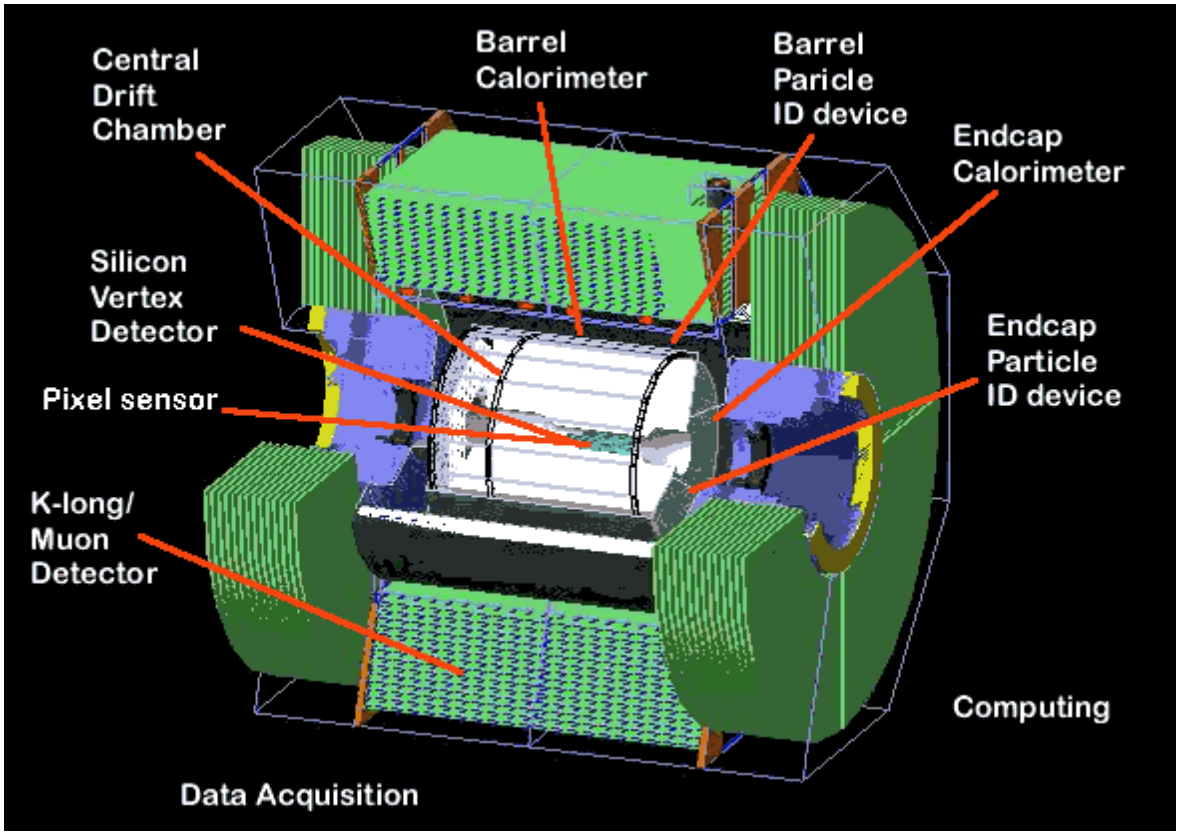

Figure 2.7: The detector has cylindrical shape, with beams colliding near the axis of the cylinder. The Belle 2 detector consists of a series of sub-detectors, starting from the most internal one and going in order of increasing radius. Source: `https://www.belle2.org/research/detector/`

2.3.1 Vertex Detectors

Since the radius of the beam pipe at the IP will be very small ($10\,mm$), the reconstruction of the B-decay vertices requires two different detection systems: the Pixel Detector (PXD), and the Silicon Vertex Detector (SVD).

2.3.1.1 Pixel Detector (PXD)

The two innermost layers, located in the range $10\,mm < r < 38\,mm$ of the vertex detector, are made of pixel sensors. This technology is characterized by thin (50 micron) design, which allow the sensors to fit within the small space, and low power consuming, which makes the cooling efficient [3].

2.3.1.2 Silicon Vertex Detector (SVD)

In the external part of the vertex detector, for $38\,mm < r < 140\,mm$, we find 4 layers of strip sensors, which constitute the silicon vertex detector (SVD). The angular acceptance covered by the SVD is $17 < \theta < 150$ [3].

2.3.2 Central Drift Chamber (CDC)

The next detector is the Central Drift Chamber (CDC), located in the range $160\,mm < r < 1130\,mm$. A drift chamber is a detector used to measure the trajectories of charged particles (charged tracks), as well as their momenta. The volume of SuperKEKB's CDC is filled with gas, specifically $He - C_2H_6$ [3]. Besides measuring tracks and momenta, the CDC also has a role in the particle identification (particle ID). Indeed, when a particle travels inside the CDC, it is possible to measure the energy loss in the gas. The energy loss depends on the momentum of the traveling charged particle, and every charged particle species (e, μ, π, K, p,) has its own characteristic dependence. In particular, when the particle has low momentum and cannot reach the more external particle ID detectors, the CDC is the only instrument capable of identifying the given particle [3].

2.3.3 Particle Identification - Barrel

External to the CDC, where the Time-Of-Flight (TOF) counter and the aerogel Cherenkov counter where present in the Belle experiment, we will now find the Time-Of-Propagation (TOP) counter. The TOP counter is an array of 16 quartz modules surrounding the CDC, covering the whole ϕ, and therefore resembling a barrel. The design of one of the modules of the TOP counter is shown in Figure 2.8.

When a charged particle passes through the TOP, Cherenkov photons are emitted

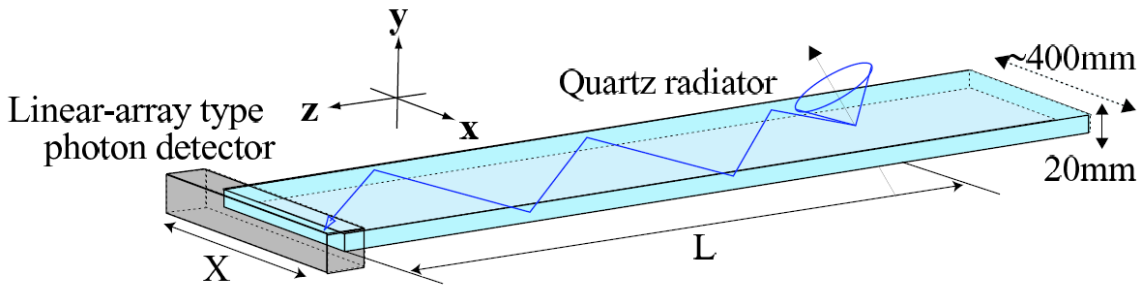

Figure 2.8: Schematic of one of the modules of the TOP detectors. The TOP detector allows, through a algorithm, to identify the species of the incident charged particle. Source: `http://www-superkekb.kek.jp/documents/B2TDR.pdf`

in a characteristic cone of angle θ_c. The photons reflect internally until they reach the endcap of the module and are measured using a grid of photo-multipliers (PMT). This allows to measure the (x, y) coordinates in the grid. The x coordinate is the same as the charged particle, while the y coordinate is related to the angle θ_c, which in turn depends on the charged particle species. Therefore, we have that photons from different particle species will be counted by different PMTs. Moreover, the TOP is designed to record the time it takes for the photons to reach the detector, called the time of propagation. In conclusion, the knowledge of the (x, y) coordinates together the time of propagation allows, through a algorithm, to identify the species of the charged particle.

2.3.4 Particle Identification: End-cap

At the End-cap of Belle 2, the particle ID is made using an Aerogel Ring-Imaging Cherenkov (ARICH) detector. The detector is composed of a radiating module of aerogel with a thickness of 2 cm, and an array of photon detectors located 20 cm farther [3]. The ARICH is particularly efficient in separating kaons from pions regardless from the momentum, while the identification among electrons, muons, and pions is efficient

only for momenta below 1 GeV/c [3].

2.3.5 Electromagnetic Calorimeter (ECL)

The Electromagnetic Calorimeter is a detector used to detect photons and measure their angular coordinates and energy. It is also used for the particle ID of electrons. The ECL for the Belle 2 detector is 3 meters long, making a barrel of radius 1.25 m, and covers a polar angle $12.4° < \theta < 155.1°$. The scintillation crystal is made of CsI(Tl). A calorimeter converts an incident particle of energy E into N particles of energy E_0, causing a "particle shower". In an ECL, the shower is produced by electromagnetic reactions: pair production ($\gamma \rightarrow e^+e^-$); compton scattering ($\gamma \rightarrow \gamma e^-$); bremsstrahlung ($e^- \rightarrow \gamma e^-$). The energy released is recorded and, having the calorimeter being correctly calibrated, it is possible to calculate the energy of the original particle.

2.3.6 K_L^0 and μ detector (KLM)

The ECL offers only 0.8 interaction lengths for K_L^0 to undergo hadronic shower, and therefore a K_L^0 can pass through the ECL without being detected. Moreover, the probability of muons undergoing electromagnetic showers is lower than for the electrons, because of the mass dependence of the bremsstrahlung. To detect both K_L^0 and μ we need a detector with a much longer interaction length. The KLM offers 15 layers of detectors alternated with 14 layers of iron, which allows for 3.9 interaction lengths for the K_L^0. The KLM is designed with both barrel and end-caps, covering the angular polar angle range $20° < \theta < 155°$ [3].

2.4 Luminosity

Energy and luminosity are the two figures of merit of a particle accelerator. At SuperKEKB, the center of mass energy is tuned at 10.58 GeV, corresponding to the $\Upsilon(4S)$ resonance. The rate of event production at SuperKEKB will be proportional to σ, the cross section of the $\Upsilon(4S)$. Recall that the constant of proportionality, $\mathcal{L}$, is the luminosity

$$\frac{dN}{dt} = \mathcal{L}\sigma \tag{2.7}$$

Before giving the rigorous definition of luminosity, we need to define some other important quantities. As already anticipated, the colliding beams of electrons and positrons are organized in bunches. At SuperKEKB, the bunches collide with a collision frequency $f = 250\,MhZ$. Let us define $\rho_1(\mathbf{r}, t)$ and $\rho_2(\mathbf{r}, t)$ as the charge densities of the two colliding bunches, traveling with velocities $\mathbf{v_1}$ and $\mathbf{v_2}$, and containing N_1 and N_2 particles, respectively. The luminosity is defined as the space-time integral of the product of the two charge densities, multiplied by the frequency collision and the magnitude of the relative velocity of the two beams:

$$\mathcal{L} = f N_1 N_2 |\mathbf{v_1} - \mathbf{v_2}| \int d\mathbf{r} dt \rho_1(\mathbf{r}, t) \rho_2(\mathbf{r}, t) \tag{2.8}$$

We can gain physical insight into this definition by considering the simplified case of a collision between Gaussian collinear beams. In this case we have density distributions given by:

$$\rho_1(\mathbf{r}, t) = N_1 G(x|0, \sigma_x) G(y|0, \sigma_y) G(z - ct|0, \sigma_z) \tag{2.9}$$

$$\rho_2(\mathbf{r}, t) = N_2 G(x|0, \sigma_x) G(y|0, \sigma_y) G(z + ct|0, \sigma_z) \tag{2.10}$$

where G is the Gaussian distribution. Carrying out the integration 2.8 with these Gaussian densities, a simple result is obtained for the luminosity [10]:

$$\mathcal{L} = \frac{f N_1 N_2}{4\pi \sigma_x \sigma_y} \tag{2.11}$$

From equation 2.11 we notice that, for a given collision frequency f, there are two ways of increasing the luminosity: increasing the number of particles per bunch or decreasing the size of the beams. For SuperKEKB the result in 2.11 is not valid, because the beams collide at a crossing angle, and therefore carrying out the integration 2.8 is a much more challenging task. However, the considerations just made about how to increase the luminosity remain valid. The strategy of increasing the number of particles in a beam is bound to bring instabilities in the beam plasma itself, leading to the so called "beam disruption" and effective beam enlargement. Indeed, the strategy at SuperKEKB is to produce very small beams of nanometer size, therefore called nano-beams. The greatest technological effort has been made at SuperKEKB to reach the world record design luminosity of $8 \times 10^{35} \frac{1}{cm^2 s}$. The luminosity and the other important parameters introduced in this paragraph are listed in Table for KEKB and SuperKEKB [10].

	KEKB (e^-/e^+)	SuperKEKB (e^-/e^+)
$\mathcal{L}(1/cm^2s)$	2.1×10^{34}	80×10^{34}
$E(GeV)$	8/3.5	7/4
$I(A)$	1.1/1.6	2.6/3.6
$N(10^{10})$	4.7/6.4	6.53/9.04
$f(MhZ)$	150	250

Table 2.2: Luminosity, energy, and other beam parameters related to the luminosity for KEKB and SuperKEKB [10].

2.5 Beam instrumentation

At SuperKEKB, the beams are so small that keeping them small and well aligned constitutes a technical challenge. Integrating 2.14 we obtain the number of events produced by a particle accelerator over a period of time:

$$N = \sigma \int \mathcal{L} dt \tag{2.12}$$

In a high energy experiment like the Belle 2 experiment the accelerator runs for 10-15 years, and therefore, if we want to produce a large number of events, it is necessary to maintain a high luminosity over the time. For these reason, SuperKEKB has many system useful to monitor and control the beams, maintaining them small, and keeping the luminosity at its design value.

2.5.1 Beam position monitors

Both storage rings are equipped with beam positions monitors (BPM), the HER with 466 and the LER with 445 [4]. BPMs are instruments used to monitor the position of the beam inside the beam pipe. Traveling inside the beam pipe, a charged beam produces electromagnetic fields. The problem is analogous to that of transverse electromagnetic (TEM) waves traveling in a cylindrical wave guide. In particular, a current

is produced on the inner wall of the beam pipe. Measuring this current it is possible to establish the position of the beam inside the beam pipe. To measure the current, four electrodes are placed at four position on a plane transverse respect to the beam pipe, as in Figure 2.9.

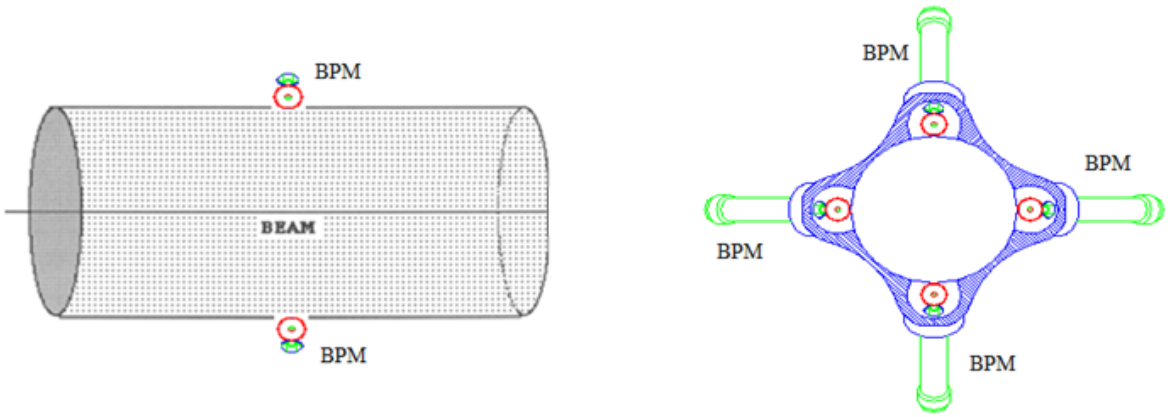

Figure 2.9: Beam position monitor configuration. Four electrodes are placed at four position on a plane transverse respect to the beam pipe to measure the current on the inner wall of the beam pipe. Measuring this current, it is possible to establish the position of the beam inside the beam pipe. Sources: `http://linac96.web.cern.ch/linac96/proceedings/tuesday/tup67/paper.html`; `https://www.bnl.gov/edm/review/files/references/RShafer_AIP_249_601_1992.pdf`

If we are interested in the vertical position of the beam, we can measure the current at the top U_t and at the bottom U_b of the pipe. The sum $U_t + U_b$ will be proportional to the bunch charge. The vertical position of the beam, relative to the center of the beam, pipe will be proportional to

$$y \propto \frac{U_t - U_b}{U_t + U_b} \tag{2.13}$$

2.5.2 Synchrotron radiation Monitors

When a beam goes past a bending magnet, synchrotron radiation is emitted and can be used to monitor the size of the beam. At SuperKEKB there are two categories of such monitor systems: visible light monitors and X-ray monitors.

2.5.2.1 Visible Light Monitor

There are two kinds of visible light monitors: interferometers, used to measure the horizontal size of the beams (σ_x); streak cameras, used to measure the length of the beams (σ_z) [4]. The radiation going to the interferometers is collected through some mirrors, and the incident power is expected to be $283\,W$ [4]. To avoid deformations due to the heat, special mirrors are used, which are made of diamond [4]. The resolution of such interferometers depends on the wavelength of the light and from the optical arrangement. The streak cameras are instrument designed to measure the length of a light pulse, with a typical resolution of $1\,ps$, and therefore a corresponding resolution $\Delta\sigma_z = 3 \times 10^{-4}$ meters.

2.5.2.2 X-ray monitor

At SuperKEKB an X-ray monitor will be used to measure the vertical size of the beam (σ_y) [4]. The technique used is called "coded aperture" and was initially developed by astronomers, with the purpose of measuring the size of the stars. The radiation emitted by the beams passes through masks having a special pattern, to which a specific algorithm is associated. The light is then collected with a plane of detectors and, through the algorithm, the image of the beam is reconstructed and the angle θ subtended obtained. Finally, knowing the distance R from the emission point to the mask, it is possible to calculate the vertical size of the beam as $\sigma_y = R\theta$.

2.5.3 Luminosity monitor

The luminosity monitor (LM) is a calorimeter designed to measure the number of photon emitted at zero angle. At SuperKEKB, the LM is located at an angle $0.9\,mrad$, covering a solid angle $d\Omega$. The LM measures the rate of photon produced within the solid angle covered by the calorimeter:

$$\frac{dN_{e^+e^+\to\gamma}}{dt} = \left(\frac{d\sigma}{d\Omega}\right)_{e^+e^+\to\gamma} d\Omega\,\mathcal{L} \tag{2.14}$$

The differential cross section is known, and therefore the LM is essentially a measure of the luminosity, and it is used to monitor the luminosity at run time.

2.5.4 The large angle beamstrahlung monitor

The large angle beamstrahlung monitor (LABM) measures the radiation emitted during the electromagnetic interaction of two charged beams, which is called beamstrahlung. The measure is carried at a much larger angle respect to the characteristic angle of synchrotron radiation, and this explains the name. The LABM allows to measure the spectrum and polarization of the beamstrahlung light, which are in turn related to the relative size and position of the beams. Unlike the other monitor systems, the LABM is able to deliver measures of the properties of the beams at the interaction point. The LABM is the subject of this thesis, and therefore we will thoroughly discussed in the next chapters.

CHAPTER 3 THE LARGE ANGLE BEAMSTRAHLUNG MONITOR

3.1 The Beamstrahlung

The Beamstrahlung (BS) is the radiation emitted from one beam of charged particles due to the electromagnetic interaction with another beam of charged particles [11]. We have emission of BS in every particle accelerator. However, the BS power is proportional to $1/m^2$, where m is the mass of the particles in the beams. Therefore, there will be sizable emission of BS only in an e^+e^- colliders. The main features of the BS, polarization and spectrum, are fundamentally related to the size and relative position of the beams. These properties represent a diagnostic tool that can be used to monitor the beam collisions in a e^+e^- storage ring [6].

3.2 The Large Angle Beamstrahlung Monitor

The Large Angle Beamstrahlung Monitor (LABM) has the peculiar capability to monitor the size of the beams at the interaction point (IP)[6]. The LABM measures the polarization and spectrum of the BS emitted at the IP during a collision. These properties are related to the size and relative position of the beams, therefore allowing to measure the latter ones [6]. The LABM collects the BS using four vacuum mirrors located inside the beam pipes. The light is then extracted though viewports and travels inside a series of pipes which constitute the four LABM's optical channels. Once extracted, the properties of the light are measured inside two optical boxes located outside the interaction region. The colliding beams travel at relativistic velocities, and therefore the BS is emitted forward within a narrow cone. The collision takes place at the Tsukuba area, with the positron beam emitting in the direction of the Nikko area, while the electron beam emitting in the direction of the Oho area. The terminology

used is illustrated in Figure 3.1.

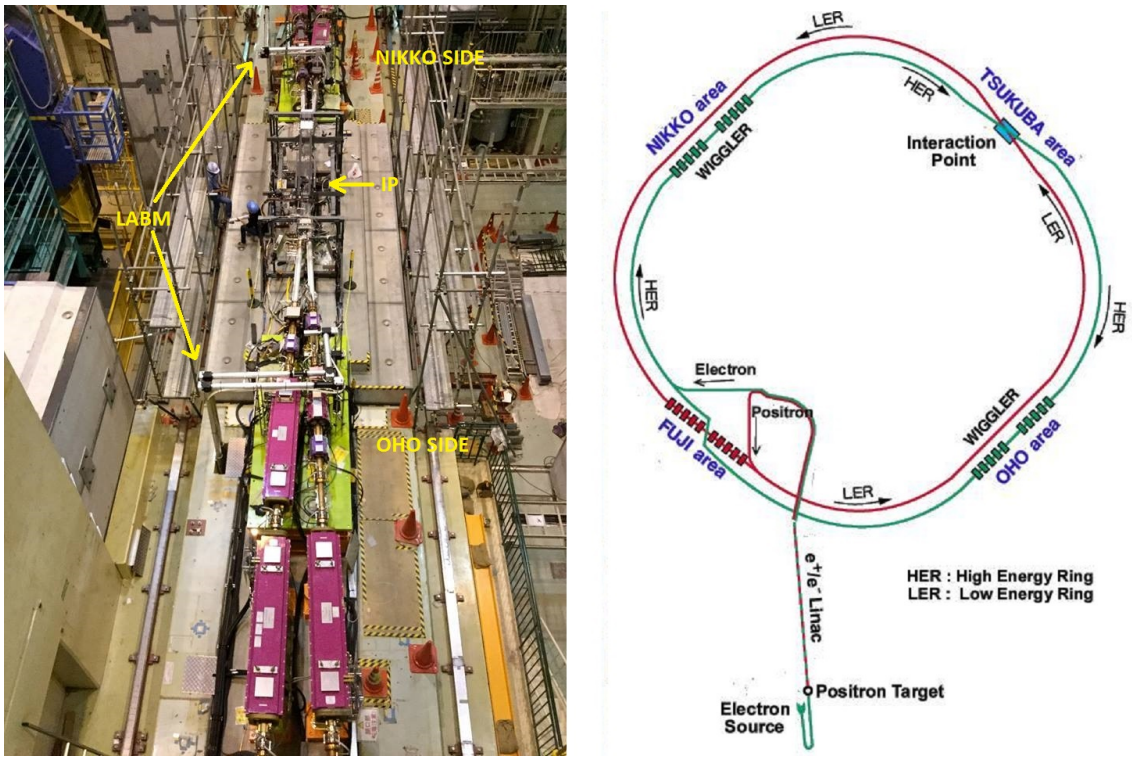

Figure 3.1: The interaction region in the Tsukuba area on the left, the four KEK areas specified on the right. The position of the LABM is indicated on each side of the IP. Source: `http://www.wikiwand.com/de/KEK_(Forschungszentrum)`

We notice that the positron beam circulates counterclockwise, while the electron beam circulates clockwise. The interaction point, and therefore the Belle 2 detector, is located in the Tsukuba area, while the remaining areas are not used in the Belle 2 experiment. The LABM is located in the Tsukuba area and it is basically divided in two sides, each one distant about 5 meters from the interaction point, as shown in Figure 3.1. In the following we will refer to each side of the LABM apparatus as the Nikko (LER, positrons) or Oho (HER, electrons) sides. We are now ready to describe the components of the LABM. A schematic of the whole apparatus is shown in Figure 3.2, while every component will be thoroughly described in the following sections.

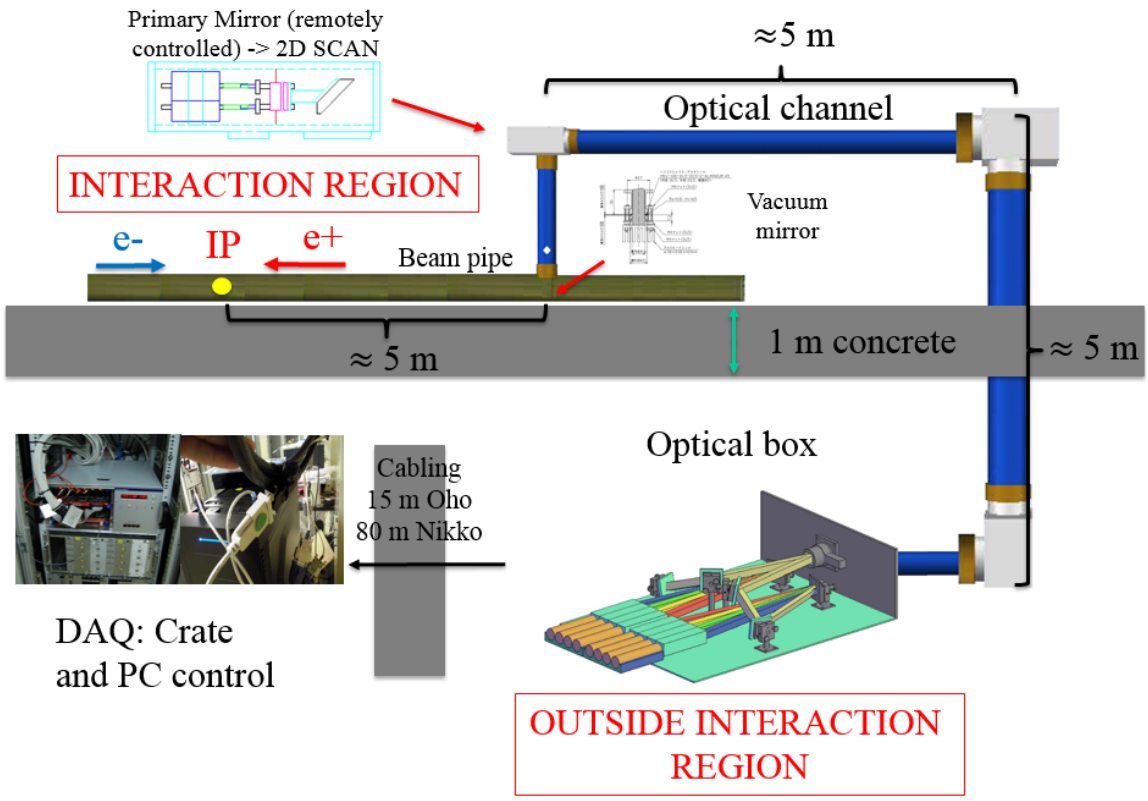

Figure 3.2: A schematic of the whole LABM apparatus. The optical channel is described in section 3.3. The optical box is described in section 3.4. The DAQ system is described in section 3.5.

3.3 Optical channels

The optical channels transport the BS light from the beam pipe to the optical boxes. There are four optical channels, two for each side of the LABM, which drive the light toward two optical boxes. The first element in the optical channel is a vacuum mirrors, located inside the beam pipe. The BS is then extracted through a window in the beam pipe, and the light travels inside aluminum pipes of several meters, joined with elbows. Inside each elbow there is a mirror, and the position of the first two external mirrors is remotely controlled. Some details of the optical channel are shown in Figure 3.3.

The optical channel is designed to work as a telescope, with long pipes that allow

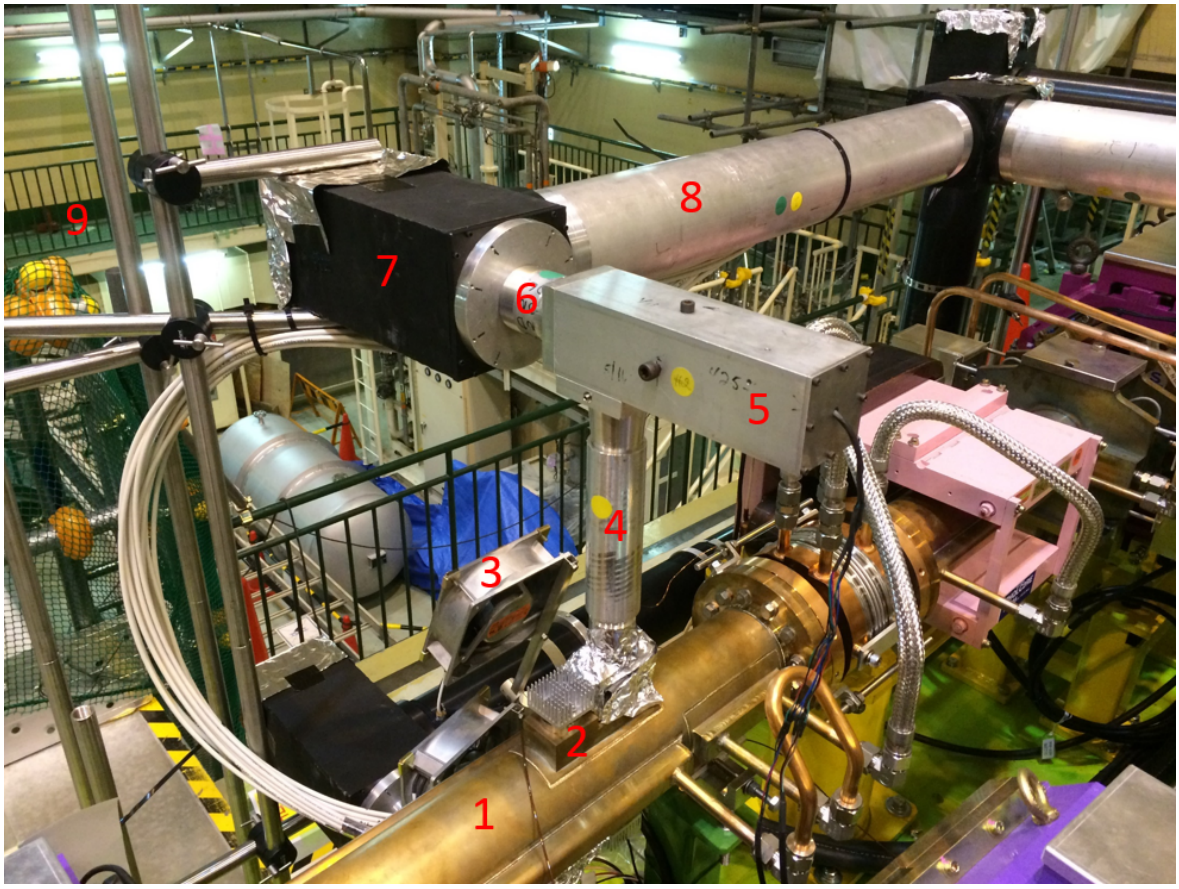

Figure 3.3: Some details of the optical channel. 1)Beam pipe; 2)Heat sink; 3)Cooling fan; 4)Primary pipe; 5)Primary elbow; 6)Small pipe; 7)Secondary elbow; 8)Big pipe; 9)Steel rods

to point toward a small region at the IP, and therefore really measuring only light coming from the collision between the beams. The total length (from the IP to the optical box) and efficiency of the four LABM optical channels are given in Table 3.1. The efficiency of the optical channel is defined as the ratio of the light that arrives at the box and the light incoming at the vacuum mirror.

3.3.1 Vacuum mirrors

The BS emitted at the IP is collected with vacuum mirrors, which constitute the first component of the LABM. On each side of the LABM, we have two vacuum mirrors, located inside the beam pipe, at about 4 meters from the interaction point. Therefore,

Optical channel	Length (m)	Efficiency
Oho Down	14.76	0.34
Oho Up	13.68	0.37
Nikko Down	15.89	0.34
Nikko Up	14.56	0.39

Table 3.1: Optical channels length and efficiency.

we have a total of four vacuum mirrors. One of the mirrors is located on the top and the other on the bottom of the beam pipe, as shown in Figure 3.4.

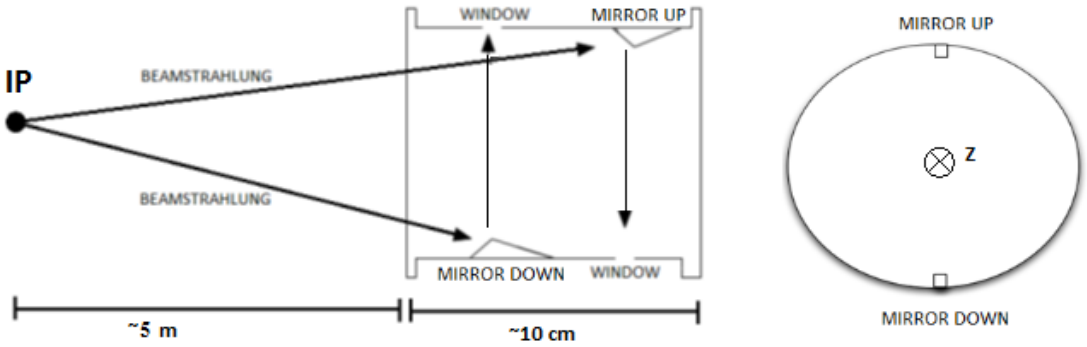

Figure 3.4: Vacuum mirrors configuration inside the beam pipe. The vacuum mirrors are located about 5 meters far from the interaction point (IP). The beamstrahlung is collected by two mirrors per side, one on the top, and the other of the bottom of the beam-pipe. The beams travel in the z direction.

The LABM was designed to have two vacuum mirrors, in order to measure the up-down asymmetry in the BS signal. The importance of the up-down asymmetry was understood already in the eighties, and the first method was invented by P. Bambade who used the beam-beam deflection [12] to extract information about the beam vertical sizes. Let us suppose to have a positron beam colliding head on with an electron beam. If the two beam are perfectly aligned, they will not be deflected during the collision. On the contrary, if there is an offset Δ between the two beams, the two beams will be

attracted toward each other during the collision, with the result of being deflected, as illustrated in Figure 3.5.

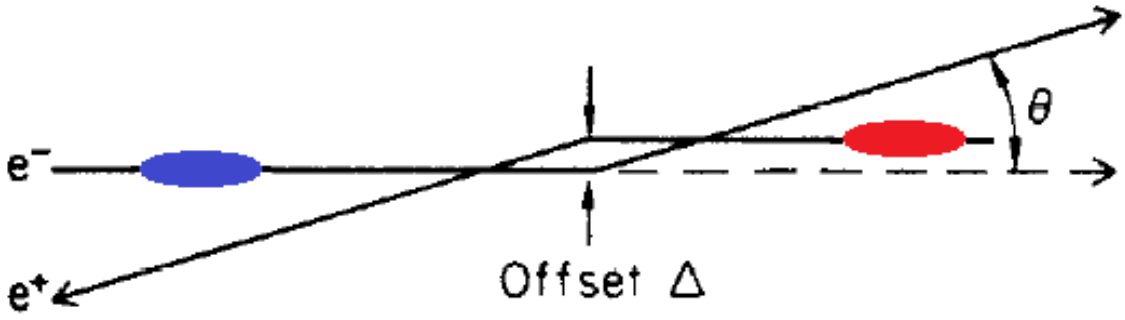

Figure 3.5: Beam-beam deflection of beams with a given offset Δ: the two beams will be attracted toward each other during the collision, with the result of being deflected. Source: `http://accelconf.web.cern.ch/AccelConf/l86/papers/th3-16.pdf`

As a result of the deflection, the BS will be mainly emitted in the direction of deflection. For example, in the case of Figure 3.5, we would have that the electron beam emits mainly up, while the positron beam emits mainly down. From the measurement of the up-down asymmetry, we could infer that there must be an offset Δ between the beams, and therefore correct the alignment.

The position and the total BS power received by each of the vacuum mirrors is given in Table 3.2.

Mirror	Distance IP (m)	$\theta_{min}(mrad)$	$\theta_{max}(mrad)$	BS Power (W)
Oho Down	4.51	8.43	8.87	8.08×10^{-8}
Oho Up	4.57	8.32	8.76	8.64×10^{-8}
Nikko Down	4.77	7.97	9.39	1.99×10^{-7}
Nikko Up	4.70	8.08	8.50	1.92×10^{-7}

Table 3.2: LABM vacuum mirrors parameters.

Each vacuum mirrors is $2\,mm$ wide, $2.8\,mm$ long, and inclined by 45° respect

to the beam pipe. This makes the effective area, as seen from the IP, $2\,mm \times 2.8(\cos(45°))\,mm \approx 4\,mm^2$. The mirror receives a relatively low BS power. However, due to the jump of the image current flowing on the internal wall of the beam pipe, the vacuum mirror receives a power of order 10 W and could become somewhat hot. Therefore, the vacuum mirrors are realized in Berillium, with an external cooling system. The cooling system consists of a heat sink, whose temperature is continuously monitored, cooled with a fan. The vacuum mirror and the cooling system were designed at KEK, and a technical drawing is shown in Figure 3.6. The vacuum mirrors have a normal reflectivity that depends on the polarization of the incident light, about 0.65 for the perpendicular component and about 0.42 for the parallel component (see Figure 3.7) in the visible wavelengths range.

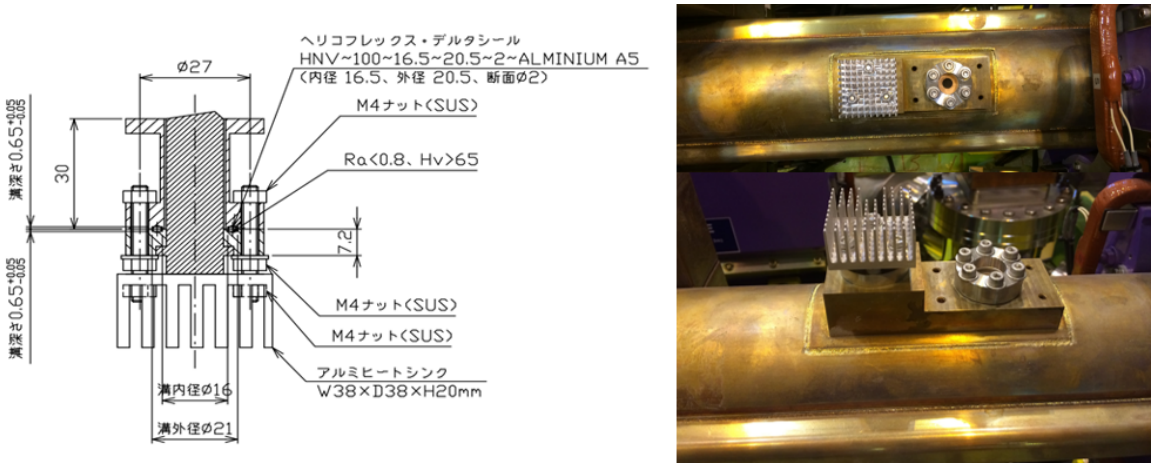

Figure 3.6: Vacuum mirror design on the left; top and side view of the heat sink and beam pipe window on the right.

3.3.2 Primary and secondary mirrors

To each vacuum mirror there corresponds an external primary and an external secondary mirror. Then, the BS light travels through the optical channels, with several other mirrors, before arriving to the optical boxes. However, the primary and secondary

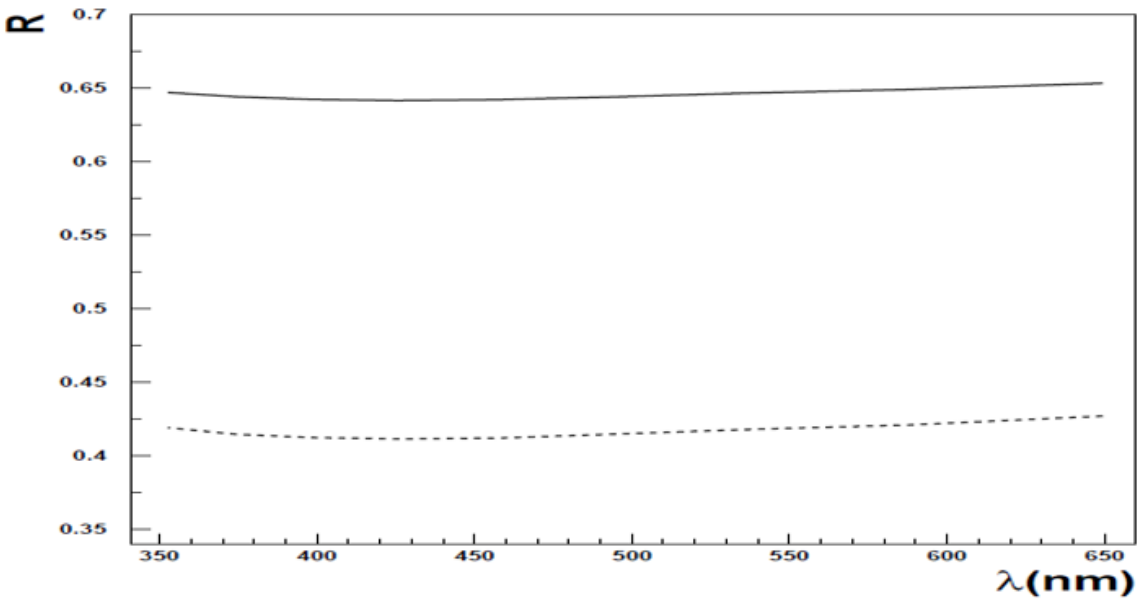

Figure 3.7: Normal reflectivity for the Berillium vacuum mirrors. The solid line is the s-polarization. The dashed line is the p-polarization.

mirrors deserve a special description, because they can be remotely controlled. The design uses high precision stepper motors to move the mirrors, and this enables to scan the plane transverse to the beam pipe. The mirror is mounted inside the elbow using a special frame that allows to adjust the position. Each mirror is controlled with two precision screws, each one moving the mirror around one of two perpendicular rotation axis. The stepper motor is equipped with a special fork to rotate the screw, and one motor is needed for each screw. The secondary elbow without and with stepper motors is shown in Figure 3.8.

This is a very important feature, because it allows scanning the signal coming from the IP direction, and therefore to find the exact position of the collision point. In the current design, the resolution of the LABM is about $6\,mm$ at the IP, meaning that the LABM can point at an spot of diameter $6\,mm$ on the transverse plane at the IP.

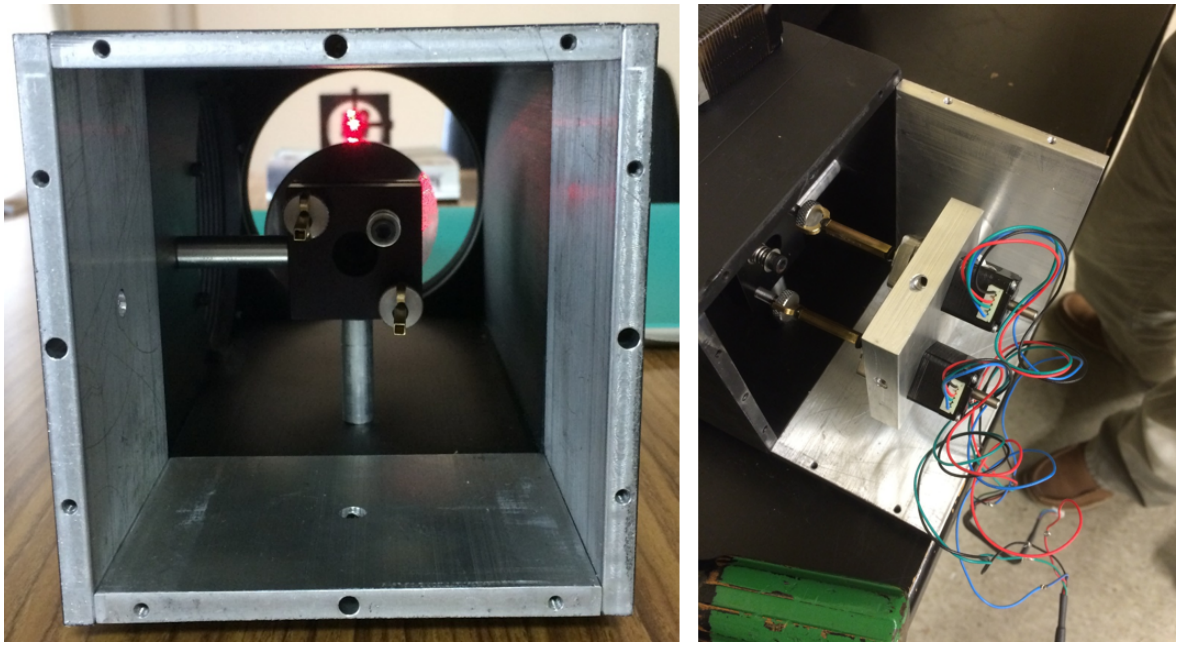

Figure 3.8: The remotely controlled secondary elbow. Mirror frame with the two screws on the left. Stepper motors installed to rotate the screws on the right.

The calculation of this resolution will be discussed later. The stepper motors allow to move this spot on the plane transverse to the beam pipe. The stepper motors can move the mirrors with a resolution of $4\,nrad$ for the primary mirrors and a $2\,nrad$ for the secondary mirrors. Assuming that the average distance of these mirrors from the IP is about $5\,m$, this corresponds to a displacement resolution of $20\,nm$ and $10\,nm$ respectively. Of course, since the spot has diameter $6\,mm$, it is not reasonable to scan the transverse plane with steps smaller than $1\,mrad$.

3.3.3 Pipes

The pipes are made in aluminum and are internally black painted, in order to avoid reflections from the internal walls. There are essentially three sizes of pipes: primary pipes, small pipes, and big pipes. The primary pipes connect the beam pipe to the primary elbow. The small ones connect the primary elbow to secondary elbow. The

big pipes are used after the secondary elbow until the optical channel reaches the optical box. The primary pipes have an internal diameter of $4.7\,cm$, the small pipes have an internal diameter of $5.1\,cm$, and the big pipes have an internal diameter of $10.2\,cm$. These pipes are shown in Figure 3.3. The aluminum pipeline constitute a giant antenna and therefore, because of the large electromagnetic fields present in the interaction region, could cause a significant noise in the electronics inside the boxes. For that reason, the last pipe, about $10\,cm$ long, is electrically insulated from the rest of the pipes. This result is achieved using rubber gaskets and plastic screws to insulate the last pipe from the last elbow.

3.3.4 Elbows and remaining mirrors

The elbows are used to connect pairs of pipes at 90° (See Figure 3.3). Pipes and elbows are threaded, and that means that when they are joined ambient light can not penetrate our system. Each elbow has a removable back panel, which allows to reach the mirror which is accommodated inside the elbow, as shown in Figure 3.9.

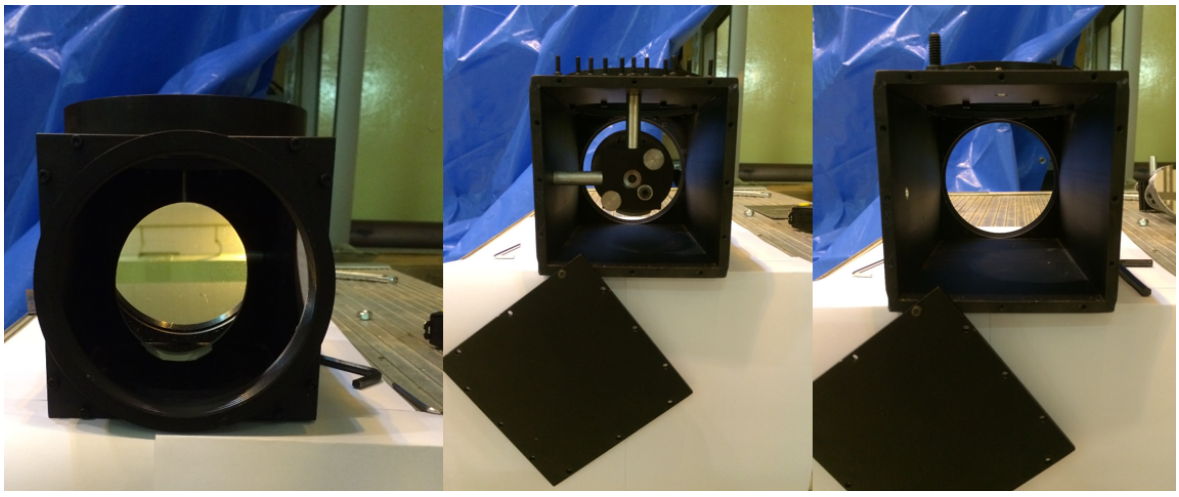

Figure 3.9: Elbow: front view on the left; back view with panel removed and view of the mirror mount at the center; back view with panel and mirror removed on the right.

The mirror is mounted on a frame, which is designed to adjust the position of the mirror. Two screws allow to rotate the mirror around two perpendicular axis. The design is the same as the one used for primary and secondary mirrors, with the difference that the remaining mirrors are adjusted manually. All the mirrors, besides the vacuum ones, have a reflective aluminum coating and have reflective efficiency between 0.9 and 0.95 (see Figure 3.10).

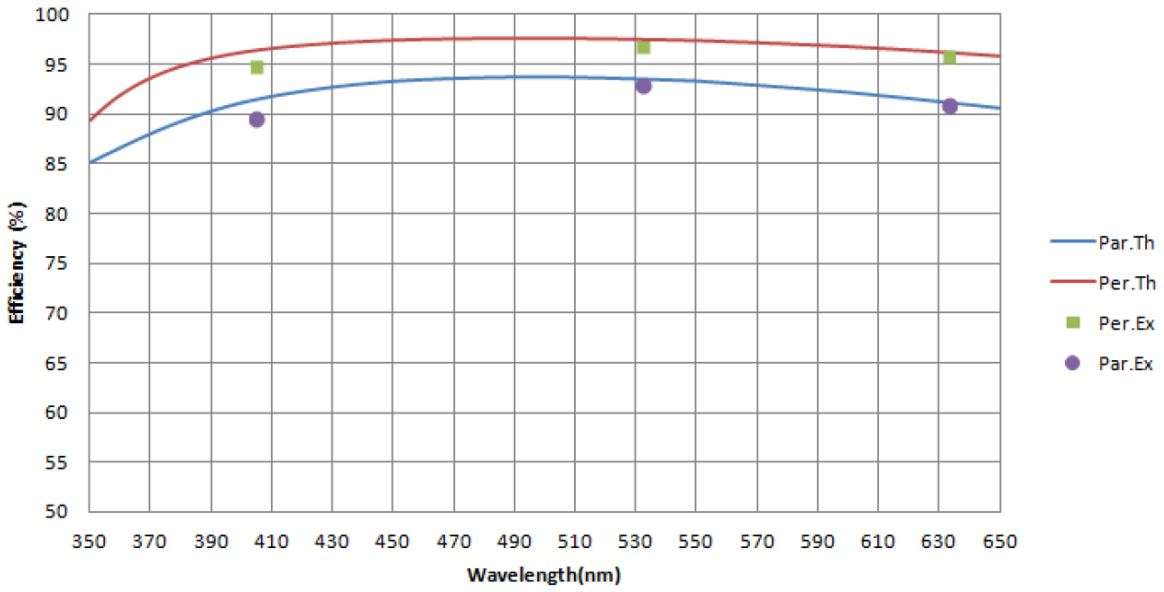

Figure 3.10: Normal efficiency of the aluminum mirrors for perpendicular and parallel polarizations. Source: `http://motor1.physics.wayne.edu/~giovanni/hussein.pdf`

3.3.5 Installation and alignment

The installation of the hardware part of the LABM requires approximately two working days, one for each side of the apparatus. The alignment of all the optical components may require one more day. The pipes are screwed into the elbows, both components being opportunely threaded. Moreover, the apparatus design must keep into consideration the seismicity of the region, and therefore special precautions are

taken. A large number of stainless steel round rods of diameter 2 cm are used to support and keep steady the pipes, and therefore the whole optical channel. Once the installation of pipes and support rods is ultimated, it is important to align the optical channel. The primary pipe has an aperture that is used to insert a light source, for example a LED, in order to visually align the position of the mirrors (see Figure 3.11). Starting from the secondary elbow, the procedure consists in removing the back panel, removing the mirror, and moving the previous mirror until the LED source is seen as perfectly centered. The procedure is repeated for all the successive mirrors, until the LED source is seen centered looking from the back of the last elbow. The source consists of three LED in row that are soldered to a board. The LEDs are of three different colors (red, yellow, green) and are controlled with an Arduino Uno board. The Arduino board is used to independently control each LED, which can be turned on and off, varied in intensity, and made to blink. The directional, color, and blinking properties allow, when the system is aligned, to easily distinguish the real image of the LEDs from the reflections.

3.4 Optical boxes

The optical boxes are not located in the interaction region, but at a lower floor that is shielded by a one meter concrete wall. This allows to shield the optical boxes from the direct influence of the electromagnetic fields present in the interaction region. The purpose of the optical box is to measure the polarization and spectrum of the BS light. There are two optical boxes, one for the Nikko side and the other for the Oho side. Each box is separated in two parts, one for the up signal, and the other for the down signal. Each side of the box is equipped with a Wollaston prisms, two ruled gratings,

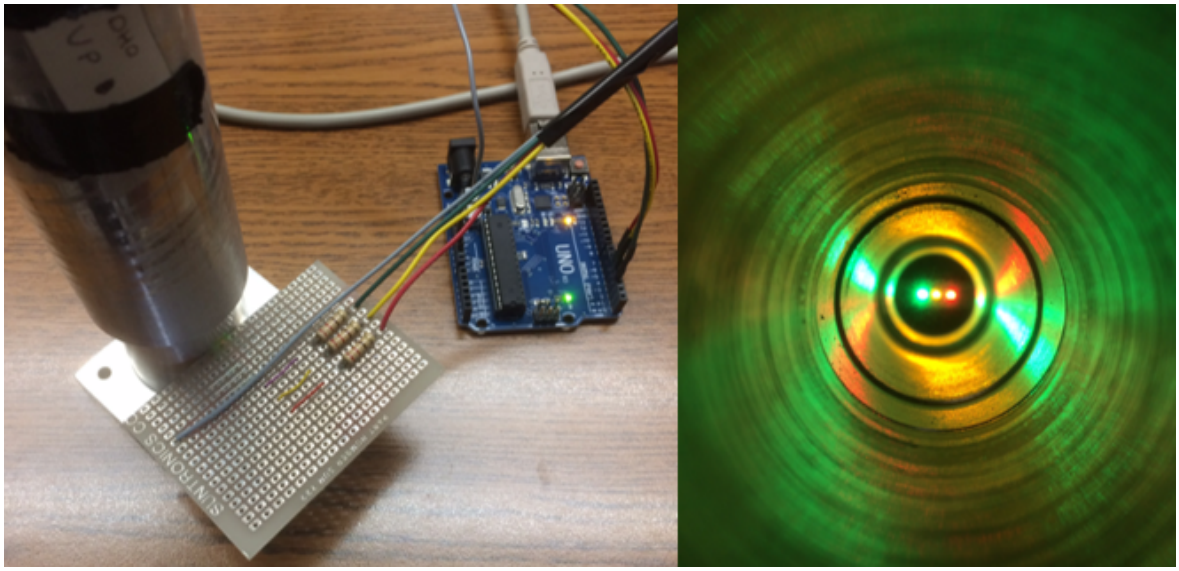

Figure 3.11: LED board inserted on the primary pipe on the left. LEDs seen from inside the optical channel on the right. The LEDs allow to visually align the position of the mirrors in the optical channel.

and four mirrors, as shown in Figure 3.12.

3.4.1 Wollaston prism

The Wollaston Prism (WP) is the first optical element inside the box, and it is used to separate the light in parallel and perpendicular polarizations. The WP is made of two calcite (calcium carbonate $CaCO_3$) prisms glued together at a wedge angle θ, as shown in Figure 3.13. In calcite it is possible to define an optic axis, such that the crystal is symmetric for a I_3 (3-fold symmetry) rotation respect to the axis itself. The two prisms are glued in such a way that the optic axis of the two prisms are perpendicular to each other. A wave with polarization perpendicular to the optic axis is a ordinary wave with refractive index n_o, while a wave with polarization parallel to the optic axis is a extraordinary wave with refractive index n_e. The separation of parallel and perpendicular components is due to the fact that, in calcite, $n_e < n_o$. When the incident wave hits the first prism, since the incidence is perpendicular, there is no deflection.

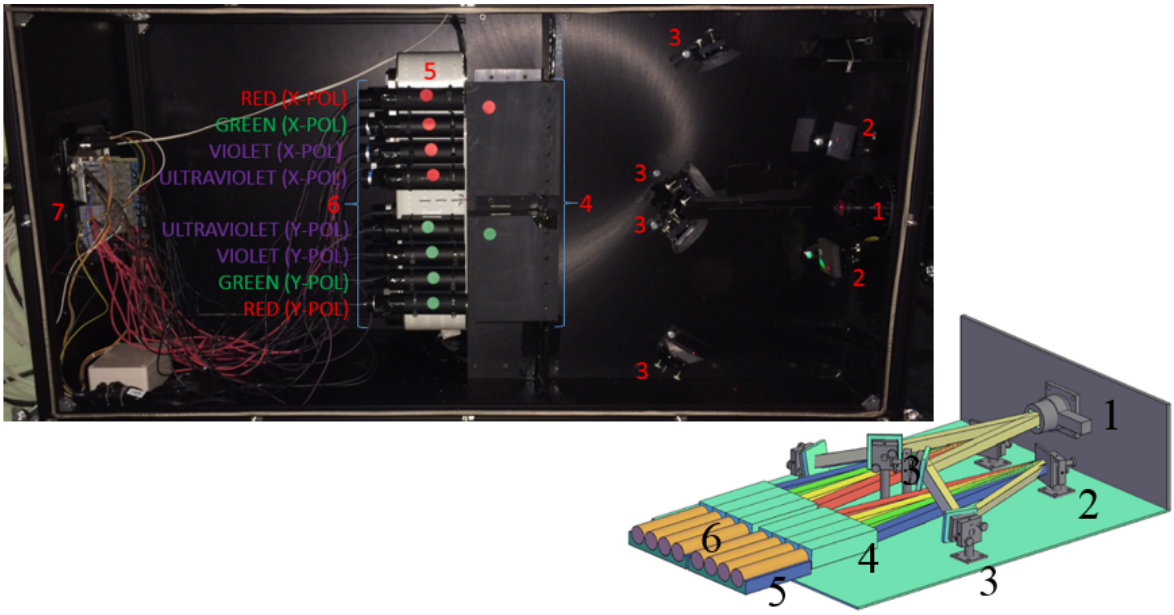

Figure 3.12: View of the inside of the optical box. The box contains many optical elements, the photomultiplier tubes (PMTs) used to measure the beamstrahlung, and the electronics needed to read the signal from the PMTs and send it to the DAQ. 1)Wollaston prism, 2)Gratings, 3)Mirrors, 4)Focusing prism-lens, 5)Conveyor belt, 6)Photomultipliers, 7)Electronics.

When the light reaches the second prism, the second optic axis is perpendicular to the first one and therefore ordinary and extraordinary waves interchange with each other. The interchange in the waves causes an interchange in the refractive indexes. Because of the Snell Law $n_e sin\theta_e = n_o sin\theta_o$, the extraordinary wave (old ordinary wave) is bent away from the normal to the separating surface, while the ordinary wave (old extraordinary wave) is bent toward the normal. At the prism air separation, the two waves are further refracted, resulting in a larger angle of separation. The result is a wave polarized along the optic axis of the second prism and another with polarization perpendicular to the same axis. The final angle of separation between the exiting polarized waves depends on the wedge angle θ. The WP used in the optical box allows for a separation angle of 20°.

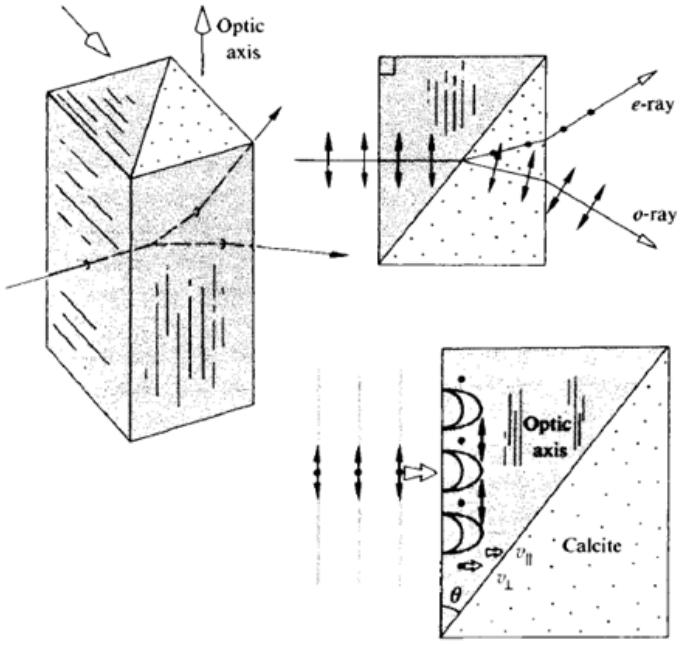

Figure 3.13: Schematic of the Wollaston prism (WP). The WP is used to decompose the unpolarized incident wave into two waves with perpendicular polarizations. Source: Hecht E. "Optics", 5th edition.

3.4.2 Mirrors

The mirrors used inside the box are of the same quality of those used in the optical channel, having an efficiency between 0.9 and 0.95 (see Figure 3.10). The mirrors are used to reflect the light coming from the WP toward the ruled gratings, thereby changing the plane of propagation inside the box.

3.4.3 Ruled diffraction gratings

The diffraction gratings are used to separate the light in spectral components. A ruled grating is an optical element made of a repetitive array of grooves, separated by a distance a. A white beam of light, incident at an angle θ_i on the grating, will give rise to a diffraction figure with peaks at angles θ_m. The position of the peak of order m is given by Eq. 3.1:

$$a(sin\theta_i + sin\theta_m) = m\lambda \tag{3.1}$$

The diffraction gratings used for the optical box are blazed, meaning that the maximum power is reflected toward the first order peak ($m = 1$). A picture of the diffraction grating used in the box is shown in Figure 3.14.

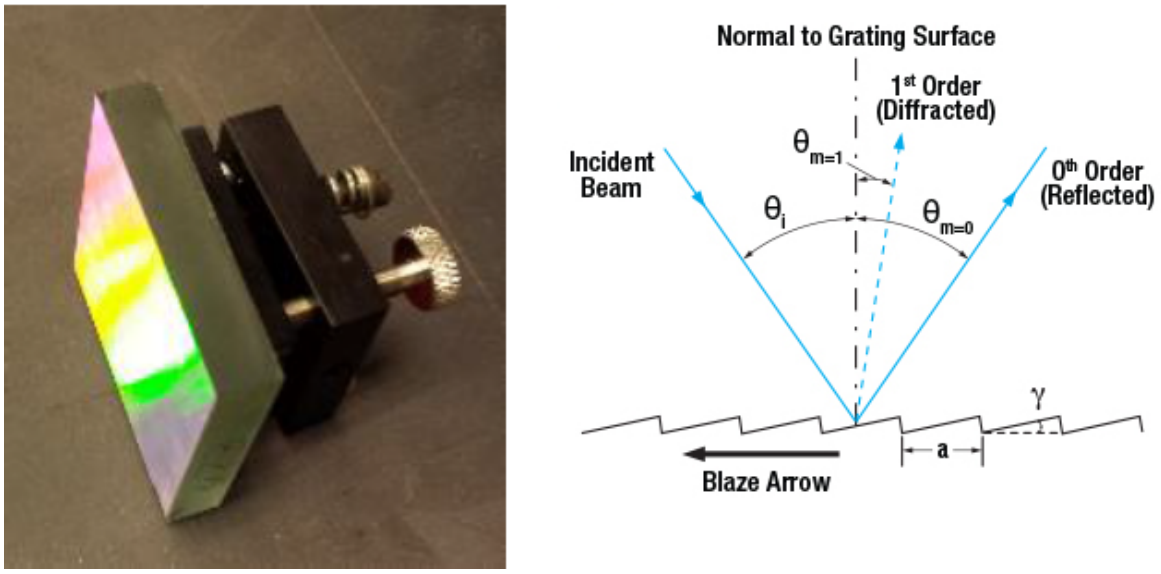

Figure 3.14: Blazed diffraction grating: the maximum power is reflected toward the first order peak ($m = 1$). Source: `https://www.thorlabs.com/newgrouppage9.cfm?objectgroup_ID=26`

3.4.4 Focusing prism-lens system

The light is reflected from the diffraction gratings toward the photo-multiplier tubes (PMT), but before it gets focused by a prism-lens system (see element 4 in Figure 3.12). The prism and the lens are glued together, in order to achieve a combined effect in a single optical element (see Figure 3.15). The prism is a refractive optical element that deflects the incident light in another direction. In our case, the prism deflects the BS light coming from the grating in the direction of the PMT. Then the lens focuses the

light into a smaller spot, in order to optimize the detection with the PMT (see Figure 3.15).

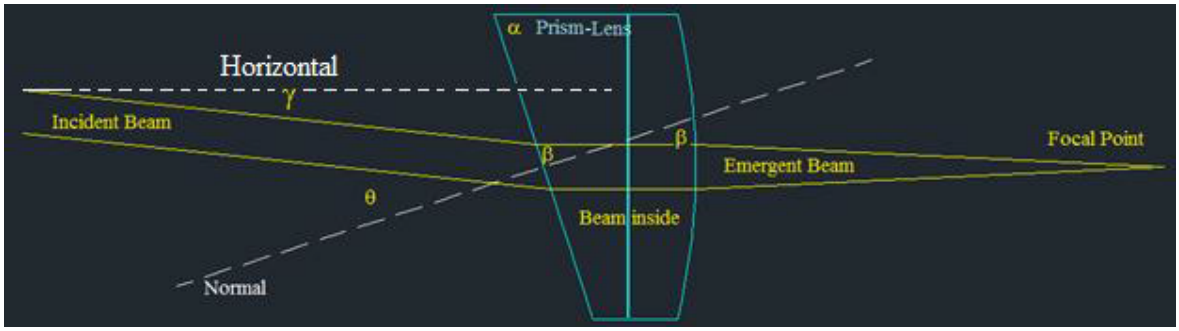

Figure 3.15: The Prism-Lens system is used to focus the light incoming from the gratings into a smaller spot on the surface of the PMTs, in order to optimize the detection.

3.4.5 Conveyor belt

The optical box is equipped with a conveyor belt that is remotely controlled. The conveyor belt was designed to accommodate the PMTs, like a cartridge case with PMTs instead of bullets. The rotation of the conveyor belt allows placing each PMT in the original position of every other PMT, as shown in Figure 3.16. This is a fundamental feature which enables to measure with high precision the relative efficiency of each PMT respect to each other PMT. Then, arbitrarily fixing the efficiency of one PMT, it is possible to define the absolute efficiency of all the other PMTs.

3.4.6 Photo-multiplier tubes

The detection of BS light is performed using photo-multiplier tubes (PMTs). A PMT is a vacuum tube used to detect photons, basically multiplying the initial current produced by an incident photon. Due to the great amplification of the signal, the PMT allows even single photon detection. The LABM is equipped with 16 PMTs per optical box. The PMT is shielded from external magnetic fields with a high permeability

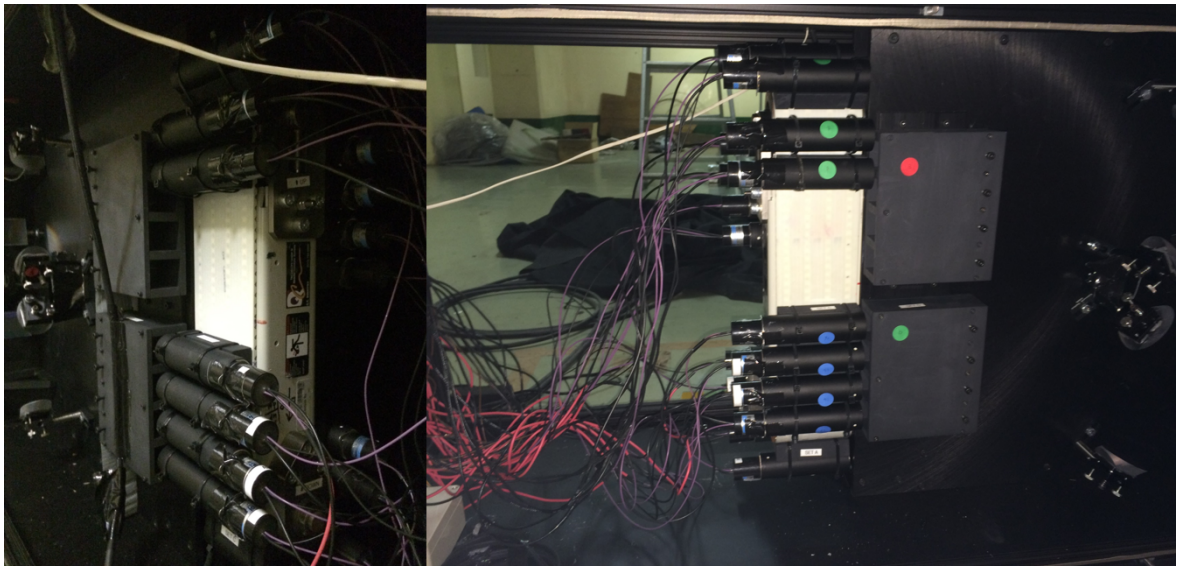

Figure 3.16: The conveyor belt during a calibration run. The rotation of the conveyor belt allows placing each PMT in the original position of every other PMT and therefore measuring the relative efficiencies.

material. The scheme of a PMT is shown in Figure 3.17. The initial component of the PMT is the photocathode, which in our case is a cesium compound. The cesium layer has a work function of $2\,eV$, therefore we cannot detect photons with a frequency lower than $\nu = 480\,THz$ (red). On the other hand, the glass of the window absorbs very much for photon energies higher that $5\,eV$. Therefore, we cannot detect photons with a frequency higher than $\nu = 1200\,THz$ (Near ultraviolet). The photocathode is a thin layer and, when a photon strikes it, an electron is emitted with a 20% probability. The next element is a series of dynodes at increasing electric potential. Each dynode is separately connected to one of the connector pins in the back of the PMT (see 3.17). For the LABM, the potential difference between the photocathode and the anode is $1380\,V$. The initial electron produced has a kinetic energy of about 100 eV and strikes the first dynode. Because each dynode has a work function of $5\,eV$, an average of 20 electrons are generated. Some of them recoil, and about 3 electrons make it to the next

dynode in average. The PMTs used in the LABM box have 12 dynodes, and therefore the overall gain will be $G = 3^{12} \approx 10^6$. On the last element, the anode, we reach an electron current of several mA. The final current is approximately proportional to the number of photons incident on the PMT.

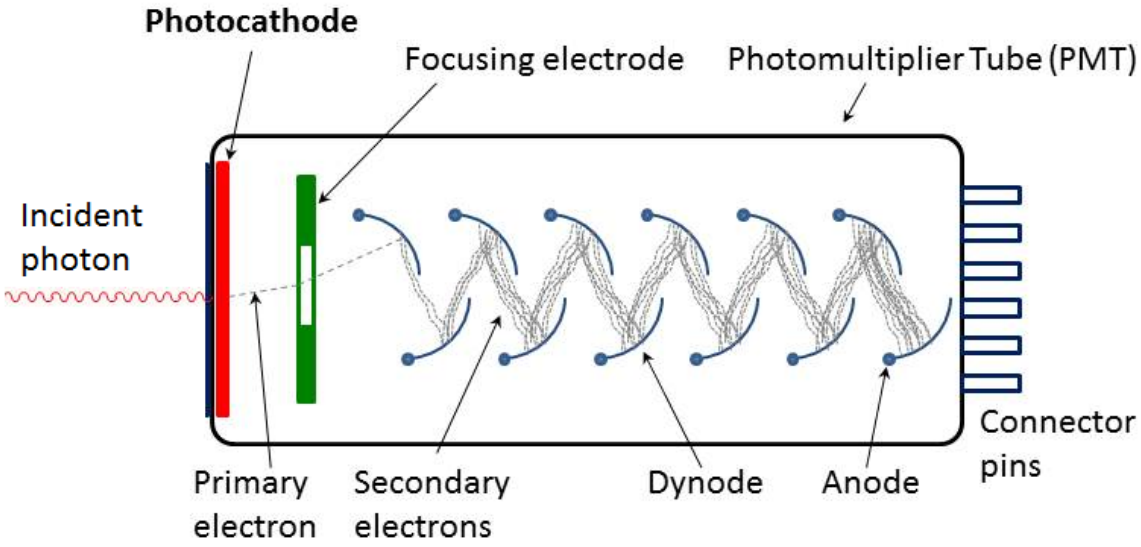

Figure 3.17: Photo-multiplier tube (PMT) schematic. A PMT is a vacuum tube used to detect photons, basically multiplying the initial current produced by an incident photon. Source: `https://en.wikipedia.org/wiki/Photomultiplier`

3.4.7 Electronics

The electronics is located in the back part of the optical box. A custom electronic card was designed to power the PMTs and allow discrimination of the output signal (see 3.18). The electronic board is powered with a $5\,V$ source. The board receives the signal from the PMTs and discriminate the real signal from the noise. Indeed, thermal electrons are emitted from the photocatode and the dynodes inside the PMT. The discriminator present on the board cuts signals smaller than $10\,mV$. The real signals are digitized and sent to the scaler through the SuperLemo connectors present on the board.

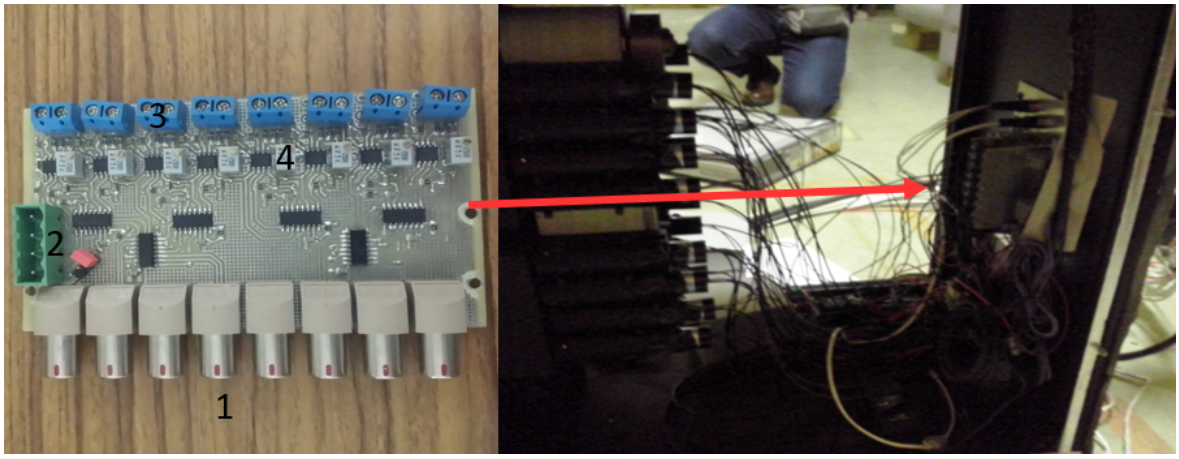

Figure 3.18: The electronic board was designed to power the PMTs and allow discrimination of the output signal. The relevant elements of the board are: 1)SuperLemo connectors; 2)Low Voltage (LV) power +/- 5V; 3)Photo-multiplier tube connection; 4)Discriminator 10 mV.

The SuperLemo connectors are accessible through an external panel located in the back of the optical box, as shown in Figure 3.19. We have already said that we electrically insulated the box from the optical channel, using some rubber gaskets and plastic screws. As a security measure, we also decided to insulate the external panel from the box using screws covered with plastic. The panel shows many connectors. One of the connectors is used to remotely control the conveyor belt. Another connector is used to power the conveyor belt and a modem located on the top of the box. Then, we have the output from the PMTs, which is sent to our scaler through Super Lemo cables, special cables using the low-voltage differential signaling (LVDS) standard. Finally, we have the connections for the High Voltage (HV), which goes to supply the potential required for the operation of the PMTs.

3.4.8 External box

In order to shield the boxes from parasitic light and therefore lower the pedestal rates, it is necessary to cover the optical box using an external aluminum box. The

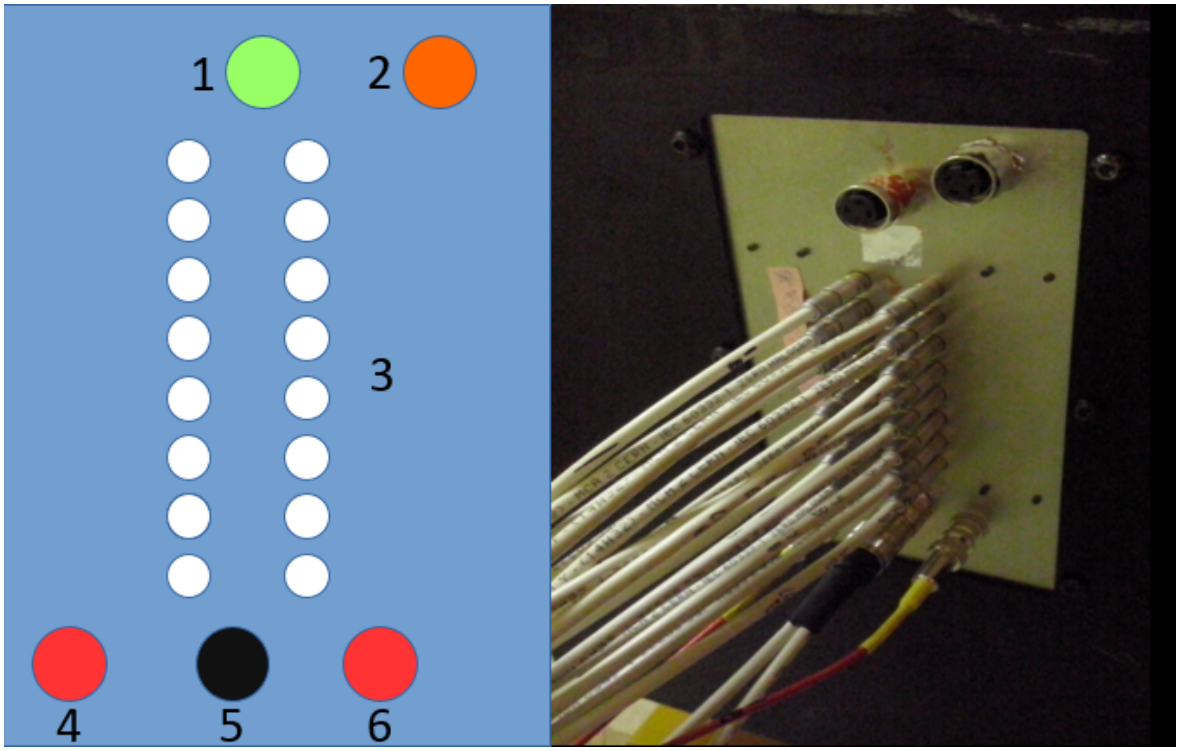

Figure 3.19: Back panel of the electronic board: 1)Conveyor belt control; 2)110 V power; 3)SuperLemo connectors, the output is sent as low-voltage differential signaling (LVDS); 4)High Voltage (HV); 5)Not used in commissioning phase; 6)HV.

external box was realized assembling a frame and covering it with robust aluminum foils of thickness $1\,mm$. This arrangement allowed to cut down the rates of an order 10, respect to those obtained without external covering. The optical box without and with external covering is shown in Figure 3.20.

3.5 Data acquisition (DAQ)

The Data acquisition is located outside the radiation area, and it is connected to the LABM through very cables, reaching 50 meters of length. The LABM DAQ consists of a VMEbus (Versa Module Europa bus) crate, equipped with three modules that perform different functions (see Figure 3.21). The High Voltage (HV) board supply the high voltage needed for the photo-multiplier tubes (PMTs). During the

Figure 3.20: The optical box, shown without covering on the left, and with covering on the right.

commisioning phase, a $1380\,V$ voltage was supplied to the PMTs. Then we have a scaler board, which receives the train of digitized pulses coming from the disciminator. The scaler is an instrument that counts the number of pulses within a certain interval of time. Our scaler can work up to $5.0\,MHz$, meaning that it counts all the pulses coming within a $5\,\mu s$ interval. The collision frequency of SuperKEKB is $250\,MHz$, and therefore the scaler will integrate over 50 collisions. A controller board connects the crate to a computer through an optic fiber. A control software from CAEN (GECO 2020) is used to set the current and HV for the PMTs.

3.6 Mirrors and conveyor belt remote control

The conveyor belt is connected to a modem, and the modem is connected to our computer through a long cable. KEK computers use Linux operating systems, and the software driver included with the conveyor belt was available only for Windows

Figure 3.21: Crate for Data acquisition: 1)High Voltage (HV) CAEN V6533; 2)V830 CAEN Scaler 32 channels; 3)CAEN V2718 controller, optic fiber. A3818 pci adapter.

operating systems. Therefore a custom script was written to move the conveyor belt. The computer also controls the stepper motors that move the primary and secondary mirrors in the optical channel. The computer sends the inputs to a motor driver, which sends an output signal to move the stepper motor (see Figure 3.22). As in the case of the conveyor belt, software drivers were not available for Linux operating systems, and therefore custom scripts were coded. The code was written to move the mirrors in single steps, or to perform scans made of many steps. All the scripts were gathered in a single DAQ software which is able to: 1) record PMTs rates continuously and saving data in a organized way; 2) Calibrate the PMTs by moving the conveyor belt in a series of established positions and record the PMTs rates at any step; 3) Performing 2D scans of the IP by moving primary and secondary mirrors according to a user specified 2D array, and recording the PMTs rates at each position of the array.

Figure 3.22: Remotely controlled mirrors: 1)Input cable from the computer to the motor drivers; 2)Motor drivers; 3)Output cable from the motor drivers to the stepper motors; 4)Stepper motor inside the primary elbow; 5)Primary elbow.

3.7 IP resolution

The LABM optical channel constitutes a telescope pointing at the interaction point. This design, with long pipes, allows to focus the apparatus toward a small spot from which the BS light is collected. This spot, located on the plane transverse to the beam pipe at the IP, is distant about 5 meters from the vacuum mirror, and about 15 meters from the optical box. Carrying the analogy further, the objective of the telescope is the vacuum mirror, and the eyepiece is a collimator that is installed in the last elbow before the optical box (see Figure 3.23). Although the collimator in Figure 3.23 is rounded, the newest version is a square. When the collimator is not inserted, the collimating element becomes the Wollaston prism, with a squared area of side $19\,mm$.

The vacuum mirror has an effective area of $2 \times 2\,mm^2$, the collimator has an area of $7 \times 7\,mm^2$. The knowledge of these areas allow to estimate the size of the spot at the

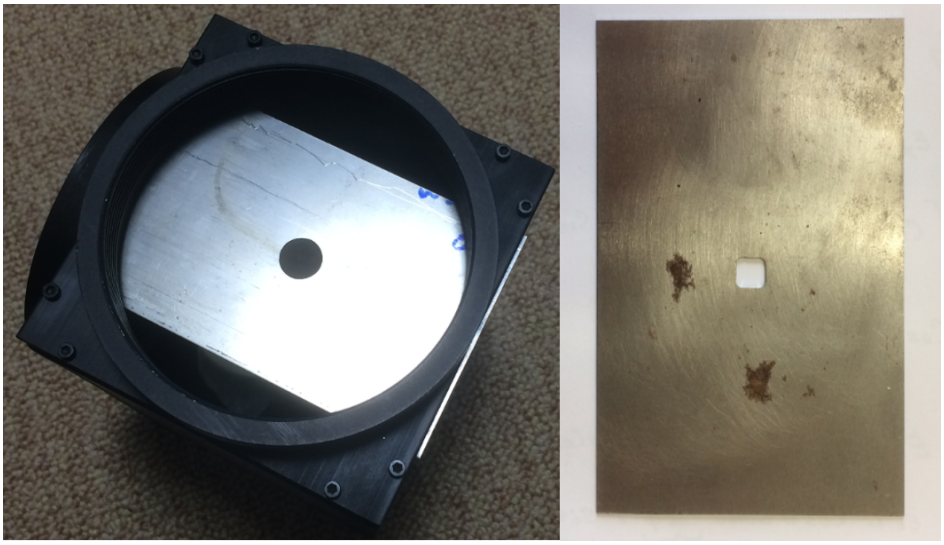

Figure 3.23: Rounded collimator inserted in the elbow on the left. Final design of squared collimator on the right. The collimator is used to improve the spacial resolution of the LABM and to reduce the rate of photons arriving at the box.

IP from which the LABM collects the BS light, in other words the space resolution. Given the schematic of Figure 3.24, with y_1 half side of the collimator, y_2 half side of the vacuum mirror, x_1 distance of the collimator from the optic box, and x_2 distance of the vacuum mirror from the optic box, the half side of the spot at the IP is $\mid y_3 \mid$, with y_3 given by 3.2:

$$y_3 = -y_1 + \left[\frac{y_2 + y_1}{x_2 - x_1}\right](x_3 - x_1) \tag{3.2}$$

With $x_1 = 0\,m$, $x_2 = 10\,m$, $x_3 = 15\,m$, the result is $y_3 = 3.25\,mm$. Therefore, the area of the spot at the IP is $6.5 \times 6.5\,mm^2$.

3.8 LABM observables

The LABM measures the polarization and spectrum of the BS light. From Figure 3.12 we can see that each PMT measures a certain color and polarization. From these measurements it is possible to calculate some significant asymmetries that give

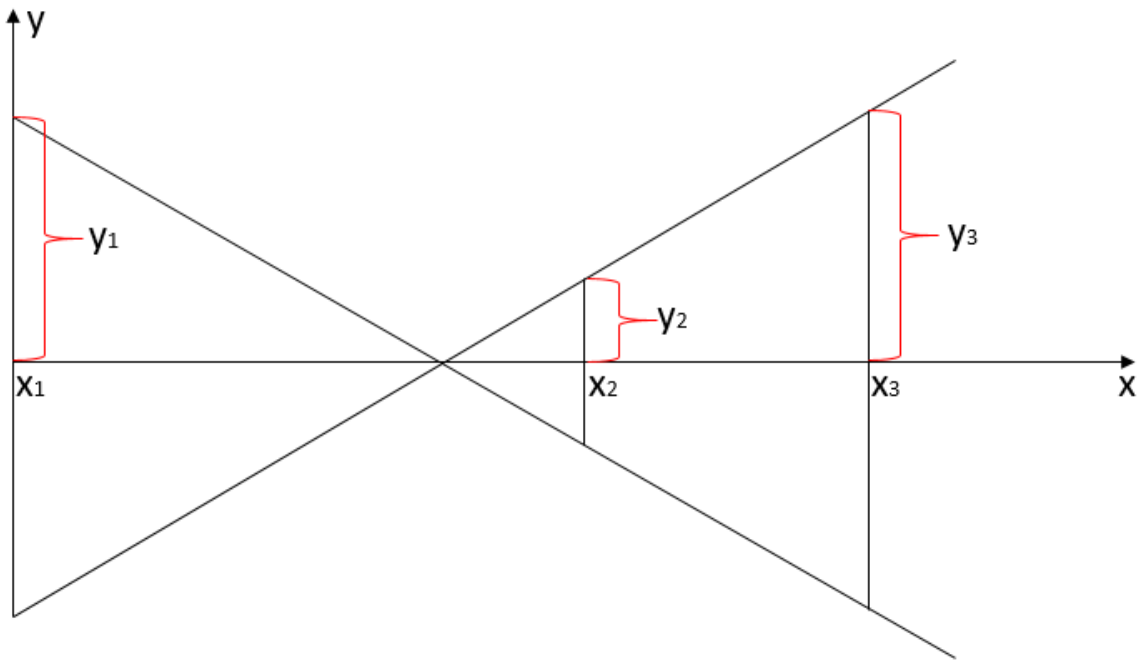

Figure 3.24: Estimation of the IP resolution for the LABM. y_1 is half of the side of the collimator. y_2 is half of the side of the vacuum mirror. y_3 is half of the side of the spot at the IP.

information about the size and position of the beams. The beams collision may present a series of pathologies that cause a decrease of the luminosity. For example, the beams may present an offset, or one beam could be smaller than the other, or the collision can take place at an angle. To illustrate these pathologies, let us consider the case of equal and collinear beams colliding head on. At SuperKEKB the beams collide at a crossing angle, but the case of collinear beam remains an instructive one. The pathologies for collinear beams are shown in Figure 3.25.

The LABM allows instantaneous measurements of the BS coming from the IP. If the beams have a vertical offset (Figure Figure 3.25 on the left), the y polarization is larger than the x polarization. The Optics box measures the intensity in both polarizations; therefore, we can measure the offset parameter, which is:

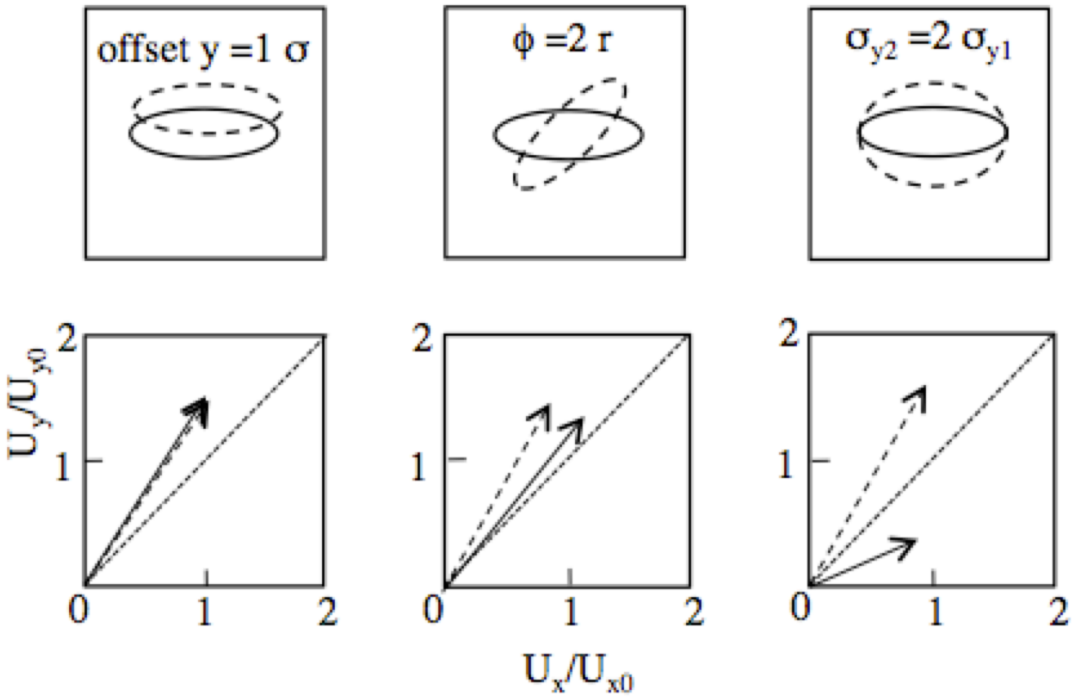

Figure 3.25: Pathologies presented by colliding collinear beams. When the collision is not perfect, the energy in the x and y polarizations show a well determined pattern: 1)Beams offset on the left; 2)Beams tilted on the center; 3)One beam embedded inside the other on the right.

$$A_1 = \frac{U_y - U_x}{U_y + U_x} \tag{3.3}$$

Incidentally, seismic motion may cause an offset between the two beams, LABM could be used to measure the motion of the ground. In the case of one beam embedded inside the other (Figure 3.25 on the right), the LABM is the only device that can identify the pathology by measuring the asymmetry parameter of interest, which is:

$$A_2 = \frac{U_{y_1}}{U_{y_2}} - 1 \tag{3.4}$$

Then, there is the case of one beam rotated respect to the other (Figure 3.25 on

the center). In this case, the parameter of interest is:

$$A_3 =\mid sin(U_1, U_2) \mid \tag{3.5}$$

In addition, the spectral separation in four colors allows the direct measurement of the length of a bunch. For collinear beams, the intensity at a given angle and wavelength is [13]:

$$\frac{d^2U}{d\Omega d\lambda} \propto exp\left[-\left(\frac{\pi\sigma_z\theta^2}{\lambda}\right)^2 \right] \tag{3.6}$$

Fitting the spectrum obtained with the function 3.6, the length of the bunch σ_z is obtained. The LABM can also be used to check the alignment between the beam and the beam pipe. Indeed, if beam and beam pipe are parallel to each other, the average number of photons that reach the up mirror must be equal to the number of photon that reach the down mirror. The relative asymmetry parameter is:

$$A_{ud} = \frac{U_u - U_d}{U_u + U_d} \tag{3.7}$$

If we consider a long time interval, the average of the quantity A_{ud} has to be zero if beam and beam pipe are parallel to each other.

CHAPTER 4 DATA TAKING AND ANALYSIS

Once the LABM was completely installed and all components tested, we started the calibration of the device and data taking. The calibration of the device took place in November 2015, when we used a white and unpolarized light source to measure pedestals and efficiency of the optical channel. The real data taking started in February 2016, when SuperKEKB started circulating the beams in its commissioning phase. Although there were no collision in this phase, we were able to use the LABM to collect the synchrotron radiation (SR) emitted by the beams while progressing through the bending magnets, located few meters before the IP (see Figure 4.1).

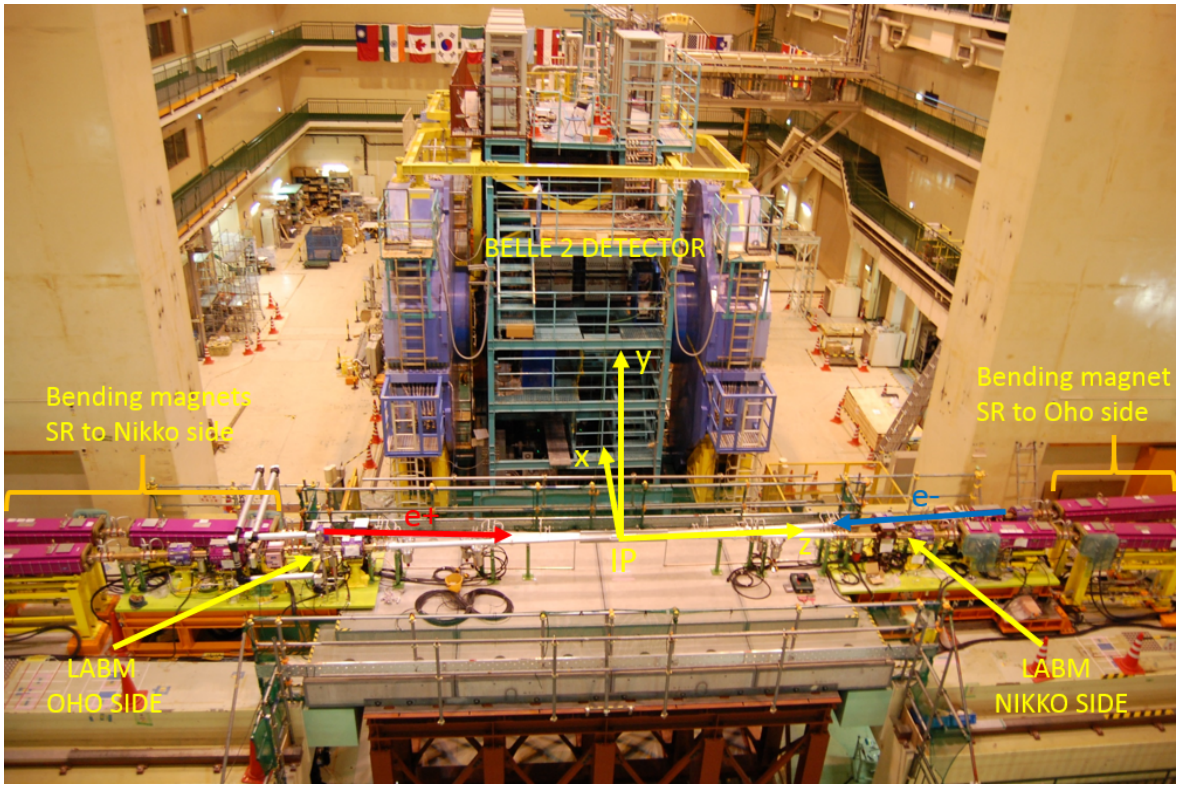

Figure 4.1: Coordinate frame at the IP: this frame will be used, in the following, to present the results. On the sides, we see the bending magnets responsible for the emission of synchrotron radiation.

4.1 Conventions used

The LABM is divided in two sides: the Nikko side measures the radiation emitted by the positron beam; the Oho side measures the radiation emitted by the electron beam. On each side, the light is extracted through two windows located on the beam pipe, one on the top and one on the bottom. The corresponding measurements are referred as Up and Down. The light is then separated in polarization and spectrum, so that the LABM is able to take 32 independent measurement through an equal number of PMTs. The PMTs are numbered, from 0 to 31, in the following way:

Oho Up, light X polarized: 4 (ultraviolet), 5 (violet), 6 (green), 7 (red);
Oho Up, light Y polarized: 0 (red), 1 (green), 2 (violet), 3 (ultraviolet);

Oho Down, light X polarized: 8 (red), 9 (green), 10 (violet), 11 (ultraviolet);
Oho Down, light Y polarized: 12 (ultraviolet), 13 (violet), 14 (green), 15 (red);

Nikko Up, light X polarized: 24 (red), 25 (green), 26 (violet), 27 (ultraviolet);
Nikko Up, light Y polarized: 28 (ultraviolet), 29 (violet), 30 (green), 31 (red);

Nikko Down, light X polarized: 16 (red), 17 (green), 18 (violet), 19 (ultraviolet);
Nikko Down, light Y polarized: 20 (ultraviolet), 21 (violet), 22 (green), 23 (red).

The X and Y coordinates refer to the polarization of the light in the beam pipe, according to the reference system used in 4.1. The light, before being measured, travels inside the optical channels, and therefore the polarization changes. At the optical box, we actually measure, always according to the reference system used in 4.1, the Z and Y polarizations of the light. However, the polarization was mapped with a computer simulation, so that we know how to convert the polarization measured at the box to

the actual polarization inside the beam pipe. The relation between the polarization in the beam pipe and that measured in the optical box is:

Nikko up $(x, y)_{beampipe} \rightarrow (z, y)_{box}$

Nikko down: $(x, y)_{beampipe} \rightarrow (z, y)_{box}$

Oho up: $(x, y)_{beampipe} \rightarrow (y, z)_{box}$

Oho down: $(x, y)_{beampipe} \rightarrow (z, y)_{box}$

We notice that the Oho up mapping for the polarization differs from the other channels, due to a different configuration of the optical channel.

4.2 Pedestals and calibration

The first measurements were taken without any light source, in order to measure the pedestals for the rates. The pedestals were first measured during summer 2015, right after assembling the LABM for the first time. Initially the optical boxes did not have an external box for shielding from parasitic light, as shown on the left of Figure 3.20. The pedestals were quite high, and we decided that it was important to realize an external aluminum box, shown on the right of Figure 3.20. To appreciate the decrease of the pedestals, the rates for some of the PMTs are shown in Table 4.1 before and after this upgrade.

PMT number	Rates before (Hz)	Rates after (Hz)
0	1096.8	90.1
1	2309.4	87.7
2	5674.5	60.7
3	1027.9	72.7

Table 4.1: Comparison of pedestals before and after upgrading with an external aluminum box.

We notice that the pedestals, after using an external box, dropped by a factor

varying between 10 and 100 depending on the PMT. The pedestals are now included in the software that records the data, and therefore all the measurements presented in the following are already pedestal subtracted. Once the pedestals were measured, we started taking measurements with an unpolarized white light source in order to calibrate the LABM and calculate the relevant efficiencies. The rates were measured while rotating the conveyor belt in 12 different positions. This is equivalent to 12 different configurations of the PMTs, of which one is the nominal position. In the other 11 configurations each PMT is moved in the position hold by another PMT in the nominal configuration. This enables to calculate the relative efficiencies among PMTs and among optical channels through a 24 parameter fit. The result is that the efficiencies of the PMTs differ at most by 30%, while the efficiencies of the optical channels differ at most by 10%. These efficiencies are taken into account in the analysis of the measured data.

4.3 Data taking

The LABM was continuously recording the rates during the commissioning phase of SuperKEKB, and therefore we were able to take measurements since the first time the positron beam was circulating, on February 10, 2016 (See Figure 4.2).

The LABM took data continuously from February to June 2016, during the SuperKEKB commissioning phase. During this period it was decided to have no collisions, and therefore no BS light was recorded from the LABM. However, due to the arrangement of the IP, with a pipe much larger of the one that will be used in the final configuration, it was possible to observe synchrotron radiation (SR) emitted by the beams when they were bent within some bending magnets near the IP (See Figure

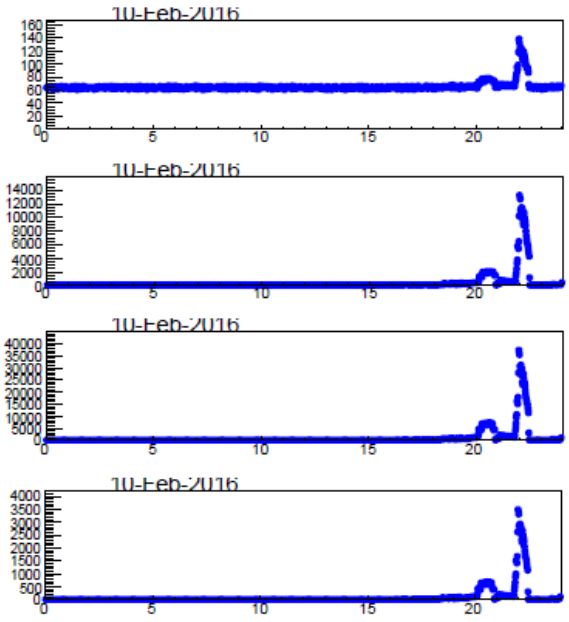

Figure 4.2: First rates measured by four of the PMTs of the LABM in February 2016. Time (hour) on the horizontal axis. Rate (Hz) on the vertical axis.

4.1). The measurements of SR radiation in the commissioning phase allowed us to test the whole apparatus, as we will show in the following. The first thing to do was to prove that the signal measured was really radiation emitted by the beams, and not some sort of noise. The LABM is connected to the EPICS framework of SuperKEKB. EPICS is a software environment used to control and communicate with the hardware in high energy experiment facilities. Therefore, we were able to access all the significant parameters of the accelerator, among which the real time measured current of the beams. Then, it was possible to correlate our measurements of the rates with those of the currents. The rates measured on the Oho side are correlated to the HER current, while those measured on the Nikko side are correlated to the LER current. Figure 4.3 shows the rate-current correlation for two of the PMTs.

From Figure 4.3, on the left, we see how the values of the rates perfectly superim-

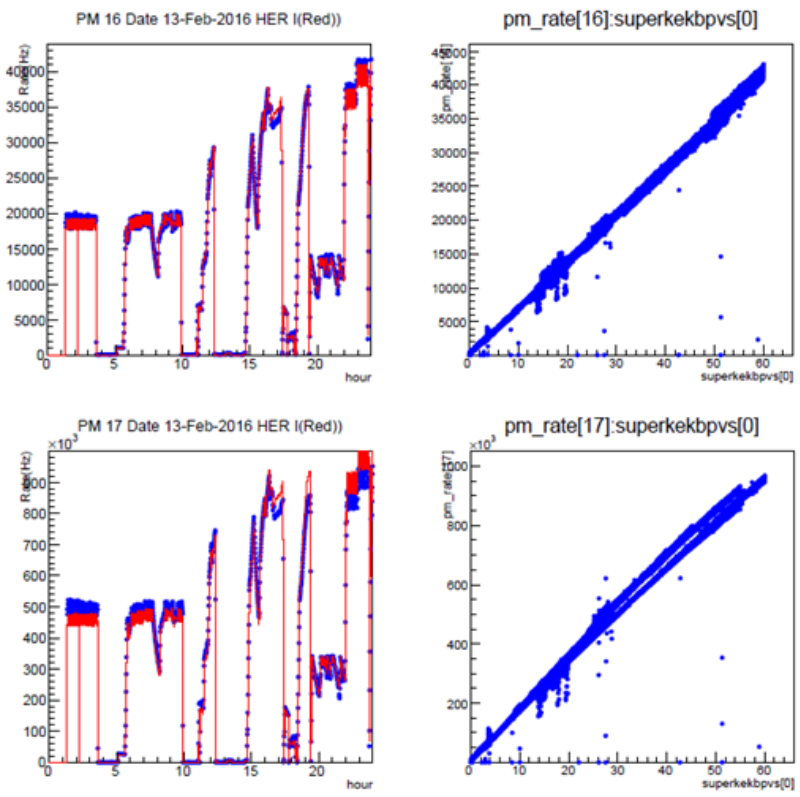

Figure 4.3: Rate-current correlation for PMTs 16 and 17. Rate (blue) and current (red) superimposed on the left. Time (hour) on the horizontal axis. Rate (Hz) on the vertical axis. Rate versus current on the right. Current (A) on the horizontal axis. Rate (Hz) on the vertical axis. We notice that the signal from the PMTs is linearly correlated to the current of the radiating beam.

pose with the values of the current. In particular, from Figure 4.3, on the right, we can appreciate how the rate-current correlation is linear. This fact definitely proved that what we were observing was really radiation emitted by the beams. During the commissioning phase, the current for the beams was initially a few mA, but over time reached the value of almost $1\,A$, not so far from the nominal current values given in Table 2.2. Soon we noticed that the rates were very high, dangerously close to our saturation limit of about $10\,MHz$, and therefore we needed to use a countermeasure. We decided to install a collimator of diameter $15\,mm$ inside the last elbow before the optical box (see Figure 3.23). Then, we gradually moved smaller collimator of diameter

to 12 mm, and finally to 8 mm. The final design of the collimator will be a square of side 7 mm 3.23. This decrease in the collimator's diameter is explained by the current increase. We progressively went to smaller collimators because we wanted to be sure to collect enough light. In Figure 4.4 we see the rate drop caused by passing from a 12 mm to a 8 mm collimator. The beam current, 60 mA, was the same in the two intervals of time, and we see how the rates drop to about 1/3 of the initial value.

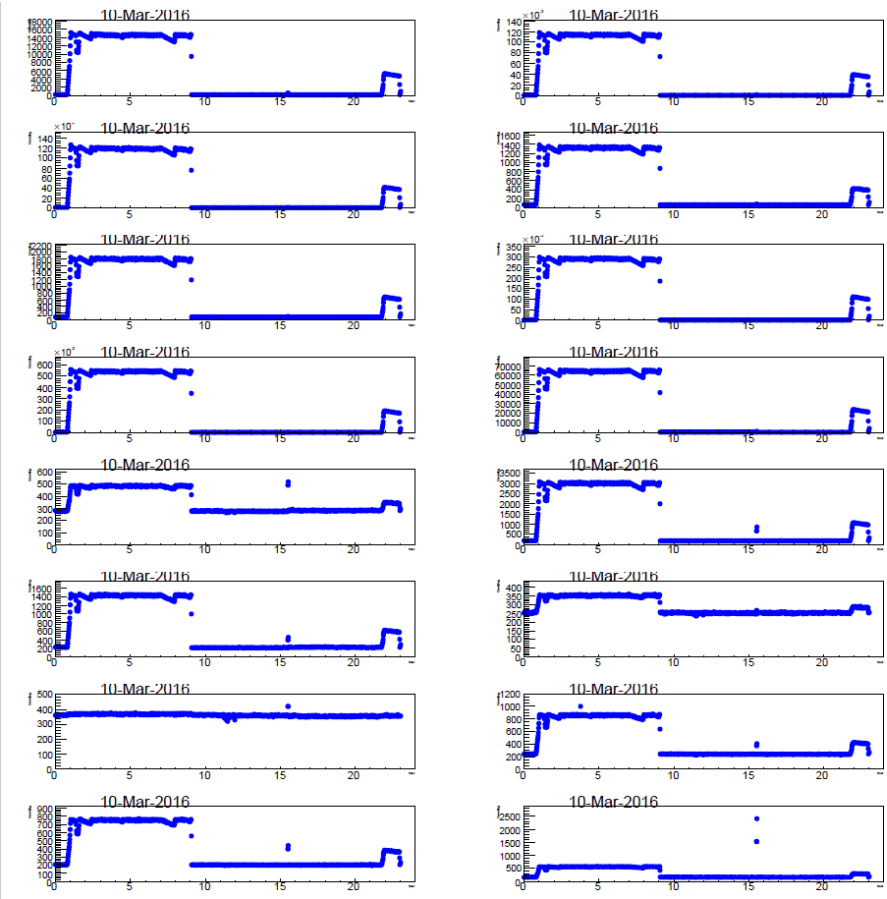

Figure 4.4: The rates measured in passing from a 12 mm to a 8 mm collimator. We notice that the rate, for the same current of the radiating beam, drop to about 1/3 of the initial value. Time (hour) on the horizontal axis. Rate (Hz) on the vertical axis.

4.4 Angular scans

In the commissioning phase, we used the LABM to scan the solid angle inside the beam pipe, while measuring the SR. From the analysis of these 2D scans it is possible, in principle, to identify the position of the IP. It is also important to study the SR in order to understand the background, even if a smaller beam pipe in the final configuration of the IP is expected to block SR and allow observation of only BS light. The rates measured will vary during the scan, and the imagine produced enables to find where the light comes from.

However, during the commissioning phase the currents were often changed and so the rates, due to the linear dependence of the two quantities. As a result, during an angular scan, the rate R would change with dependence on both the current I and the observed angular position (δ_x, δ_y). To isolate the rate dependence from the angular position, it was decided to plot the ratio R/I instead of just rate. To perform an angular scan, we can decide to move either the primary or secondary mirror. We have tested angular scans with both mirrors, and we have obtained the same images. The advantage is that if either the primary or the secondary mirror gets stuck, it is possible to continue running scans by using the other one.

The conversion from angular displacement to X-Y coordinates on the plane transverse to the beam pipe at the IP has been calculated and embedded in our DAQ software. Therefore, our 2D scans can be plotted in angular displacement (δ_x, δ_y) or position (X, Y) at the IP. After many runs, it was decided that the best way to perform the scan, in terms of time and resolution, was to collect light from an angular region

large about $20 \times 20\, mrad^2$ and divide this region in a grid of 26×41 boxes. The DAQ software would move the mirror in such a way to observe each one of this boxes, take five measurements of R/I per box, and record the average before going to the next box. Each measurement takes about 1 second and there are 5 measurements per step.

Therefore, in order to complete a scan with $26 \times 41 = 1066$ steps, it takes about 90 minutes in measurements. Considering also the dead time necessary to move the mirror from one step to the other, a complete scan lasts about 2 hours. However, once the IP is identified, the mirrors can be moved in their final position and no other scans are required. The first scans were performed without collimators. In this case it is the first element in the box, the Wollaston prism, which acts as a squared collimator of side $19\, mm$. Later, when we identified the first structures in the angular scans, we moved to smaller collimators, thereby allowing an improved angular resolution. The results presented in this thesis were obtained with a rounded collimator of radius $8\, mm$.

4.5 Large angle synchrotron radiation

Before getting into the analysis of the scans, let us review the polarization and spectrum properties of the SR. According to classical electrodynamics, the asymptotic expression for the energy per unit of frequency and elevation angle above the trajectory of the emitting charged particle is [5]

$$\frac{d^2U}{d\omega d\psi} \sim \frac{e^2}{\pi c}\left(\frac{\omega\rho\psi}{c}\right) exp\left(\frac{-2\omega\rho\psi^3}{3c}\right) \tag{4.1}$$

According to Eq. 4.1, there is no net polarization at large angle. In our notation the elevation angle ψ corresponds to θ, and therefore the latter symbol will be used in

the following. It is possible to rewrite this equation using the length of the magnet L, the power P, and total energy emitted U, using the following substitutions [14]:

$$d\psi = 4\pi d\theta \ ; \ (1+\gamma^2\theta^2) \sim u^2 \ ; \ \omega \sim \frac{3ct}{\rho\theta^3} \tag{4.2}$$

The result obtained using the variables defined in 4.2 is:

$$\frac{d^2U}{dudt} \sim \frac{54\pi U\rho}{L}\left(\frac{t}{u^5}\right)exp(-2t) \tag{4.3}$$

In treating SR, it is possible to define a cone of aperture $\theta_0 = 1/\gamma$, within which at least half of the power is emitted [15]. The quantity γ is defined as

$$\gamma = \frac{E}{mc^2} \tag{4.4}$$

where E and m are are the energy and mass of the emitting particle. The comparison between the elevation angles for SR measured from LABM and θ_0 is shown in Table 4.2.

Side	$\theta(mrad)$	$\theta_0 = 1/\gamma(mrad)$	θ/θ_0
Oho	3.2	0.0714	44.8
Nikko	4.2	0.125	33.6

Table 4.2: Comparison between $1/\gamma$ angle and elevation angle.

Since $\theta \gg \theta_0$ for our purposes, we can use the so called short magnet approximation (SMA), which can be only applied at very large angles. The formulas obtained in the SMA give a polarization pattern in the azimuthal coordinate ϕ, which has been defined in the previous paragraph. The formulas for the SR intensities in the x and y

polarization are [14]:

$$\frac{d^3U_x}{dudtd\phi} \sim \frac{48U\rho}{\pi L\gamma}\frac{cos^2(2\phi)}{u^4t^2} \tag{4.5}$$

$$\frac{d^3U_y}{dudtd\phi} \sim \frac{48U\rho}{\pi L\gamma}\frac{sin^2(2\phi)}{u^4t^2} \tag{4.6}$$

From equations 4.5 and 4.6 it is possible to derive some conclusions on the SR emitted in the bending magnet and collected by the LABM. Let us consider the SR that arrives directly at the vacuum mirror without reflections on the internal wall of the beam-pipe. Looking at Figure 4.5 and Table 4.5, we see that the intensity of the Y polarized SR decreases as the emitting particle travels inside the bending magnet.

The last piece of SR radiation, when the particle is about to exit from the magnet (emission 3 in Figure 4.5), is emitted at $\phi = \pi/2$ and therefore will have negligible Y polarization.

Other cases of interest are SR emitted at $\phi = \pi/8$ or $\phi = \pi/4$. In the first case we will have no net polarization, in the second case we will have only Y polarization. The SMA approximation is not exactly true for bending magnets of length 2 m. However, the general dependence of the polarization from the azimuthal angle ϕ is retained.

4.6 Bending magnets

The SR collected by the LABM is emitted when the beams are bent while traveling inside the bending magnets (BM) near the IP, as shown in Figure 4.5. The image was purposefully exaggerated to make clear the process. The real BM producing the SR, are shown in Figure 4.1. The properties of the two BMs closest to the IP, on each side

of Figure 4.1, are listed in Table 4.3.

Magnet	$\rho(m)$	L (m)	d+D (m)	$\theta(mrad)$
BCLWRP(LER)	148.686	2.119	9.37	4.2
BLC1LE(HER)	609.065	3.49	12.11	3.2

Table 4.3: Bending magnets parameters. $\rho(m)$ is the bending radius, L the length of the magnet, d is the horizontal distance between the IP and the LABM, D is the distance between the magnet and the IP, θ is the angle of the LABM above the beam line as seen from the bending magnet (see 4.10).

The SR is collected at a certain angle θ between the direction of the instantaneous velocity of the beam and the observer (LABM). The instantaneous direction of the velocity is indicated in the upper part of Figure 4.5 at three instants: 1, when the beam has just entered the magnet; 2, when the beam is at about the center of the magnet; 3, when the beam is about to exit the magnet. The top of the Figure shows the angles in the x direction, while the bottom shows the angles in the y direction. Since the intensity of the SR depends on the angle of observation θ, it is interesting to understand if θ increases or decreases in going from 1 to 3. This will be important to identify the SR coming from the points along the trajectory of the beam. We know that $\theta_{x,3} \approx 0$, while $\theta_{x,1} = L/\rho$ as a result of the bending. For the y direction we have $\theta_{y,3} \approx h/(D+d)$, while $\theta_{y,1} \approx h/(L+D+d)$. Also, for small angles, we can calculate the total observation angle as $\theta \approx \sqrt{\theta_x^2 + \theta_y^2}$. The relevant angles for 1 and 3 are given in Table 4.4.

We notice that $\theta_3 < \theta_1$ in all four channels. It is well known that the intensity of the observed SR decreases with increasing observation angle, and therefore the SR is expected to increase in going from 1 to 3. Moreover, we are always in the large angle regime for SR, and therefore we can use Eqs. 4.5 and 4.6. To exploit these equations,

Side	$\theta_{x,1}$	$\theta_{y,1}$	θ_1	$\theta_{x,3}$	$\theta_{y,3}$	θ_3
Oho Down	5.73	2.56	6.28	0	3.30	3.30
Oho Up	5.73	2.56	6.28	0	3.30	3.30
Nikko Down	14.25	3.48	14.67	0	4.27	4.27
Nikko Up	14.25	3.48	14.67	0	4.27	4.27

Table 4.4: Observation angles. All values in $mrad$.

let us calculate the azimuthal angle. We can define ϕ as the azimuthal angle respect to the direction of the velocity of the emitting particle. From Figure 4.5 we can estimate using $\phi \approx atan(\theta_y/\theta_x)$. The angle ϕ for 1 and 3 are given in Table 4.5. Since the azimuthal angle decreases from 156° or 166° to 90° in going from 1 to 3, we expect an increase of the polarization R_x/R_y according to formulas 4.5 and 4.6.

Side	ϕ_1	ϕ_3
Oho Down	156	90
Oho Up	156	90
Nikko Down	166	90
Nikko Up	166	90

Table 4.5: Azimuthal angles. All values in degrees.

4.7 Beam pipes and reflections

As mentioned above, the light coming into our telescope was SR emitted because of the bending magnets present near the IP. Therefore, we obtained complex structures due to both the SR properties and to reflections in the internal wall of the beam pipe. We need to take into account that the HER beam pipe is made of brushed aluminum, while the LER beam pipe has a special coating of TiN (titanium nitride). The reflectivities of TiN (Figure 4.6) and aluminum (Figure 4.7) are different and also depend on the polarization, which can be parallel (p-polarization), or perpendicular (s-polarization) to the beam pipe wall.

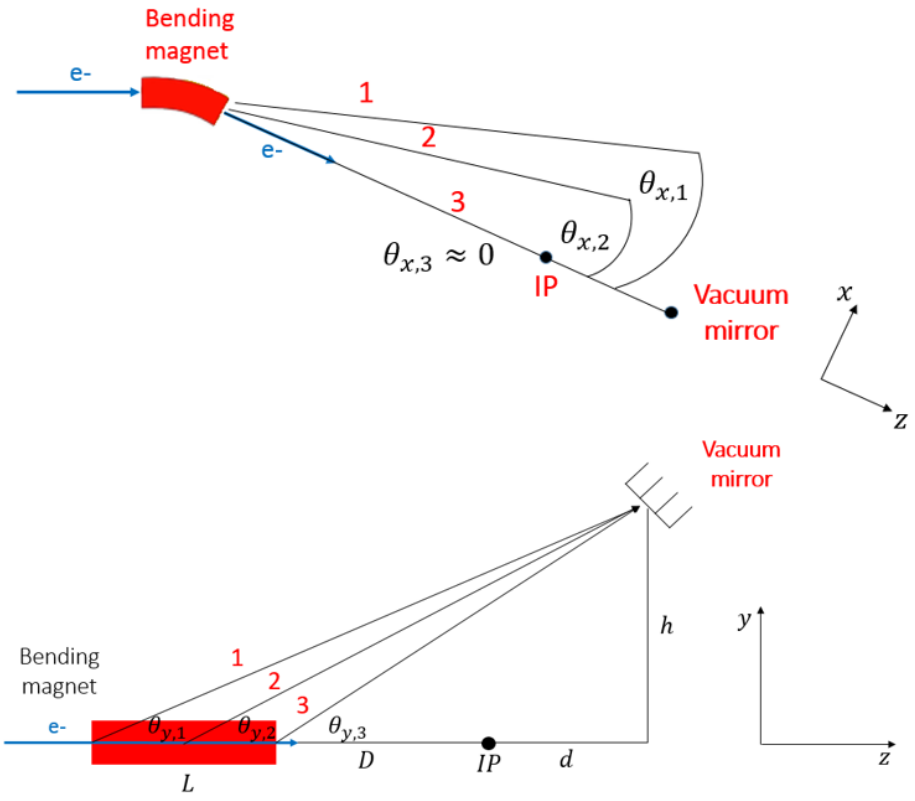

Figure 4.5: The beam emits SR while progressing through the magnet. The SR collected by the LABM is collected at different angles along the path. At the entrance of the bending magnet (BM) the angles are denoted by 1, in the center of the BM by 2, and the exit of the BM by 3. We are interested in the angles respect to the vacuum mirror. We have that the polar angle θ decreases during the progression, while the azimuthal angle at the exit of the magnet (3) is $\phi = \pi/2$. The result of radiation emitted by the beam while progressing inside the beam is a streak.

It is not possible to infer that the direct image will be the brightest structure observed in the scan. Because of the position of the vacuum mirror, the direct image of the beam is collected at large angle. Some of the reflections collected by the vacuum mirror might come from SR originally emitted at a small angle and then bounced off the pipe wall. Because of the properties of the SR, whose emissions are much more intense at small angle, those reflections might be brighter than the direct image. By the same token, the reflections do not become, due to the reflectivity dependence on the frequency, necessary redder than the direct image.

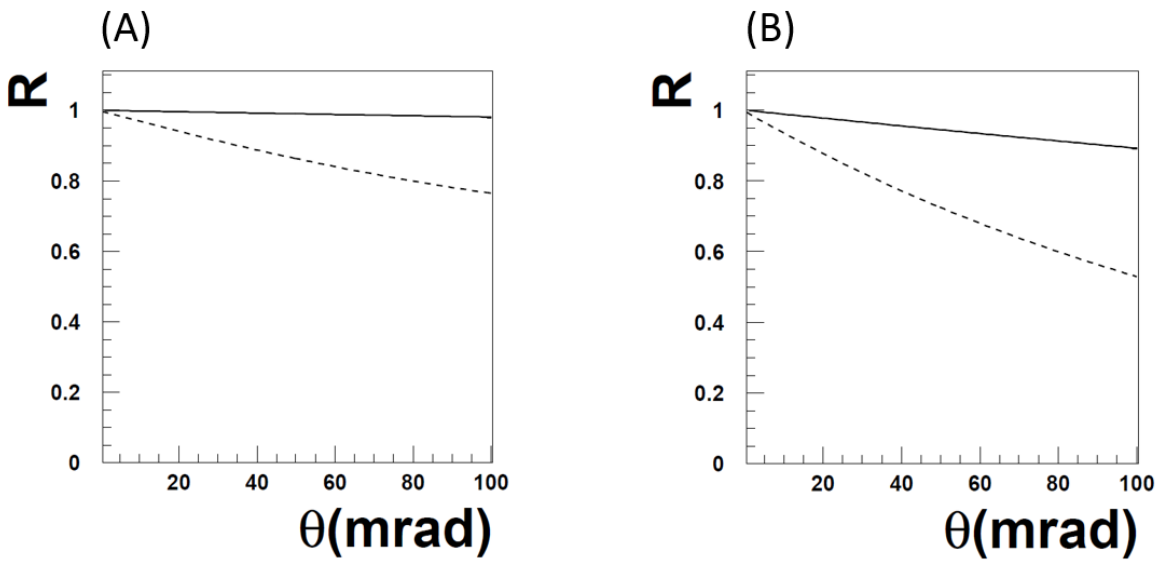

Figure 4.6: TiN reflectivity: (A) $\lambda = 650nm$; (B) $\lambda = 350nm$. The solid line is the s-polarization. The dashed line is the p-polarization.

Indeed, according to Eq. 4.1, a reflection emitted at small angle has a much larger blue component. The light reflected off the wall of the beam pipe tends to gain a net polarization parallel to the wall, as shown in Figure 4.6 and 4.7. However, if the light is emitted at azimuthal angle $\phi = \pi/8$, it is not certain that it will gain a polarization larger than the direct image. The reflections of azimuthal angle $\phi = \pi/8$ can be identified from the fact that, according to Eqs. 4.5 and 4.6, they do not show a net polarization.

Finally, we should expect the reflections coming from the external wall respect to the bending induced by the bending magnet. The position of these reflections can be calculated from Figure 4.8, which shows the section of the beam pipe. In this calculation, the vacuum mirror is located on the top of the beam pipe, corresponding to the down channels. The same calculation can be performed with the vacuum mirror on the bottom, corresponding to the up channels. The thick line represents the SR

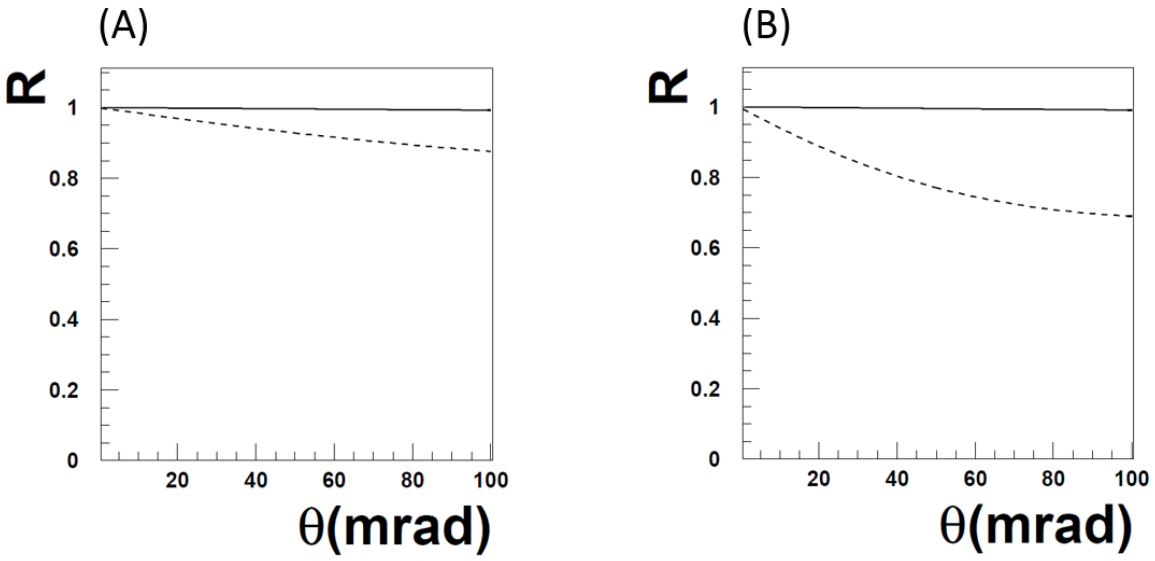

Figure 4.7: Aluminum reflectivity: (A) $\lambda = 650nm$; (B) $\lambda = 350nm$. The solid line is the s-polarization. The dashed line is the p-polarization

image of the emitting beam. The element of the image located at $x = 0$ corresponds to the beam exiting the magnet, which is the situation we have labelled with 3 in the previous paragraphs (see Figure 4.5). The element of the image located at $x = X$ corresponds to the beam inside the magnet. The element at $x = X$ can be reflected at angle $\varphi > 0$. From the figure, we find that:

$$\frac{X}{sin\varphi} = \frac{R}{sin\psi} \tag{4.7}$$

where R is the radius of the beam pipe and ψ is given by

$$\psi = \pi/2 - 3\varphi \tag{4.8}$$

Therefore, the equation regulating the reflections is:

$$\frac{X}{sin\varphi} = \frac{R}{cos(3\varphi)} \tag{4.9}$$

After some algebra, Eq. 4.9 can be written as

$$16a^2cos^6\varphi - 24a^2cos^4\varphi + (9a^2 + 1)cos^2\varphi - 1 = 0 \tag{4.10}$$

where $a = X/R$. Let us consider the solutions for $X = a = 0$, for which we have:

$$cos^2\varphi - 1 = 0 \tag{4.11}$$

The solutions to this equation are $\varphi = \pm\pi$ or $\varphi = 0$, the first one corresponding to the direct image and the second one to a reflection on the bottom of the beam pipe. Now let us consider the case $X > 0$. For the Nikko side, the length of the streak is about 3 cm. Since the radius R of the beam pipe is 4 cm, let us use the approximation $a \approx 1$. This simplifies the calculation,with the equation that becomes

$$16cos^6\varphi - 24cos^4\varphi + 10cos^2\varphi - 1 = 0 \tag{4.12}$$

The solutions to this equation are the angles $\pm\pi/8$, $\pm\pi/4$, $\pm3/8\pi$, $\pm5/8\pi$, $\pm3/4\pi$, $\pm7/8\pi$. However, due to the curvature of the pipe, we are only able to see the reflections on the external wall, corresponding to positive φ. Moreover, only the solutions with $\varphi < \pi/2$ are acceptable, as we can see from Figure 4.8. This reduces the physical solutions to $\pi/8$, $\pi/4$, $3\pi/8$. These solutions correspond to single, double and quintuple reflections. In the analysis of the scans, we will associate the reflections calculated in

this way to the actual structures found.

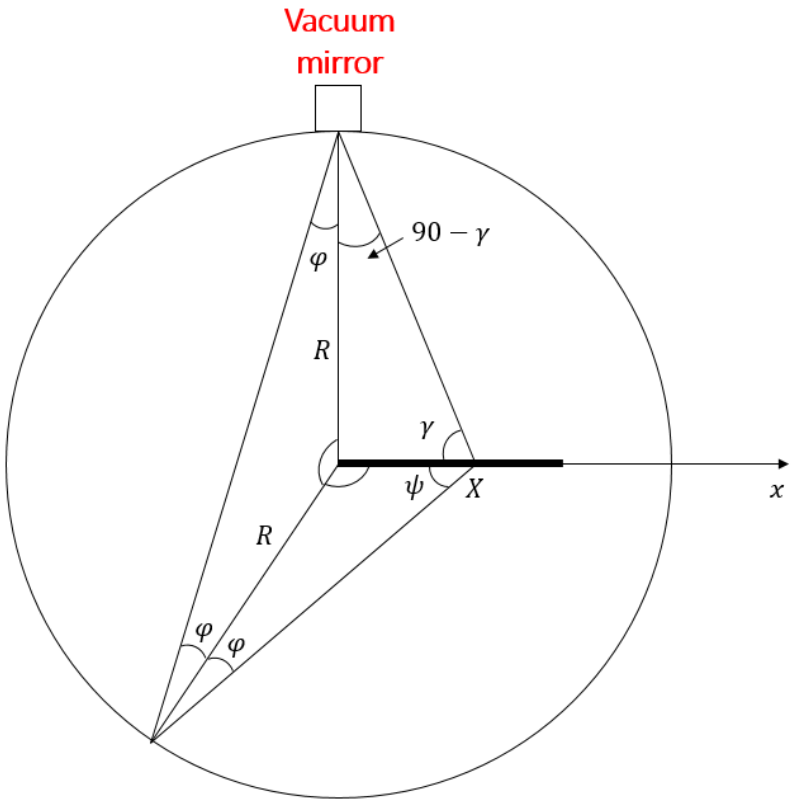

Figure 4.8: Figure for the calculation of the reflection angles inside a beam pipe of radius R. The thick line represents the streak produced by the radiating beam while progressing through the magnet. The reflection emitted by the X point of the streak is seen, from the vacuum mirror, at an angle φ.

4.8 Streaks and IP angle

4.8.1 Streaks

To analyze the scans produced we need to identify all the significant spots and streaks present in the image of the SR. The streaks are produced from a beam traveling along its path inside the bending magnet (BM), as shown in Figure 4.5. Of course, the streaks are in the horizontal (i.e., along X) direction with one end corresponding to the SR emitted at the entrance of the magnet (1 in Figure 4.5), and the other end corresponding to SR emitted when the beams exits the magnet (3 in Figure 4.5). At

the exit, the beam points toward the IP. Therefore, the IP will lie on the vertical of the point corresponding to SR emitted at the exit of the magnet. The length of the horizontal streaks can be calculated from Figure 4.9. The direct image will be a streak of length ϵ, subtending an angle:

$$\theta_s = \frac{\epsilon}{d + D + L/2} = \frac{L^2}{(d + D + L/2)\rho} \tag{4.13}$$

From Eq. 4.13, the direct image will be a streak subtended by an angle $1.4\,mrad$ for the Oho side and $2.9\,mrad$ for the Nikko side. Since the angular resolution of our telescope is about $1\,mrad$, we expect to resolve the image as a point-like structure for the Oho side, and as a streak for the Nikko side.

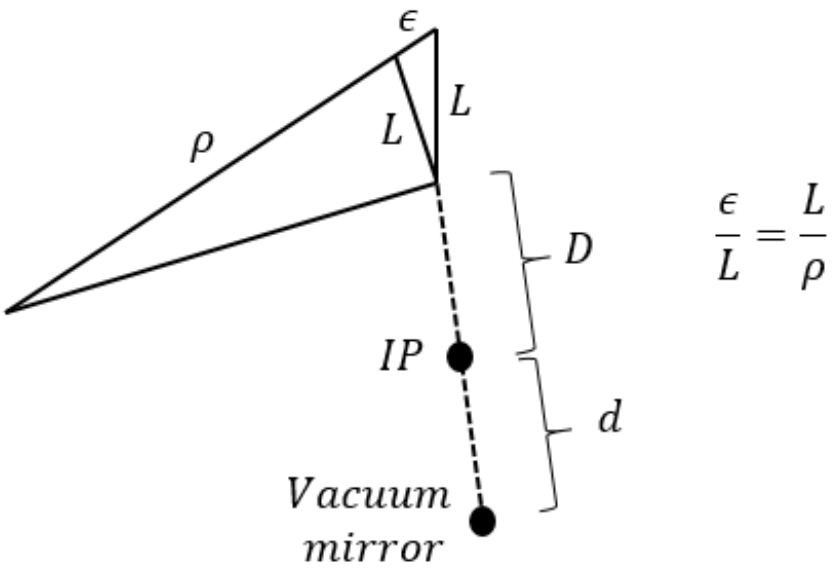

Figure 4.9: Schematic to find the length of the direct streak from the geometry of the interaction region. L is the length and ρ is the radius of curvature of the bending magnet.

4.8.2 IP angle

The position of the IP respect to the streak can be calculated. Let us calculate the position of the IP for one of the "down" channels, as shown in Figure 4.10. At the exit of the bending magnet, the SR collected from the LABM is emitted at an angle θ from the axis of the beam pipe. Let us assume that we have already found the position of the end of the streak, i.e., the position of the SR emitted when the beam exits the magnet (3 in Figure 4.5). Then, to find the position of the IP from the image of the scan, we need to move by an angle α in direction -Y. Analogously, for an "up" channel, we would need to move by an angle α in direction +Y. Using some trigonometric relations, it is possible to show that:

$$\alpha = \arcsin\left(\frac{D}{d}\frac{\sin\theta}{\sqrt{1+\frac{h^2}{d^2}}}\right) \tag{4.14}$$

where D is the distance from the edge of the bending magnet to the IP, d the horizontal distance from the vacuum mirror to the IP, and h is height of the vacuum mirror from the beam pipe axis.

In Table 4.6 all the relevant quantities are listed, and the calculated angle α for each channel is shown in the last column. In the following, the best scans obtained are shown, and an analysis of the relevant features is discussed. Of course, because we do not know the position of the IP before the scan, the origin of the axis is arbitrary.

4.9 Analysis of the angular scans

In this section I will discuss the best scans obtained, showing the most relevant images obtained. The image of the pipe at the IP will be superimposed to the scans.

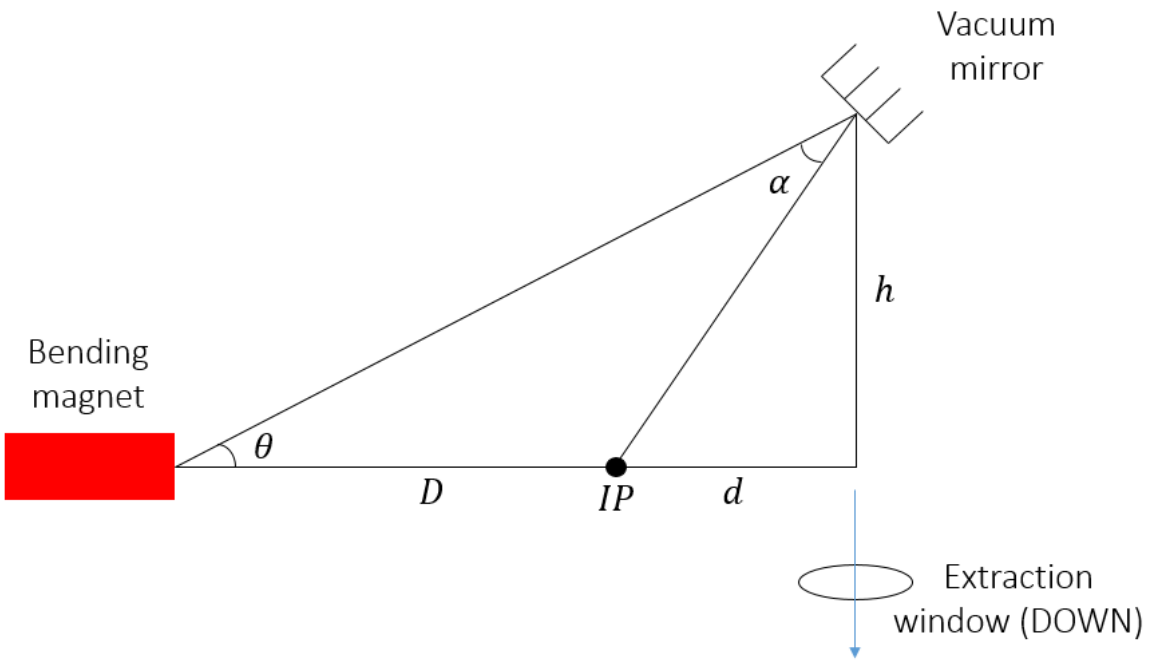

Figure 4.10: Schematic to find the angle α. The IP will be located at an angle α below the position of the bending magnet. The position of the bending magnet is identified with the position of the direct streak produced by the radiating beam while progressing through the magnet.

Channel	d (m)	D (m)	h (m)	$\theta\,(mrad)$	$\alpha\,(mrad)$
Oho Down	4.51	7.60	0.04	3.2	5.3
Oho Up	4.57	7.54	0.04	3.2	5.2
Nikko Down	4.77	4.60	0.04	4.2	4.1
Nikko Up	4.70	4.67	0.04	4.2	4.2

Table 4.6: LABM vacuum mirrors parameters.

Incidentally, the beam pipe superimposed to the scans looks like an ellipse because the scales are different for δ_x and δ_y. The diameter of the beam pipe at the IP is given in Table 4.7.

4.9.1 Nikko down

The best scan was probably obtained for the Nikko down channel. As already mentioned before, we need to find the end point of the direct streak, and then move

Channel	d	Diameter IP (m)	Diameter (mrad)
Oho Down	4.51	0.08	17.7
Oho Up	4.57	0.08	17.5
Nikko Down	4.77	0.08	16.8
Nikko Up	4.70	0.08	17.0

Table 4.7: Diameter of the beam pipe at the IP.

downward (in the negative δ_y axis direction) by an angle alpha. The images obtained with PMT 16 (red light X-polarized) and PMT 23 (red light Y-polarized) are shown in Figure 4.11. As mentioned before, the image obtained is somewhat complicated, consisting of many streaks. Of course, we need to identify which one is the direct image, and which are the reflections due to the beam pipe. We infer that the direct image of the beam is the streak identified as I, for a series of reasons that we now discuss.

First of all, the horizontal angular length has the correct size, estimated before to be $2.9\,mrad$ for the Nikko side. From Figure 4.5, we notice that the polar angle from the direction of motion of the beam to the position of the vacuum mirror decreases when the beam progresses through the magnet. Therefore, according to Eq. 4.1, the intensity of the SR collected by the LABM increases. The progression of the beam through the magnet is indicated by an arrow in Figure 4.11, and we can appreciate the expected behavior, with a total intensity that increases by 60%. Moreover, as the beam progresses along the magnet, the azimuthal angle ϕ changes from 166° to 90°, and therefore, according to Eq. 4.5 and 4.6, the polarization R_x/R_y should increase. Effectively, the polarization along the four pixel of the streak I in Figure 4.11 increases: the polarization R_x/R_y along the arrow is 9.3, 19.4, 29, 53. The other structures,

labelled as II, III, IV, V are reflections. According to the study of the reflection done in Section 4.7, to each reflection we can associate a corresponding azimuthal angle previously calculated. The reflections II, III, IV are associated respectively to $\varphi = \pi/8, \pi/4, 3\pi/8$. We believe that reflection V is a $3\pi/8$ reflection emitted inside the second-last bending magnet, which is shown on the extreme left of Figure 4.1. Finally, the polarizations of direct image and reflections follow the expected behavior: the direct image has a stronger X-polarized component, while the reflections have a polarization that depends on the azimuthal angle ϕ. We clearly notice that image I is the only image whose intensity, relative to the others, decreases in going from the image for X-polarization to that for for Y-polarization.

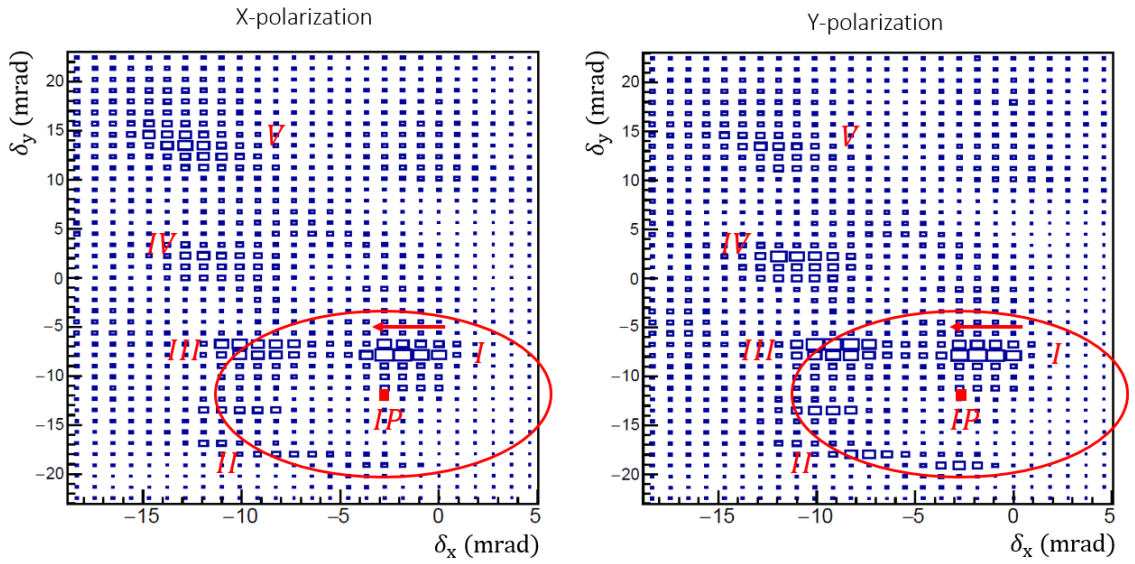

Figure 4.11: Nikko down scan. PMT 16 (red light X-polarized) on the left. PMT 23 (red light Y-polarized) on the right. The area of each cell is proportional to the intensity of the signal in arbitrary units. The red ellipse corresponds to the Beam Pipe Inner diameter at the IP. The direct image of the beam is the streak identified as I, while the structures labelled as II, III, IV, V are reflections. The position of the interaction point (IP) is found below the direct streak.

4.9.2 Nikko up

The Nikko up image should produce an image similar to that for Nikko down. However, what we obtained, shown in Figure 4.12, is not a clear image as we would expect. Instead of streaks, we obtained extended structures that make difficult to find the position of the direct image coming from the magnet. We also notice that the image tends to develop in a diagonal fashion. Finally, for Nikko up we recorded rates 30 times lower than for Nikko down. The malfunctioning could have several reason, and all of them have been taken under considerations, with relative upgrades for the system. One problem could be the primary elbow (see 3.3), which is particularly long for this channel (38.3 cm). The length, combined with the fact that the primary pipe was designed in two joint pieces, might have caused the primary pipe to be bent under mechanical stress due to the other pipes. In this case, it is possible that the SR light could have been reflected by the walls of the primary pipe before arriving to the optical box. To solve this potential issue, a new primary pipe has been realized at Wayne State University, which consists of only one rigid piece (see 4.13). Moreover, we decided to paint black the internal walls of all primary pipes, in order to minimize the reflection inside our optical channels. Finally, the problem might have arisen from the stepper motor mechanism for rotating the mirror screws (see 3.8). We suspected the motors of the primary mirror had got stuck and therefore we decided to use the secondary mirror, which was working fine. However, if the primary mirror remained stuck in a blind position, the secondary mirror could not point toward the IP, thereby collecting only reflections. In this case, we decided to upgrade the mechanism of motion of

the primary mirrors to prevent any further problem in the future. The forks used to hook and rotare the screws, shown in Figure 3.8, were available only for the secondary mirrors during the commissioning phase. Now, always at WSU, we are upgrading all the primary mirrors to use the same mechanism (see 4.13), which revealed very efficient during the commissioning phase.

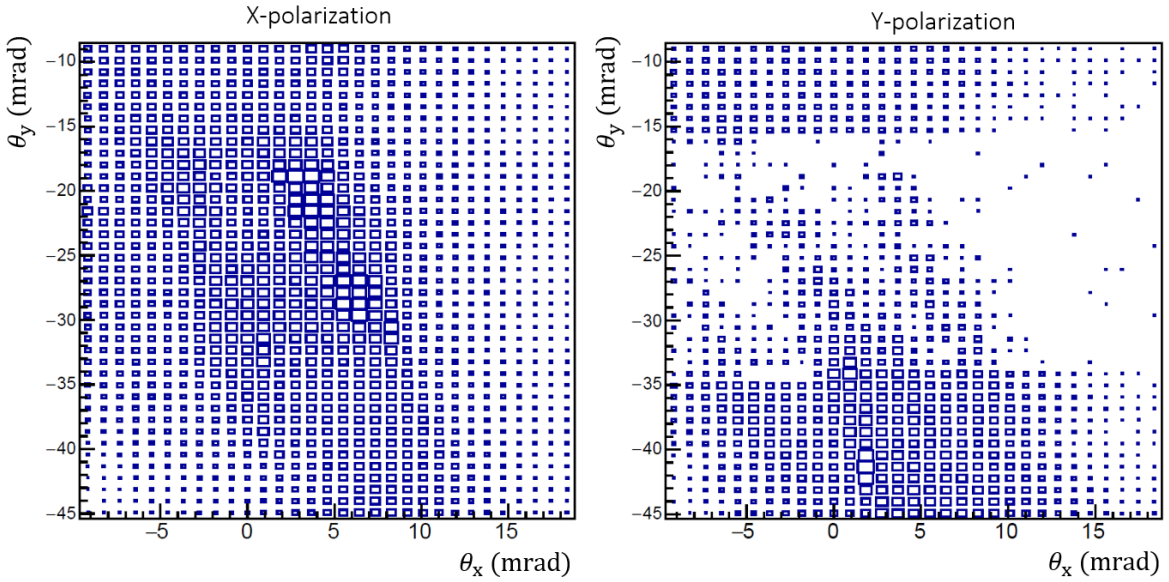

Figure 4.12: Nikko up scan. PMT 24 (red light X-polarized) on the left. PMT 31 (red light Y-polarized) on the right. The area of each cell is proportional to the intensity of the signal in arbitrary units. Instead of streaks, we obtained extended structures that make difficult to find the position of the direct image coming from the magnet.

4.9.3 Oho down

In the case of Oho down, as well as Oho up, we are looking at the SR emitted by the electron beam. In this case, we have a softer bending that results in shorter streaks. The length of the streaks, calculated to be $1.4\,mrad$, is just 40% larger than our resolution, and therefore we expect to be able to see only dots. The image obtained is shown in Figure 4.14. In this case we show the UV image, which is the most clear, and also both X and Y polarizations. There are two clear structures, and we need

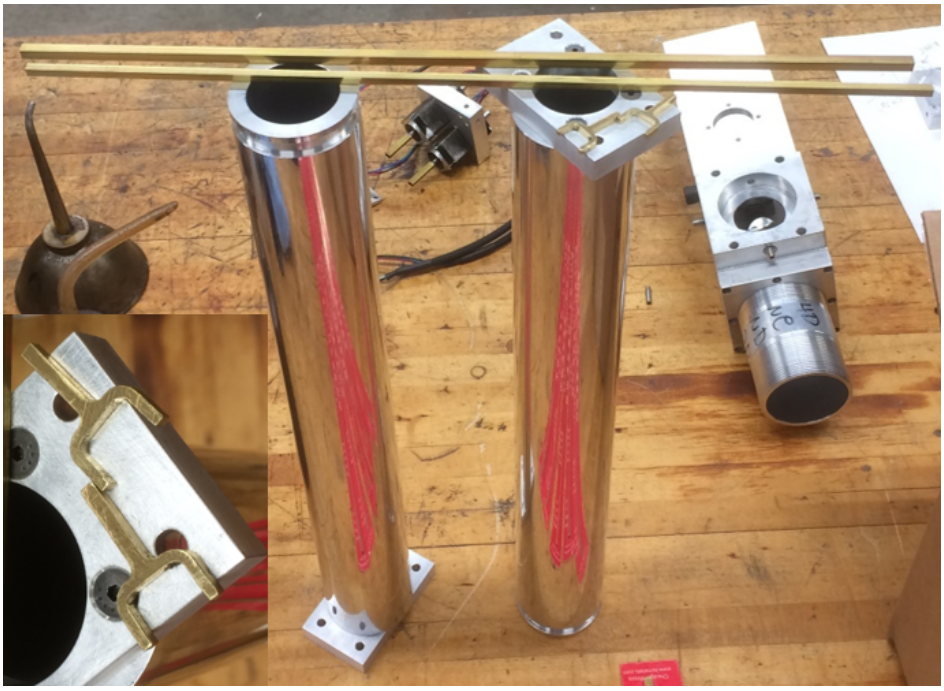

Figure 4.13: Upgrades for the primary pipes and the primary mirrors. We have realized new primary pipes made of a single piece, and a new transmission system for the motors with forks used to rotate the screws that move the remotely controlled mirrors.

to identify which one is the direct image and which is the reflection. In this case we have a soft bending, and therefore the direct image is emitted at an azimuthal angle $\phi \approx 90°$. According to Eqs. 4.5 and 4.6, the direct image should have by far a prevalent X-polarization. On the contrary, a reflection emitted at $\phi = \pi/8$ should have an equal percentage of X and Y polarization. We notice, from Figure 4.14, that the structure I is present in X-polarization image, but disappears in the Y-polarization one. On the contrary, structure II is present in both figures and with approximately equal intensity. Therefore, we infer that I is the direct image, and II is the reflection. The streak I is very short, which is in agreement with our expectation of $1.4\,mrad$. To find the IP, we follow the progression of the beam inside the magnet (see arrow in Figure 4.14) and we go down by the appropriate angle α given in Table 4.6.

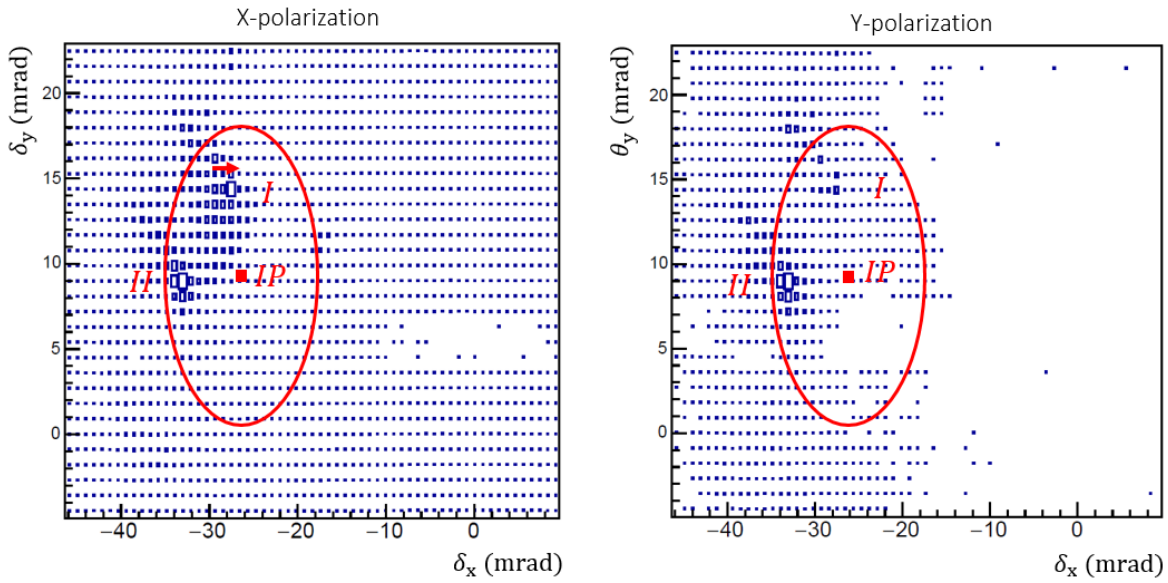

Figure 4.14: Oho down scan. PMT 11 (UV light X-polarized) on the left; PMT 12 (UV light Y-polarized). The area of each cell is proportional to the intensity of the signal in arbitrary units. We have a softer bending that results in short streaks, of size comparable to our resolution. Therefore, we are able to see only dots. The position of the interaction point (IP) is found below the direct streak.

4.9.4 Oho up

As in the case of Oho down, we expect the scan image to contain only dots and not streaks. Figure 4.15 shows the UV images for both X and Y polarizations. Incidentally, the rates for Oho up became very high around the end of the commissioning phase of SuperKEKB, despite the use of progressively smaller collimators, and we reached saturation. To overcome this problem, especially considering that we will be dealing with higher currents in the future, we are planning to place an intensity filter on the hole of the collimator (see Figure 3.23). In this case therefore, the use of the UV image is necessary to analyze the scan. In finding the interaction point, we use the same argument that we have used for Oho Down. Structure I is relatively less intense then structure II when going from X to Y polarization. Therefore, structure I is the

best candidate to be the direct image, with the progression arrow going to the right. Finally, to find the IP we go up by an angle α given in Table 4.6.

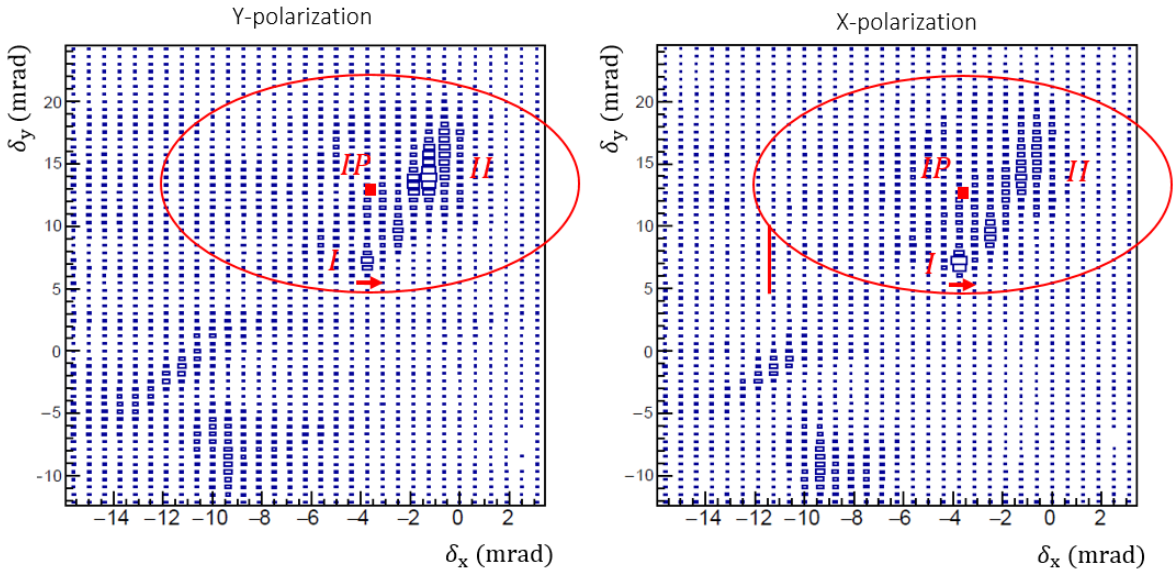

Figure 4.15: Oho up scan. PMT 3 (UV light Y-polarized) on the left; PMT 4 (UV light X-polarized). The area of each cell is proportional to the intensity of the signal in arbitrary units. As for Oho Down, we have a softer bending that results in short streaks, of size comparable to our resolution. Therefore, we are able to see only dots. The position of the interaction point (IP) is found above the direct streak.

4.10 Up-down asymmetry

One of the important features features of the LABM is the possibility to measure the Up-Down asymmetry. Unfortunately, it happened that one telescope for each side recorded much lower rates than the twin. In particular, we obtained overall rates 40 times lower for Oho down respect to Oho up, and rates 30 times smaller for Nikko up respect to Nikko down. We will do it as soon as the detector is reassembled and re-aligned in late 2017.

4.11 Results of the angular scans

The images collected from the angular scans consisted of complex structures, either point-like, streaks, or extended structures. Besides the scan for Nikko up, we were able

to explain the origin of those structures. Then, knowing the position of the magnets respect to the LABM, we were able to calculate the position of the IP. Unfortunately, it was not possible to find the position of the IP for Nikko up, but we are confident that the channel will become fully operative with the upgrades that are underway.

CHAPTER 5 SUMMARY AND CONCLUSIONS

The LABM works as expected for three of our four channels, measuring polarization and spectrum of the incoming light. During the commissioning phase there were no collisions between the beams, and therefore the only source of light was the synchrotron radiation (SR) emitted at the bending magnets. From the interpretation of the image and reconstruction of their physical origin, we were able to find the position of the interaction point (IP). To fix Nikko Up, our defective channel, we have realized some upgrades that will be installed before the phase of real data taking. Among these upgrades we have new primary pipes and a new mechanism to remotely move the primary mirrors. We are confident that these upgrades will surely solve the issue with the channel. Moreover, we had some unexpected lower rates for Nikko Up and Oho Down. Next time, when we assemble the channels again, we will use a spectrometer to verify that the intensity of our LED source propagates properly after each of the mirrors, which have a 0.9 efficiency. Since we expect currents close the nominal values of SuperKEKB, we will install some intensity filter to stop the light in excess. Finally, since our PMTs have a low efficiency in the UV, we will install new ruled gratings in order to diffract the visible spectrum into a broader angle. In conclusion, the LABM commissioning phase allowed us to test all the parts of the apparatus, understanding the defects and finding the countermeasures. We are confident that the four channels will be all ready and working for the real data taking, which will start in early 2018.

BIBLIOGRAPHY

[1] G. Luders, Annals Phys. **2**, 1 (1957), [Annals Phys.281,1004(2000)].

[2] A. D. Sakharov, Pisma Zh. Eksp. Teor. Fiz. **5**, 32 (1967).

[3] T. Abe et al., Belle II Technical Design Report (2010).

[4] M. Arinaga et al., Beam instr. for SuperKEKB rings, in *IBIC2012*, 2012.

[5] J. D. Jackson, *Classical Electrodynamics*, Wiley, 1998.

[6] G. Bonvicini and J. Welch, Nucl. Instrum. Meth. **A418**, 223 (1998).

[7] N. Detgen et al., Prel. Design of a Large Angle Beamstr. Det. at CESR, 1999.

[8] Y. Funakoshi et al., Beam Comm. of SuperKEKB, in *IPAC 2016*, 2016.

[9] S. Y. Lee, *Accelerator physics*, 1999.

[10] C. Patrignani et al., Chin. Phys. **C40**, 100001 (2016).

[11] J. E. Augustin et al., eConf **C781015**, 009 (1978).

[12] P. Bambade et al., Phys. Rev. Lett. **62**, 2949 (1989).

[13] M. Bassetti et al., CERN-LEP/TH **83-24** (1983).

[14] R. Coisson, Phys. Rev. **A20**, 524 (1979).

[15] A. Hofmann, Camb. Monogr. Part. Phys. Nucl. Phys. Cosmol. **20**, 1 (2004).

ABSTRACT

COMMISSIONING OF THE LARGE ANGLE BEAMSTRAHLUNG MONITOR AT SUPERKEKB

by

Salvatore Di Carlo

May 2017

Advisor: Dr. Giovanni Bonvicini

Major: Physics

Degree: Doctor of Philosophy

The Large Angle Beamstrahlung Monitor (LABM) is a device capable to monitor the beam-beam collisions. The LABM measures the beamstrahlung light emitted at large angle during the collisions of electron and positron beams. The properties of the beamstrahlung, spectrum and polarization, are fundamentally related to the size and relative position of the beams. Measuring the beamstrahlung, the LABM delivers information about the size of the beams and their relative position at the interaction point. The LABM will be part of the instrumentation of SuperKEKB, a new e^+e^- collider that aims to reach the world record luminosity of $8 \times 10^{35} \frac{1}{cm^2 s}$. To achieve such luminosity, SuperKEKB will use the nano-beam scheme, which allows for beams with a height of few tens of nanometers. In this framework, the LABM represents an invaluable piece if instrumentation, allowing to measure the size and relative position of the beams at run time and to adjust their position in case of misalignment. The commissioning phase of the LABM took place in parallel to the commissioning phase of SuperKEKB, starting in February 2016 and ending in June 2016. During this phase no collisions took place and the LABM was used to measure the background radiation

produced by bending magnets. All the components of the LABM where tested and the device has proved to work as expected. A few upgrades will be installed at the end of 2017 to improve the performance and the reliability of the device. The LABM will be ready and fully operative at the beginning of 2018, when the first collisions will take place and beamstrahlung light will be measured.

AUTOBIOGRAPHICAL STATEMENT

Name:

Salvatore Di Carlo

Education:
B.S. Physics, University of Palermo, Palermo, Italy, 2012
M.S. Physics, WSU University, Detroit, USA, 2015
Professional Experience:
Graduate Teaching and Research Assistant, Dept. of Physics and Astronomy, Wayne State University, 2011-2017
Biography:
I was born in Palermo in 1988. I obtained my Bachelor degree in Physics from the University of Palermo in 2012. In January 2014, I entered the Wayne State Universitys graduate program in Physics. I have joined the High Energy Physics group under Prof. Giovanni Bonvicinis supervision in April 2014. I received the Degree of Master of Science from Wayne State University in August 2015.